UNIVERSITY OF LEEDS

Fermi Satellite Observations of Gamma-ray Counterparts to Radio and X-ray Binaries

Mohamed Omar Ali

Department of Physics and Astronomy

University of Leeds

Submitted in accordance with the requirements for the degree of

Doctor of Philosophy

January 2014

The candidate confirms that the work submitted is his own and that appropriate credit has been given where reference has been made to the work of others.

Dedicated to my little cousin Abdulaziz Abdulkadir Ali with love, who passed away on 20th March 2013, three weeks before his 14th birthday. You were a young boy filled with joy, love and laughter. Although you are gone now, you will always remain in our hearts. I wish there were more moments we spent together. You are someone we love that became a memory, and a memory we shall all treasure. There is not a single day passed that we do not think of you, and I hope you are resting now in the highest of heaven.

In loving memory of my granddads Dr. Ali Ahmed Omar and Pilot Mohamed Haji Salah. I have heard many great things about you both and I wish you were here with me now to witness how much of an inspiration you have both become. You both achieved your goals in life, which has driven me to push further in mine.

Acknowledgements

I would like to thank my family for all the support and encouragement. I have been blessed with a large family and you have all contributed to helping me achieve my dreams. My nan for all the prayers and having faith in me. My parents (Omar and Ruqia) for giving me the freedom to pursue my dreams. Fatma, Ali, Tariq, Tania, Naseem and Naelah: for all the laughter, love and moments that I will treasure forever. My uncles Ismail Mohamed Salah and Abdulkadir Ali Ahmed for all the encouragements and believing in me.

It's fair to say that this research and thesis would not have been possible without my supervisor Dr. Jeremy Lloyd-Evans. Thank you very much for all your advice, support, encouragement and inspiration. I sincerely appreciate the huge amount of effort you put in when most would have given up. I also want to thank Professor Jim Hinton and Dr. Johannes Knapp for giving me the chance to study this PhD. Thanks also to Professor Alan Watson for transferring the wonderful world of high energy Astrophysics to me.

I would also like to thank the Astrophysics group at the University of Leeds whose support and vast knowledge made all this possible. Special thanks to my office friends Dr. John Ilee and Dr. Hazel Rogers. The

last four years have been an incredible journey and I could not have asked for better people to travel with. Thanks also to Jonny Henshaw for everything you did to help me with the last few days of the thesis crunch time.

Funding from the STFC for this PhD is gratefully acknowledged. I would also like to thank the Fermi Collaboration and the Fermi Science Support Center for providing access to the LAT public archives.

Abstract

With the advent of the Fermi Large Area Telescope (Fermi hereafter), the total number of gamma-ray sources has almost reached 2000 and continues at a rapid pace. The second catalog was released in 2012 and contained 1873 sources, with only 127 of those sources firmly identified. The large number of unidentified sources means that interesting physics could be discovered.

This thesis will present a study of the gamma-ray emission from X-ray and radio binary systems using the Fermi satellite. A review of gamma-ray binaries is presented with examples of sources detected by Fermi. Gamma-ray emission mechanisms are discussed with particular focus on those likely to be detected from binary systems. The connection between X-ray, radio and gamma-ray emission is discussed with emphasis on the features that can be searched in the Fermi observations.

A review of gamma-ray telescopes leading up to the Fermi satellite is presented followed by detailed discussion of the Fermi event reconstruction, classification and background rejection. The Fermi detecter point spread function, energy dispersion and effective area are shown followed by an overview of the recommended Fermi data analysis threads used throughout the thesis.

The current status of gamma-ray binaries that have already been observed with Fermi and the features that could potentially be observed on other binaries is discussed. The techniques used in this thesis including temporal, statistical, cross correlation and pulsar gating are presented.

The analysis and results from known Fermi gamma-ray sources Cygnus X-3 and PSR B1259-63 are presented along side a possible detection of Circinus X-1. The 4.8 hour orbital period of Cygnus X-3 is clearly observed after the application of the pulsar gating technique. PSR B1259-63 is simultaneously observed for the first time in GeV during its periastron passage. A flare is also observed 15 days after periastron which is not detected in radio, X-ray and TeV.

Two catalogues containing radio and X-ray binary systems are analysed using Fermi data and the results presented. Three sources are found to be of interest and further analysed as potential gamma-ray candidates. Although no definitive detections were obtained, the upper limits in gamma-ray flux provide a good starting point for future observations with Fermi and other gamma-ray detectors.

Abbreviations

ACD	Anticoincidence Shield
AGN	Active Galactic Nuclei
ATCA	Australia Telescope Compact Array
AU	Astronomical Unit
CRs	Cosmic Rays
CsI	Caesium Iodide Scintillator
CT	Classification Tree
EGRET	Energetic Gamma Ray Experiment Telescope
EPU	Event Processor Units
FITS	Flexible Image Transport System
GBM	Gamma-ray Burst Monitor
GLAST	Gamma- ray Large Area Space Telescope
GLEAM	GLAST LAT Event Analysis Machine
GTI	Good Time Intervals
HESS	High Energy Stereoscopic System
HMXB	High Mass X-ray Binary
IRF	Instrument Response Function
LAT	Large Area Telescope
MAXI	Monitor of All-sky X-ray Image
PSF	Point Spread Function
PWN	Pulsar Wind Nebula
RA	Right Ascenion
RoI	Region of Interest
RXTE	Rossi X-Ray Timing Explorer
SAA	South Atlantic Anomoly
SED	Spectral Energy Distribution
TOA	Time of Arrivals
TS	Test Statistic
VERITAS	Very Energetic Radiation Imaging Telescope Array System
VHE	Very High Energy
VLA	Very Large Array

Contents

List of Figures

Chapter 1

X-ray Binary Astrophysics

1.1 Gamma-ray Binaries

X-ray and gamma-ray binary systems typically consist of a stellar mass compact object, such as a neutron star or a black hole of up to a few solar masses, and a companion star such as a blue giant or white dwarf. They contain violent environments with high magnetic fields and stellar winds and hence they constitute astronomical particle accelerators that operate under a varying, but often regularly repeating, set of environmental conditions. Throughout the orbit of the binary system, matter and photon field densities are continually changing. Observations of gamma-ray binary systems provide repeatable and stringent tests for models of particle acceleration and high energy emission mechanisms (Dubus, 2007).

There are currently four models for the production of gamma-rays in a binary system, although most detections are believed to be of either the microquasar or the binary pulsar wind models shown in figure 1.1. The other two models are the wind and nuclear powered gamma-ray binaries.

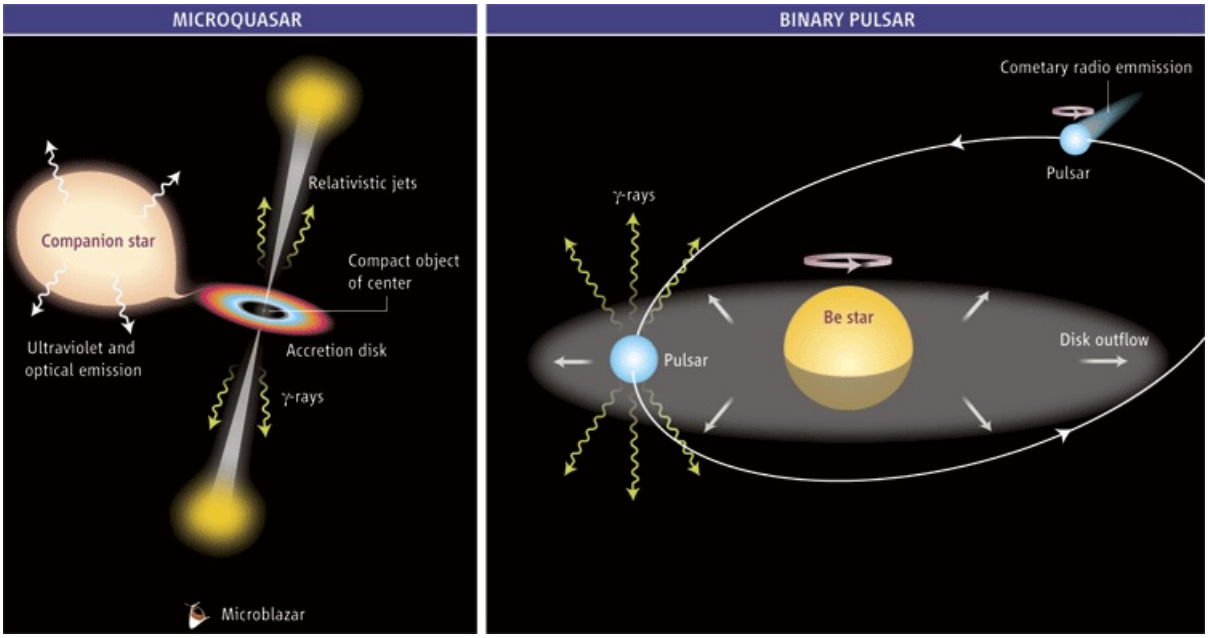

Figure 1.1: *Two models for high energy gamma-ray binary systems. Microquasars (on the left) are powered by the mass accretion from a companion star onto a compact object (a black hole or a neutron star). The accretion produces collimated jets, similar to AGNs, which are believed to be the sites of gamma-ray production. The binary pulsar winds (on the right) are powered by the rotation of the neutron star. The pulsar wind flows away to large distances and it is the interaction of this wind with the companion star outflow that is believed to be the production method for high energy gamma-rays. Figure from Mirabel (2006).*

1.1.1 Microquasars

For the microquasar jet model shown on the left of figure 1.1, a normal star and either a black hole or a neutron star orbit around each other in a binary system. Material is accreted from the companion star into a disc around the compact object and in the process is heated to about 10^7 K (Smponias & Kosmas, 2011). Some of this material emerges again in the form of two relativistic jets, which emit in the radio and X-ray bands (Fender & Maccarone, 2004). Additionally, shock fronts within the jets can accelerate charged particles to high energies, which can then

produce gamma-rays via the inverse-Compton effect or the interaction of hadrons (See section 1.3 for details on emission mechanisms).

There are several methods of categorising microquasars but the most often used is based on the spectral type of the companion star. In high mass X-ray binaries, the companion is a hot, early-type supergiant, which is expected to produce strong stellar winds and a dense ultraviolet radiation field (Böttcher & Dermer, 2005). In contrast, the low mass X-ray binaries contain a companion that is a cool, late-type star with a spectrum peaking in the near-infrared.

For high mass systems the accretion could be powered by material being gravitationally captured from the stellar wind of the massive companion (so called *wind fed*), or be driven by Roche lobe overflow: where matter flows through the inner Lagrangian point of the binary system (Portegies Zwart *et al.*, 1997). However, some high mass binary systems can exhibit hybrid characteristics of both wind and Roche lobe accretion, as is believed to be the case for Cygnus X-1 which has a companion star that almost fills its Roche lobes. In contrast to high mass binaries, the companion star in a low mass system cannot drive a stellar wind which is powerful enough to power a bright X-ray source and therefore accretion in these systems is believed to occur by Roche lobe overflow only (Portegies Zwart *et al.*, 1997).

In the context of high energy gamma-ray emission, there are important differences between high and low mass binary systems. The early-type companion stars of high mass binaries are characterised by dense ultraviolet radiation fields which provide a source of photons that could be inverse-Compton scattered to gamma-ray energies. However, the radiation fields from low-mass companions are relatively soft, which decreases the importance of inverse-Compton scattering (see

section 1.3.1) for gamma-ray production in low-mass binaries.

Stellar winds can also play an important role in the gamma-ray emission of both high and low-mass systems. The relativistic outflows produced by the compact object may interact with the stellar winds and lead to hadronic production of gamma-rays via the production and decay of π^0 (see section 1.3.5).

The compact object also plays a vital role in the production of gamma-rays. One of the fundamental requirements for the emission of gamma-ray photons (for example, at GeV/TeV ranges) is a population of particles, most likely electrons, with TeV energies. The collimated jets produced by the compact objects are an obvious mechanism for the acceleration of these particles to the required high energies.

Microquasars are important as they share similarities with active galactic nuclei (AGN). Both microquasars and AGN contain a compact object, an accretion disc and relativistic jets. Therefore, microquasars are analogous to galactic, scaled down copies of AGNs, with a stellar mass black hole or neutron star instead of a super-massive black hole. Moreover, while most AGNs appear to require many thousands of years to manifest significant changes in behaviour (such as a transition from radio-loud to radio-quiet behaviour (Marecki & Swoboda, 2011)), microquasars can exhibit changes on time scales of years. Since microquasars are relatively close in distance compared to AGNs, they make attractive laboratories to study the physical processes of accretion discs and jets which determine the internal workings of both microquasars and AGNs.

1.1.2 Pulsars and Pulsar Wind Nebulae

Pulsars are the rapidly rotating neutron star remnants from a type II supernova explosion (Kochhar, 1981). A pulsar wind nebula (PWN) is a nebula powered by the relativistic wind of an energetic pulsar. Young PWN emission is typically synchrotron radiation (Section 1.3.2) and the nebulae are often found inside the shells of supernova remnants. The rotating strong magnetic field of the neutron star produces strong and varying electric fields. This is where charged particles are accelerated to high energies and due to the variable electric field, these charged particles (electrons and positrons) emit pulsed synchrotron radiation.

An interesting observational feature of pulsars is that most have rotational periods that are steadily increasing with time. This phenomenon ("spin-down") corresponds to a loss of rotational kinetic energy of up to 10^{39} erg/s. A large fraction of this energy loss is thought to be dissipated by a magnetised wind of relativistic electrons and positrons (Gaensler *et al.*, 2000). After a certain distance from the pulsar, a strong stationary shock front is formed due to the pressure from the pulsar wind being balanced by the external pressure of either a supernova remnant or a dense interstellar medium. The shock front is also a site of charged (mainly electrons and positrons) particle acceleration, which then radiates synchrotron radiation and produces inverse-Compton emission.

The prototypical example of a pulsar-driven nebula radiating X-rays and gamma-rays is the Crab Nebula, which shows un-pulsed emission from radio to gamma-rays (see Cocke *et al.* (1969), Carpenter *et al.* (1976) and Vernetto & for the ARGO-YBJ collaboration (2013)). The 33 ms pulsar is embedded in a pulsar cavity with its relativistic particle and electromagnetic wind confined by a shock. As the pulsar

wind (a mixture of electromagnetic fields and particles) interacts with the shock, it results in non-thermal synchrotron and inverse-Compton radiation being emitted. The volume of the emitting region is larger than the inner pulsar cavity, and both fields and particles diffuse out from this central pulsar cavity into the surrounding main nebula.

A schematic of the three regions of non-thermal radiation associated with a rotation powered pulsar such as the Crab Nebula is shown in figure 1.2. The details of acceleration, particle composition and electromagnetic structure of relativistic winds near the pulsar (within the light cylinder radius) are poorly constrained. The relativistic winds carry off a major fraction of the pulsar rotational energy but by the termination shock almost all energy is believed to be in the form of kinetic energy of the wind's bulk motion. Again, the mechanism that provides for such an efficient transformation of the rotational energy of the wind into kinetic energy is unknown.

The unshocked wind, although magnetised, does not emit synchrotron radiation because the electrons of the wind move together frozen into the plasma magnetic field. However, the wind can be observed directly through its inverse-Compton radiation caused by the bulk motion Comptonization by external low-energy photons of different origin. The inverse-Compton photons are expected to be in the energy range between 10 GeV and 10 TeV, depending on the wind's bulk Lorentz factor, which is believed to be within 10^4 - 10^7 (Aharonian & Bogovalov, 2003).

The pulsar wind eventually terminates in the interstellar medium resulting in strong shocks that lead to the formation of synchrotron and inverse-Compton nebulae around the pulsar. An interesting note is that while the spectrum of the inverse-Compton radiation of the unshocked wind is primarily determined by the

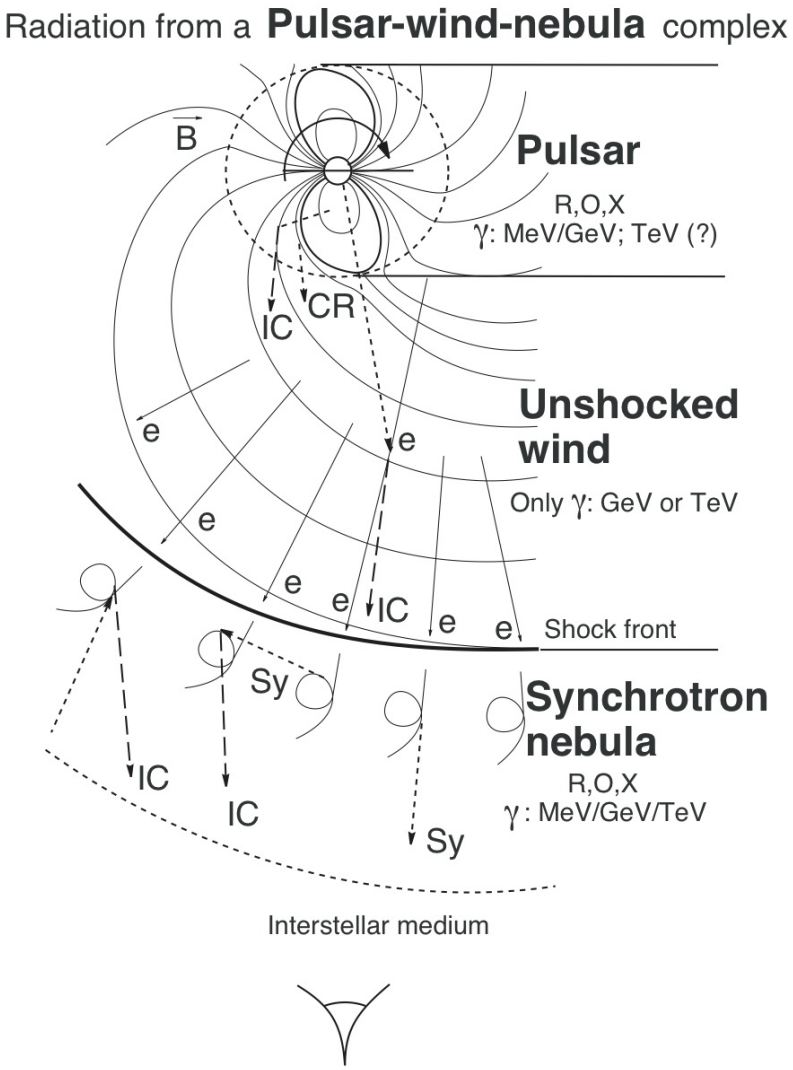

Figure 1.2: *Three regions of non-thermal radiation associated with a rotation powered pulsar. The first region (pulsar) is within the light cylinder where the magnetospheric pulsed radiation from radio to gamma-rays is produced. The second region (unshocked wind) is the wind of cold relativistic plasma which emits GeV and TeV gamma-rays through the inverse-Compton mechanism. The last region (synchrotron nebula) is the surrounding nebula that, through synchrotron and inverse-Compton mechanisms, emits from the radio up to TeV gamma-rays. Figure from Aharonian & Bogovalov (2003).*

wind's Lorentz factor, the latter has less direct effect on the broadband spectrum of the pulsar nebula. However, the inverse-Compton radiation from the unshocked wind is yet to be detected for any pulsar as the inverse-Compton radiation from the pulsar nebula is dominant when we inspect a pulsar's spectrum. Nevertheless, this is also the reason why studying binary pulsar wind nebula (a model is shown on the right of figure 1.1) is interesting, as the interaction between the pulsar and the companion will change the observed spectral energy distribution compared to an isolated pulsar. The interaction of the pulsar wind with the stellar wind from the companion forms strong shocks, which is variable as the pulsar orbits its companion star. Therefore, the spectrum of the inverse-Compton radiation from the shocked region will be different than in the case of an isolated pulsar. However, the spectrum of the inverse-Compton radiation of the unshocked wind will be relatively unaffected and can be observed by Fermi (see section 2.2 for details on the telescope) leading to better understanding and constraining of the physics involved in the unshocked wind of pulsars.

1.1.3 Wind and Nuclear Powered Emission

The other models for gamma-ray emission from binary systems is through wind and nuclear powered binaries. For wind powered emission, the requirement is that two massive stars be in orbit so that there is a non-relativistic mass outflow from both that can collide and produce shocks. These shocks are then believed to be regions of particle acceleration and hence gamma-ray production. However, for the gamma-ray energy regime, the only candidate for this emission mechanism is η Carinae, which is believed to be formed of either two or possibly three massive stars (Pittard, 2010) and the shocks caused by their respective winds interacting could be a source

of gamma-rays. Both AGILE and Fermi (see AGILE Collaboration (2010) and The Fermi LAT collaboration (2010)) have detected gamma-rays coincident with the position of η Carinae but neither have confirmed the source of emission as being from η Carinae. From a gamma-ray perspective, it will be interesting to detect colliding wind powered binaries and constrain if they really are powered by colliding winds or if there are other mechanisms.

The other mechanism is nuclear powered binary gamma-ray emission in which a binary system containing a compact white dwarf and a massive star produces a nova. The first gamma-ray detection of such a binary is the Fermi detection of V407 Cyg (Fermi LAT Collaboration, 2010), which is a binary containing a compact white dwarf and a red giant star of about 500 $M_{\odot}$. There have subsequently been four more nova observed by Fermi (V339 Del, Nova Mon 2012, Nova Sco 2012 and V1369 Centauri; see Page *et al.* (2013), Cheung & on behalf of the Fermi-LAT collaboration (2013) and Cheung *et al.* (2013)). The red giant star in V407 Cyg will be leaking gas into space and some of it accumulates on the surface of the white dwarf. Over a long period of decades to centuries, this gas piles on and eventually becomes hot and dense enough to fuse into helium, which triggers a runaway reaction that explodes the accumulated gas. The explosion creates a shock front composed of particles, ionised gas and magnetic fields. It is these magnetic fields that trap and accelerate particles to high energies which then collide with the red giant's wind and emit gamma-rays. Nuclear powered gamma-ray binaries are a new class of gamma-ray binaries and further detections could shed light on the emission mechanism as well as the environments of novae.

1.2 Spectral States

X-ray black hole binaries have, historically, shown two distinct states: the high/soft state when the source X-ray intensity is high, and the low/hard state when the source X-ray intensity is low. The X-ray emission in the high/soft state is dominated by thermal emission from the optically thick accretion disc. The X-ray spectrum in the low/hard state is dominated by a hard (photon index < 2) power law with typically ≈ 100 keV cut off energy. Further monitoring have also shown an intermediate state as well as the state transitions. It is not clear what drives the state transitions but the mass accretion rate is believed to be partly responsible (Homan *et al.*, 2001). The low/hard state is believed to indicate low mass accretion rates and corresponds to the production of collimated radio jets. The high/soft state is believed to indicate high mass accretion rates and jet formation appears to be suppressed in this state. The intermediate and transition states are characterised by strong disc emission and a non-thermal tail upto high energies. These are often accompanied by radio flaring which are believed to be from the propagation of the highly relativistic clouds of plasma through the mildly relativistic remnants of the low/hard state jet.

Neutron star binaries are separated into two catagories which are named after the shapes traced by their spectral evolution in a colour-colour diagram. The *atoll* sources, similar to black hole binaries, exhibit spectrally distinct states and are believed to be linked to the mass accretion rate. The *banana* state corresponds to the high/soft state of black hole binaries and the *island* state corresponds to the low/hard state (Done *et al.*, 2007). *Atoll* sources also show evidence of correlation between X-ray and radio emission similar to that observed in black home binaries

(Tudose *et al.*, 2009). Z sources have high X-ray luminosity exceeding half the Eddington luminosity. They are typically observed with high accretion rates and therefore do not have a counterpart to the low/hard state of black hole binaries. The X-ray and radio emission in Z sources are yet to be definitively correlated, which would suggest that the processes that lead to jet formation may be different from those in black hole binaries and *atoll* sources (see Church *et al.* (2006) and Done *et al.* (2007)).

The spectral states of X-ray binary systems play an important role in the production of gamma-ray emission (see section 1.3 for detailed emission mechanisms). One of the fundamental requirements for production of gamma-rays is the presence of a population of particles at TeV energies (Weekes, 2003). An obvious mechanism for acceleration of particles to these high energies is via the shocks within collimated jets. Furthermore, pulsars can produce relativistic winds of particles that can interact with the stellar wind of the companion star, which form shocks and accelerate particles to high energies (Dubus, 2006b).

1.3 Gamma-Ray Emission Mechanisms

Planck's law states that the average energy of a thermal black body radiation is directly proportional to its temperature. Stars with typical surface temperatures of about 6000 K (for example, the Sun) emit in the visible with a tail extending to X-ray energies. In the extreme temperatures of the hottest objects in the universe such as accretion discs around compact objects, they can emit X-rays in the range of up to tens of keV. There is no celestial object which is hot enough to emit, thermally, photons in the high energy gamma-ray range. Hence, gamma-rays

must be produced in extreme non-thermal processes and these radiative emission mechanisms are discussed in this section, particularly the inverse-Compton and synchrotron processes. Where appropriate, examples of the scales required to produce gamma-ray photons of 1 GeV are shown.

1.3.1 Inverse-Compton Scattering

Inverse-Compton is the process by which low energy photons are up-scattered to higher energies through collisions with energetic particles. In the rest system of a relativistic electron with Lorentz factor γ, a photon of energy ε will appear to be moving with an energy of $\gamma\varepsilon$. The Compton scattered photon has an energy $\leq \gamma\varepsilon$ in the inertial frame, and energy $\sim \gamma^2\varepsilon$ in the laboratory frame. The energy of the Compton boosted photon can be defined as

$$E_\gamma \approx \varepsilon\gamma^2 \text{ when } \gamma\varepsilon \ll m_e c^2 \tag{1.1}$$

and

$$E_\gamma \sim E_e \text{ when } \gamma\varepsilon \gg m_e c^2 \tag{1.2}$$

Cross sections of the regions represented by the above equations are calculated by Heitler (1954) as

$$\sigma_c = \sigma_T \left(1 - \frac{2\gamma\varepsilon}{m_e c^2}\right) \tag{1.3}$$

and

$$\sigma_c = \frac{3}{8}\sigma_T \left(\frac{m_e c^2}{\gamma\varepsilon}\right)\left[\ln\left(\frac{2\gamma\varepsilon}{m_e c^2}\right) + \frac{1}{2}\right] \tag{1.4}$$

where σ_T is the Thomson cross section with a numerical value of 6.65 x 10^{-25} cm^2. The maximum energy that a photon can acquire is

$$E_{max} \sim 4\gamma^2\varepsilon \tag{1.5}$$

which corresponds to a head-on collision with the energetic particle, and the mean gamma-ray energy is given by

$$\langle E_\gamma \rangle = \frac{4}{3}\gamma^2 \langle\varepsilon\rangle \tag{1.6}$$

The inverse-Compton process is important in regions of high photon densities. The process is particularly efficient at elevating photon energies to very high levels such as in AGNs where the relativistic electrons can up-scatter photons to the GeV-TeV energy regime. Other examples include compact stars where an accretion disc is sufficiently hot to emit X-rays, and the compact object generates beams of high energy charged particles. For example, using equation 1.6, 1 GeV gamma-ray photons will come from electrons of $\approx$ 1.5 x 10^{10} eV where $\varepsilon \approx 10$ keV.

1.3.2 Synchrotron Emission

Electrons (or positrons) transversing a transverse magnetic field will produce synchrotron radiation. The emitted synchrotron radiation energy of a relativistic electron (or positron) per unit time per unit frequency interval, as a function of

frequency ν of the emitted photon, is given by

$$P(E_e, \nu) = \sqrt{3}(eB)sin\phi F(\nu/\nu_c)(E^2/m_e c^2) \tag{1.7}$$

where E_e and m_e are the energy and mass of the electron, B is the strength of the magnetic field, ϕ is the magnetic field pitch angle, and $F(\nu/\nu_c) = (\nu/\nu_c)\int_{\nu/\nu_c}^{\infty} K_{5/3}(\eta)\mathrm{d}\eta$, with $K_{5/3}$ being the modified Bessel function of the order 5/3. The critical frequency ν_c is given by

$$\nu_c = \frac{3eBsin\phi}{4\pi m_e c}\left(\frac{E_e}{m_e c^2}\right)^2 \tag{1.8}$$

The frequency at maximum emission is given by

$$\nu_m = 1.2 \times 10^6 B_\perp \left(\frac{E_e}{m_e c^2}\right)^2 \tag{1.9}$$

or at an energy

$$E_{\gamma,m}(\mathrm{eV}) = h\nu_m = 5 \times 10^{-9} B_\perp \left(\frac{E_e}{m_e c^2}\right)^2 \tag{1.10}$$

Here, $B_\perp = Bsin\phi$ is in Gauss. Using equation 1.10, gamma-ray photons with energy 1 GeV will come from electrons of energy $E_e \approx 2\times10^{14}$ eV in a 1G magnetic field.

1.3.3 Non-thermal Bremsstrahlung

Charged particle acceleration through electric fields can produce gamma-rays via the process of bremsstrahlung. For example, an electron passing close to an atomic nucleus will experience the strong positive charge of the nucleus, which results in

the electron's trajectory being changed by the acceleration. The change in electron energy caused by the electron-ion collision can be used to obtain the total intensity per unit frequency in bremsstrahlung radiation as

$$I_\nu(E_e) = \frac{Z^2 e^6 n}{12\pi^3 \epsilon_0^3 c^3 m_e^2 v_e} \ln\left(\frac{192 v_e}{Z^{1/3} c}\right) \tag{1.11}$$

where $I_\nu(E_e)$ is in units of erg cm^{-2}, $e = 1.6 \times 10^{-19}$ C is the electron's charge, m_e and v_e being the electron mass and velocity, $\epsilon_0 = 8.85 \times 10^{-3}$ C^2 erg^{-1} cm^{-1} as the permittivity of the vacuum, and n as the number density of matter. The spectrum of bremsstrahlung radiation is flat up to the electron kinetic energy given by

$$E_\gamma = (\gamma - 1) m_e c^2 \tag{1.12}$$

where γ is the electron's Lorentz factor. Above this, it drops sharply towards zero as all the kinetic energy of the electron has been transferred to the bremsstrahlung photon.

For bremsstrahlung radiation, the gamma-ray emissivity is proportional to the density of the ambient material. However, for most astrophysical sources, the photon density is typically several orders of magnitude higher than the matter density. Therefore, high energy electrons lose their energy more efficiently by synchrotron radiation and inverse-Compton scattering than by bremsstrahlung radiation. Nevertheless, in very dense environments such as in γ Cygni supernova remnant (where $n = 300$ cm^{-3} (Uchiyama *et al.*, 2002)) bremsstrahlung emission may dominate.

Radiation loss for bremsstrahlung is such that the electron energy falls by a

factor of e in one radiation length. Taking the interstellar medium with a mean density of 1 atom cm^{-3} as an example (and radiation length of an electron in hydrogen is $\approx$ 60 g cm^{-2}) then an electron's energy falls by a factor e in a length of about 10 Mpc. The gamma-ray emissivity, $q_b(E_\gamma)$, for bremsstrahlung from electrons in the interstellar gas was shown by Stecker (1975) to be given by

$$q_b(E_\gamma) = 4.3 \times 10^{-25} n I_e(> E_\gamma)/E_\gamma \; cm^{-3} s^{-1} MeV^{-1} \tag{1.13}$$

where n is the number density of nuclei and $I_e(> E_\gamma)$ is the integral energy spectrum of the electrons.

1.3.4 Curvature Radiation

Similar to synchrotron radiation, curvature radiation is caused by charged particles being accelerated in a magnetic field. However, curvature radiation occurs in the presence of an exceptionally strong magnetosphere of a pulsar where the charged particles are constrained to move parallel to the magnetic field lines with essentially zero pitch angle. Since these magnetic field lines are themselves curved, the particles radiate in the direction of motion (Manchester & Taylor, 1977). The characteristic energy of curvature radiation is given by

$$E_c(eV) \approx \frac{3}{2} \frac{\hbar c \gamma^3}{\rho_c} = \frac{2.96 \times 10^{-5} \gamma^3}{\rho_c(cm)} \tag{1.14}$$

where ρ_c is the radius of curvature of the magnetic field lines and $\gamma = E_e/m_e c^2$. Curvature radiation is particularly important for high energy electrons and positrons within the environments of pulsars. For example, photons with energy of 1 GeV are emitted when an electron with energy of 8×10^{12} eV moves along a field line

with a curvature of 10^8 cm, which is typical for a pulsar.

1.3.5 Gamma-rays Produced through Hadronic Interactions

Most of the very high energy cosmic rays observed on Earth are protons and heavier nuclei. These particles produce high energy gamma-rays in inelastic interactions with ambient matter via the production and subsequent decay of secondary pions. Neutral and charged (π^0 and $\pi^{\pm}$ hereafter) are produced with the same probability, therefore one third of the π mesons produced are neutral. The process for the decay of π^0 mesons into two gamma-rays is

$$p + p \rightarrow \pi^0 + X \rightarrow \gamma\gamma + X \tag{1.15}$$

Here, X represents minor secondary particles. The minimum kinetic energy for a proton to produce a π^0 is given by

$$E_{th} = 2m_\pi c^2 \left(1 + \frac{m_\pi}{4m_p}\right) \approx 280\ MeV \tag{1.16}$$

where m_π is the mass of a $\pi^0 \approx 135$ MeV. At rest, a π^0 will decay to produce a photon of energy $E_\gamma = \frac{1}{2}m_\pi c^2 \approx 68$ MeV.

The observation of π^0 decay gamma-rays near the acceleration site of the hadronic cosmic rays offers the opportunity to study the acceleration mechanisms of cosmic rays (Aharonian, 2004).

1.4 Connection between X-ray and Gamma-ray Emission

There are several characteristics of X-ray binaries and microquasars that indicate the presence of accelerated non-thermal particles. These particles can then be responsible for gamma-ray emission via the mechanisms explained in section 1.3. The sources used to illustrate these characteristics have either been detected at gamma-rays or are potential candidates.

1.4.1 Superluminal Jets

Microquasar GRS 1915+105 was the first X-ray binary source detected that had clear evidence for relativistic jets (Mirabel & Rodríguez, 1994). Multi-wavelength studies of GRS 1915+105 by Mirabel *et al.* (1998) showed an initial infrared outburst followed by a radio outburst as a result of a bipolar ejection of plasma. A simple explanation for this is that both outbursts were due to synchrotron radiation from the same relativistic electrons. Adiabatic expansion of plasma in the jets causes the electrons to lose energy and therefore shift the spectral maximum of the synchrotron emission from the infrared to the radio. Atoyan & Aharonian (1999) proposed gamma-ray emission from the relativistic electron population in the jets via synchrotron or Inverse Compton scattering. However, GRS 1915+105 has not been detected yet in the gamma-ray domain (HESS Collaboration, 2009).

Circinus X-1 is another X-ray binary source with evidence of superluminal jets (Fender *et al.*, 2005) and is analysed with Fermi (see section 2.2 for details on Fermi telescope) data in section 5.1.

1.4.2 Strong Radio Outbursts

Cygnus X-3 was first detected and observed in 1972 when it reached radio flaring levels of up to 20 Jy. It has since become one of the best examples of expanding synchrotron emitting sources, which were successfully modeled by particle injection in twin jets (Martí *et al.*, 1992). The development of the two sided relativistic radio jets was first imaged at the arcsecond scales by the Very Large Array (VLA) and is shown in figure 1.3. Multi-wavelength observations of Cygnus X-3 have shown that the strong radio flares only occur when there is a high soft X-ray flux and a hard power-law tail. Gamma-ray emission might be detectable if the electrons responsible for the strong radio outbursts are accelerated to high enough energies. The Fermi LAT Collaboration (2009b) and the AGILE Collaboration (2009a) have published results showing detections of Cygnus X-3 in the gamma-ray domain.

Detailed analysis of Cygnus X-3 with Fermi is shown in section 5.2.

1.4.3 Jet Interaction with Interstellar Medium

There are some binaries where it is possible to observe the interaction between the source jet and the surrounding interstellar medium. VLA observations of Cygnus X-1 show extended radio emission (Martí *et al.*, 1996) around the microquasar similar to an elliptical ring with Cygnus X-1 offset from the centre. Gallo *et al.* (2005) suggest that the extended radio emission is a result of a jet-blown ring around Cygnus X-1 (see figure 1.4), which develops at the location where the pressure exerted by the jet is balanced by the interstellar medium. In the gamma-ray domain, TeV flares have been observed by the MAGIC Collaboration and have been interpreted as a result of the jet-cloud interaction. Protons in the jet interact

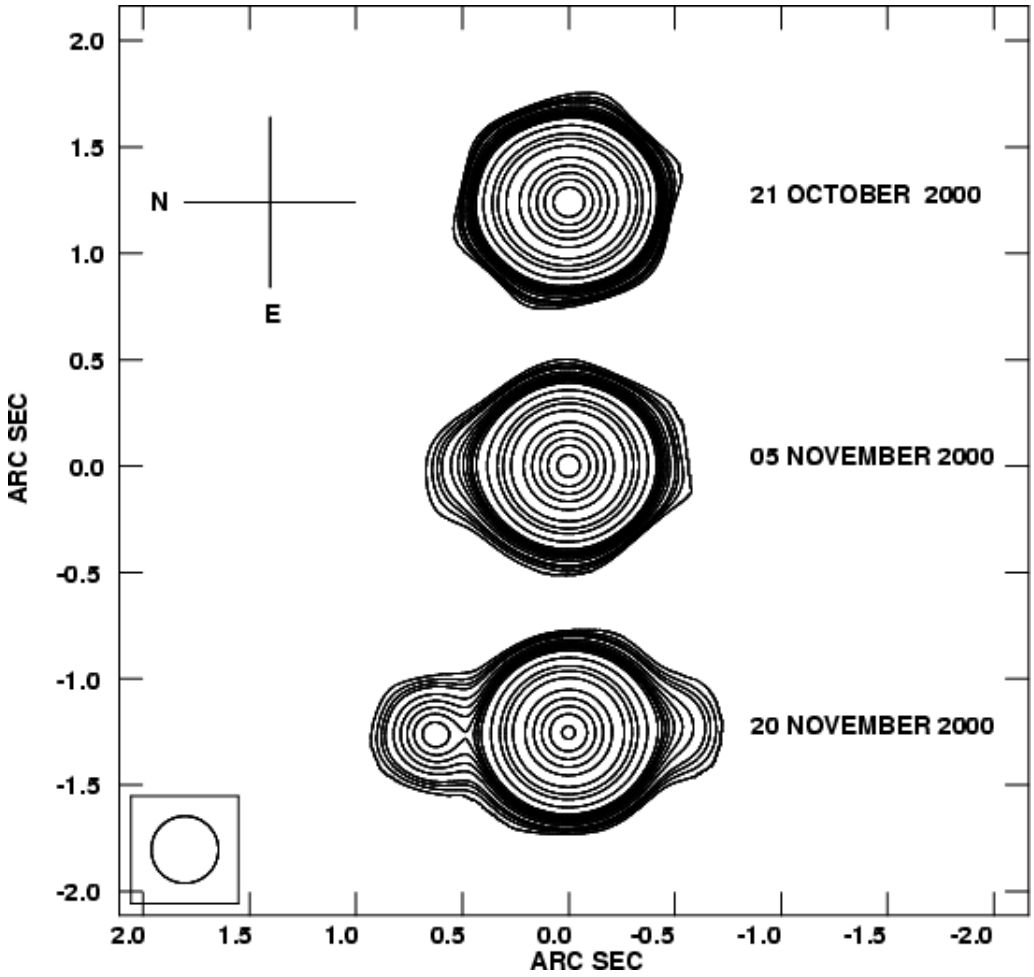

Figure 1.3: *VLA observations of Cygnus X-3 showing the development of a two sided relativistic radio jet. Figure from* Martí et al. *(2001).*

with the ions in the cloud producing inelastic p-p collisions and pion decay, which are detected as TeV gamma-ray flares (Romero *et al.*, 2010). Cygnus X-1 has also been detected by the AGILE Collaboration (Sabatini *et al.*, 2010) but not by the Fermi-LAT Collaboration.

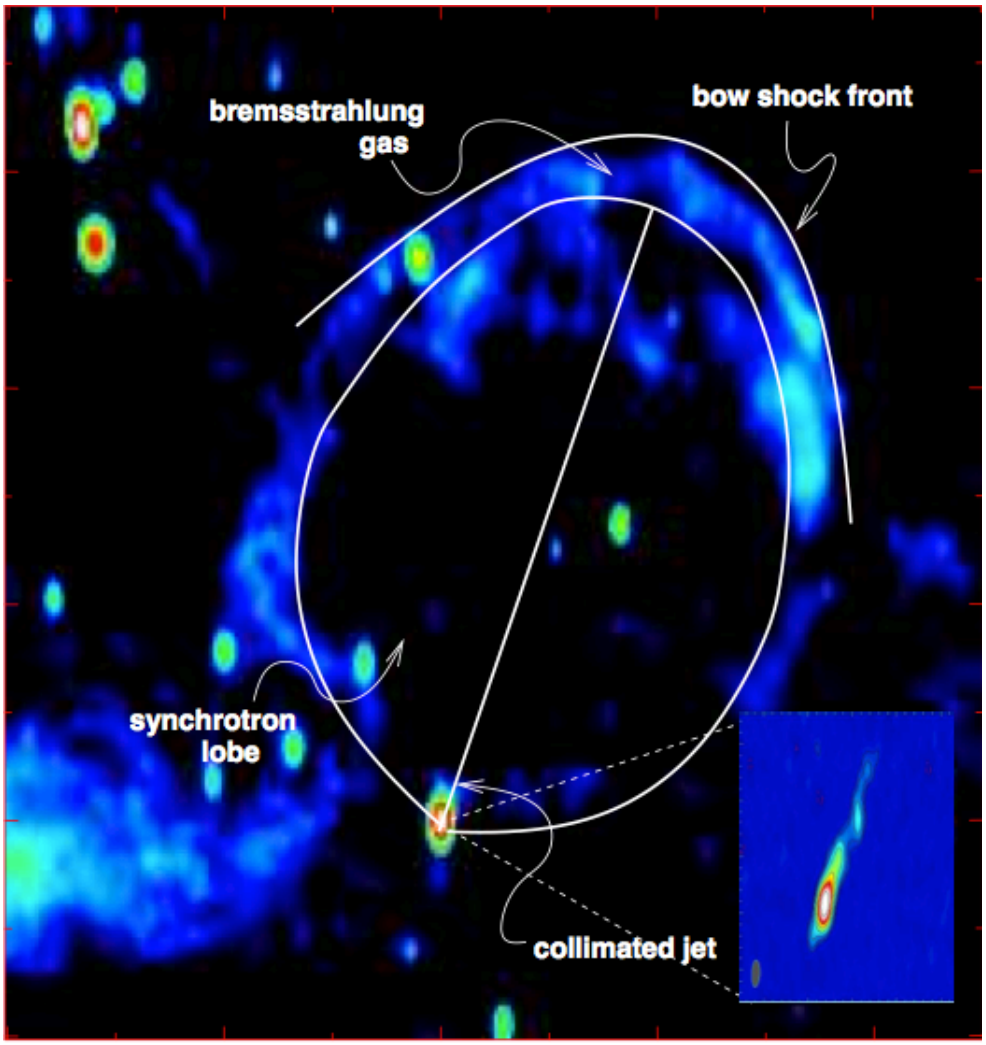

Figure 1.4: *The ring structure surrounding Cygnus X-1, which is formed as a result of the pressure from the jet (shown in the inset) being balanced by the interstellar medium. Figure from Gallo et al. (2005).*

1.4.4 Radio Variability

Some sources show periodic non-thermal emission, which can be the archetypal sign for gamma-ray production. One of these sources is LS I +61°303, which has periodic non-thermal radio outbursts every 26.6 ± 0.5 days (Abdo *et al.*, 2009a). Massi *et al.* (2004) found extended and precessing radio emitting structure. Further analysis found this structure to have a rotating elongated morphology (Dhawan *et al.*, 2006), which could be consistent with the interaction between the relativistic wind of a non-accreting pulsar and the wind of the stellar companion (see Romero *et al.* (2007) for a detailed discussion on this model). LS I +61°303 has been detected by Fermi (Abdo *et al.*, 2009a), becoming the first detection of orbital periodicity in gamma rays between 20 MeV-100 GeV.

1.4.5 Pulsar Wind Interaction with Circumstellar Disc

PSR B1259-63 became the first variable galactic source to be discovered emitting in the TeV gamma-ray domain (HESS Collaboration, 2005a). It contains a 47.7 ms radio pulsar orbiting every 3.4 years around a massive companion in a highly eccentric orbit. Detailed modelling of the radiation mechanisms and interaction geometry of the system was done by Tavani & Arons (1997). There are two models to explain the TeV gamma-ray emissions. In the hadronic model, the emission is caused by the collisions of high energy protons accelerated by the pulsar wind and the circumstellar disc (Neronov & Chernyakova, 2007). The other model suggests that the emission can be explained by the inverse Compton (IC) scattering of ultra-relativistic electrons accelerated at the pulsar wind termination shock (Khangulyan *et al.*, 2007). PSR B1259-63 was first observed in the TeV gamma-ray domain by

the HESS Collaboration in 2004 (HESS Collaboration, 2005b) and in the MeV-GeV domain by the Fermi-LAT Collaboration in 2010 (Abdo *et al.*, 2011). Both observations occured during the periastron of the system.

Analysis of Fermi data on PSR B1259-63 is shown in section 5.3 with a clear detection of the source during periastron.

Chapter 2

Observational Instruments

Gamma-ray telescopes, both ground and space based, have developed rapidly over the past five decades and are now complementary in energy coverage so that a variety of sources can be studied. This chapter describes the Fermi satellite (launched on 11 June 2008), which is the successor to EGRET (1991-2000) on the Compton gamma ray observatory.

2.1 Brief History of Gamma-ray Telescopes

The first dedicated gamma-ray telescope was carried into orbit onboard the Explorer 11 satellite in 1961 (Kraushaar & Clark, 1962). It detected less than 100 gamma-ray photons, which appeared to be coming from every direction suggesting the existence of a gamma-ray background. This could be explained by the interaction of cosmic rays with the interstellar medium. The next big leap for gamma-ray astronomy arrived with the detector onboard the OSO-3 satellite, which was launched in 1967. It was capable of detecting gamma-ray emission from solar flares as well as more than 600 events from outside the solar system (Kraushaar *et al.*,

1972).

The next gamma-ray observatory was SAS-2, which was launched in 1972 but stopped operation in 1973 when the low voltage power supply failed (Fichtel *et al.*, 1975). One of the successes for SAS-2 was the first detection of the pulsar Geminga. The other gamma-ray satellite launched in the same decade was COS-B (launched in 1975, see Bignami *et al.* (1975) for details). It collected gamma-ray data for 6.5 years until 1982. COS-B was the most successful gamma-ray observatory at the time and scientific results included the 2CG Catalogue, which listed 25 gamma-ray sources and a map of the Milky Way galaxy. However, the resolution of COS-B was insufficient to identify most of the point sources with known sources in other wavelengths.

COS-B was followed by the Energetic Gamma Ray Experiment Telescope (EGRET) on the Compton Gamma Ray Observatory (GRO) in 1991 and was operational until 2000 (Hartman *et al.*, 1992).

The capabilities of Fermi-LAT are shown next to its predecessor, EGRET on the GRO, in table 2.1. The larger effective area, wider field of view and improved angular resolution greatly enhance the sensitivity of Fermi to gamma-ray emission from binaries. The combination of the wide field of view with the scanning observational mode means that the entire sky is covered in $\sim$ 3 hours, which enables detection of fainter sources in shorter time intervals than previously possible with EGRET. This is vital in triggering rapid multiwavelength follow up observations. The increased energy coverage of Fermi allows it to work in synergy with current imaging atmospheric Cherenkov telescopes such as HESS and VERITAS.

EGRET left a legacy of a large fraction of unidentified sources in its 3EG catalog (271 sources of which 170 are unidentified). The improved performance

	LAT	EGRET
Energy range	20 MeV to >300 GeV	20 MeV – 30 GeV
Energy resolution (on axis, 100 MeV – 10 GeV)	<10%	10%
Peak effective area	9000 cm^2	1500 cm^2
Angular resolution (single photon, 10 GeV)	0.15°	0.54°
Field of view	>2.2 sr	0.4 sr
Deadtime per event	27 us	100 ms

Table 2.1: *Comparison of Fermi-LAT and EGRET capabilities. The increased capabilities on the Fermi-LAT make it 25 times more sensitive than EGRET and therefore detect more sources. Note that most of these values are energy dependant such that the energy resolution of the Fermi-LAT at 300 GeV is approximately 18% and the angular resolution is 0.6° at 1 GeV (68% containment radius). Table reproduced from the Fermi website*[1].

from Fermi allows us to identify previously unidentified sources and this is vital in our search for binary systems. For example, 3EG J0241+6103 was associated (although the position was not certain) with LSI+61°303, which is a radio flaring high mass X-ray binary (HMXB) system at 2 kpc with an orbital period of 26.5 days. Daily and monthly variablity was observed by EGRET but no periodicity was detected, and therefore a firm association could not be made (see Tavani *et al.* (1998) for details). However, Fermi was able to not only detect the gamma-ray emission, but also find a periodicity of 26.6 ± 0.5 days and with the emission peaking at periastron.

Therefore, the increased performance from Fermi enables us to to try and identify some of the large list of unidentified sources from the 3EG catalog. Fur-

[1]http://fermi.gsfc.nasa.gov/science/instruments/table1-1.html

thermore, we are now in a position to search for X-ray and radio binaries that were previously inaccessible in the MeV-GeV domain.

2.1.1 Imaging Atmospheric Cherenkov Telescopes

With the advent of imaging atmospheric Cherenkov telescopes, there has been a dramatic progress in very high energy (typically between 100 GeV to 10 TeV) gamma-ray astrophysics (Hillas, 2013). Therefore, imaging atmospheric Cherenkov telescopes are complimentary with the energy range covered by Fermi.

High energy gamma-rays and hadrons (protons and nuclei) produce electromagnetic and hadronic showers, respectively, within the atmosphere. Before the advent of high speed computing, Heitler presented a simple model of the development of an electromagnetic shower (see Heitler (1954)). The Heitler model can also be extended to extensive air showers (see Matthews (2005) for a simple model and explanation). These models are used to determine simple shower properties for cascades initiated by gamma-rays or hadrons. Showers initiated by gamma-rays can be differentiated from cosmic-ray showers using imaging parameters first defined by Hillas (1985) such as width, length, distance and asymmetry. Gamma-ray signals can then be extracted statistically from observed images of a shower. Stereoscopic observations can be achieved by using multiple telescopes such that the intersection of axes of elongated Cherenkov images can be used to determine direction of incoming gamma-ray.

One of the current generation of imaging atmospheric Cherenkov telescope is HESS located in the Khomas region of Namibia, approximately 1800m above sea level. The array consists of four telescopes positioned in a square. Each telescope is 13m in diameter and contains 960 photo-multiplier tubes, giving the whole array

a field of view of 5^o (HESS Collaboration, 2006b).

One of the successes of HESS is the ongoing Galactic Plane Survey, which has revealed more than 50 sources of high energy emission (HESS Collaboration, 2006a). However, a significant number of these sources are unidentified as either not having compelling counterparts or being completely dark in other wavelengths (HESS Collaboration, 2008). For the latter, extensive multiwavelength observations are required to identify the sources. The former sources could be identified if the angular resolution of Cherenkov telescopes is improved in future detectors. Such a next generation of telescopes is the Cherenkov Telescope Array (CTA), which is planned to offer a factor of 5-10 improvement in sensitivity (Actis *et al.*, 2011).

2.2 Fermi Large Area Telescope

Fermi has two instruments, the Large Area Telescope (LAT) and the Gamma-ray Burst Monitor (GBM), which are used to observe gamma-ray sources (Atwood *et al.*, 2009). The LAT is an imaging gamma-ray detector covering the 20 MeV to 300 GeV energy range. The primary interaction of photons in this energy range with matter is pair production, which can be used in a detector to determine the incident photons trajectory via the reconstruction of the trajectories of the electron-positron pair.

For the Fermi-LAT (a schematic is shown in figure 2.1), all incident radiation initially passes through the anticoincidence shield (ACD), which enables effective exclusion of charged particles from the gamma-ray photon analysis. The photons then interact within the layers of thin high-Z material and converted to electron-

positron pairs. The trajectories of the resulting pair are measured by particle tracking detectors and their energies measured by a calorimeter (a simulated image of this is shown in figure 2.2). Therefore, for a photon to be registered as being from a source, there must be (1) no signal in the anticoincidence shield, (2) more than one track starting from the same position in a tracker, and (3) an electromagnetic shower in the calorimeter for effective determination of the photon energy.

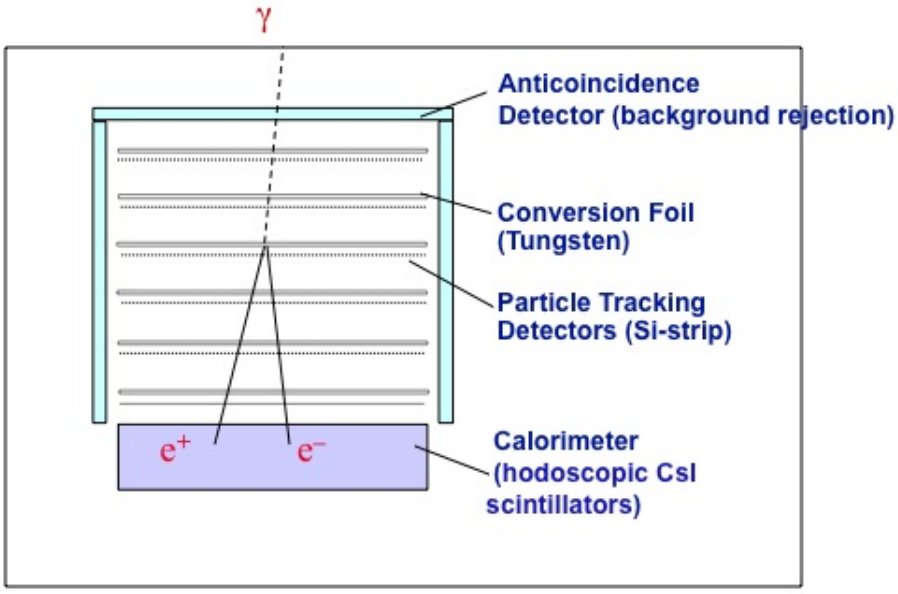

Figure 2.1: *Schematic of Fermi-LAT showing the anticoincidence shield, pair conversion telescope and the calorimeter. The telescope is 2.8 m tall. The tiled anticoincidence detector enables effective exclusion of cosmic rays from the gamma-ray photon analysis. The pair conversion telescope is composed of interlaced layers of tungsten converters and silicon strip trackers so. Below the pair telescope is the calorimeter consisting of an array of 1536 caesium iodide scintillator crystals which give effective energy resolution up to 300 GeV.*

The Fermi-LAT is arranged in a 4 x 4 array of identical towers (which are 40 x 40 cm^2), each containing a tracker, calorimeter and a data acquisition module. The tracker in each tower consists of 16 layers of tungsten converters and 18 layers

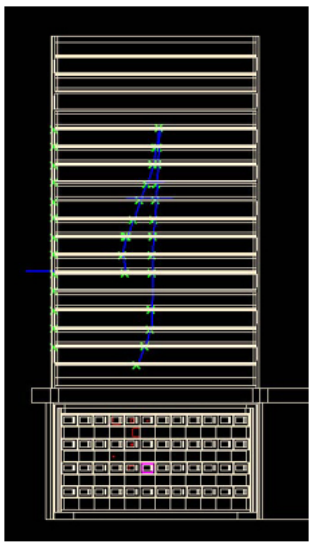

Figure 2.2: *Simulated image showing an event propagation through the Fermi-LAT tracker and energy deposition in the calorimeter. The pair production particles can be seen with each hit of the tracker represented by green crosses and the reconstructed path shown in blue. Image from* http://www.glast.sonoma.edu/multimedia/latsim/lat/ .

of silicon strip detectors designed to be highly efficient and with good positional resolution. Angular resolution is energy dependant such that the 68% containment radius is 3.5^o at 100 MeV, improving to 0.6^o at 1 GeV. The 16 tungsten converters are separated into 12 thin layers of 0.03 radiation length (where 1 radiation length in tungsten is 8 grams cm^{-2}) at the top of the instrument, followed by 4 thick layers of 0.18 radiation length in the bottom section.

Below the tracker lies the calorimeter consisting of an array of 1536 caesium iodide scintillator (CsI) crystals arranged in 8 layers. The calorimeter is in a hodoscopic arrangement, giving both longitudinal and transverse information about the energy deposition pattern and maximising cosmic ray rejection and shower leakage correction. The crystals are read out by photodiodes on each side and provide three spatial coordinates: one coordinate given by measuring the light

yield asymmetry between the ends of the crystal along its long dimension, and two coordinates from the location of the crystal in the array. The total length of the calorimeter is 8.5 X_0 (where X_0 is the radiation length) so that showers produced by photons of energies < 100 GeV are fully enclosed. However, for photons with energies greater than 100 GeV where the shower extends to the outside of the calorimeter, the shape of the shower outside the calorimeter is reconstructed based on the shape of the shower within the calorimeter. This technique can be applied to photons up to an energy of approximately 300 GeV. It must be noted that the Fermi-LAT is most efficient in its energy resolution at the energy range of 1 GeV - 10 GeV where the energy resolution is between 8% - 9%. The energy resolution then becomes less effective as we get to higher energies and at 300 GeV it is approximately 18% (Ackermann *et al.*, 2012).

The Fermi-LAT is surrounded by an anticoincidence detector consisting of 89 plastic scintillator tiles for not only effectively removing charged particles from the gamma-ray counts but to also minimise self veto. Prior to the Fermi-LAT, anticoincidence shields were constructed of one piece rather than a tiled system used in Fermi-LAT. This would effectively reduce the photon counts as any trigger in the anticoincidence shield would invalidate a photon detected at the same time in the tracker. The tiled system used in the Fermi-LAT means that only photons that are reconstructed to be coming from a tile with a trigger at the same time will be vetoed. The Fermi-LAT design required an efficiency exceeding 0.997 for detection of single charged particles entering the field of view of the telescope. Each scintillator tile contains wavelength shifting fibres which are connected at their ends to two photomultiplier tubes. The tiles are overlapping so as to minimize inefficiencies along one dimension. The anticoincidence detector is covered by a

micrometeorid shield (thickness of 0.39 g cm^{-2}) to protect it from debris hitting its surface.

The data acquisition module collects information from the subsystems, generates triggers for the instruments and provides onboard filtering which reduces the rate of downlinked events. The tower electronics module (TEM) provides the interface for the tracker and calorimeter modules. The information from the TEM and ACD is collected by a global unit which builds events based on this information and sends them to the two onboard event processor units (EPUs). The minimum read-out time per event is 26.5 μs, which is a result of the transmission of the trigger signal between different units. The two EPUs filter the data in order to reduce contamination by charged particles as most events triggered in the LAT are due to CR interactions. The onboard analysis maximizes the detection of gamma-rays whilst keeping the background within the downlink bandwidth limit ($\approx$ 500 Hz). However, all events (including background) exceeding an energy threshold of 10 GeV are downlinked for analysis on Earth since the rate is low.

The Fermi orbit crosses the South Atlantic Anomoly (SAA), which hosts geomagnetically trapped particles with several orders of magnitude greater flux than that observed in the rest of the orbit. This radiation would saturate the the tracker electronics and reduce lifetime so the LAT does not take data during the passage in the SAA. The switch off time in the SAA was defined prior to launch and evaluated during the commissioning phase so that there is only a 13% loss in total observing time.

2.2.1 Pair Production

Pair production is the main method used by the Fermi telescope to detect gamma-rays. It is the process in which a photon disappears and gives rise to an electron and positron pair. It can only occur in a Coulomb force field. Pair production usually occurs near an atomic nucleus but can also occur in the field of an atomic electron with much lower probabilities and is not considered here. Pair production near an atomic nucleus requires a minimum photon energy of $2m_0c^2 = 1.022$ MeV.

Figure 2.3 schematically shows a pair production event in a nuclear field. The incident photon hv transfers all of its energy in the creation of the electron and positron pair with kinetic energies T^- and T^+. The energy conservation equation for pair production is given by equation 2.1

$$\begin{aligned} hv &= 2m_0c^2 + T^- + T^+ \\ &= 1.022MeV + T^- + T^+ \end{aligned} \tag{2.1}$$

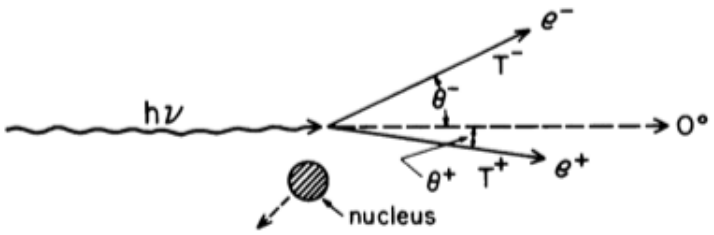

Figure 2.3: *Pair production schematic showing an incident photon vanishing to give rise to an electron and positron pair. The nucleus is there for conservation of momentum but receives negligible energy with the majority of the kinetic energy going to the electron-positron pair (schematic from Attix (1987)).*

The average kinetic energy received by the electron and positron pair is given

by equation 2.2. However, the electron and positron do not necessarily receieve equal energies.

$$\overline{T} = \frac{h\nu - 1.022MeV}{2} \tag{2.2}$$

The higher the $h\nu$ value above the threshold energy $2m_0c^2$, the smaller the angle between the electrons and positrons. The average angle of departure for the electrons and positrons from the original direction of the photon is given by equation 2.3. For example, a photon with energy 10 MeV will mean $\overline{T} = 4.489$ MeV and $\overline{\theta} \cong 0.11$ radians $= 6.5°$.

$$\overline{\theta} \cong \frac{m_0c^2}{\overline{T}} \qquad \text{(radians)} \tag{2.3}$$

2.3 Event Reconstruction and Classification

2.3.1 Fermi-LAT Monte Carlo Modeling

Once the data arrives on Earth, it is processed before being made available for public access. The process involves the determination of the direction and energy of candidate gamma-rays and the event classification required to reduce background contamination. The whole process was developed with and relies heavily on detailed Montecarlo (MC) simulations of the telescope. Fermi-LAT MC simulations are based on GLEAM (GLAST LAT Event Analysis Machine, details can be found in Boinee *et al.* (2003)). GLEAM makes use of different gamma-ray source and background models (such as neutrons, charged CRs and Earth limb gamma-ray emission, see Ormes *et al.* (2007) for more details). In particular, the

event simulations are based on the Geant 4 MC toolkit (Allison *et al.*, 2006). The MC simulations were then validated by using a calibration unit made from identical components to the Fermi-LAT (including two tracker and calorimeter towers). The calibration unit was exposed to a beam-test campaign including photons (up to 2.5 GeV), electrons (between 1 - 300 GeV) and hadrons (between several GeV to 100 GeV). The beam testing enabled the fine tuning of detector modeling and the selection of appropriate Geant 4 interaction models that best represented real events. More details on the calibration unit and the beam testing can be found in Baldini *et al.* (2007).

2.3.2 Event Tracking and Energy Reconstruction

Hits in the tracker that are spatially adjacent are combined in to a cluster, which determines a 3D position in the detecter. These clusters are then combined and two different algorithms are used to generate track hypotheses. The first algorithm uses the centroid and axis of energy deposition in the calorimeter; within an appropriate temporal window, a cluster is chosen at random and another searched for on the line connecting the first to the deposition centroid in the calorimeter. If the second is found, an initial track hypothesis is formed and populated using a version of the Kalman filter (Fruhwirth *et al.*, 2000), propagating clusters to the subsequent layer. This process is iterated over all the possible clusters until a track is found of high enough quality (i.e. the straightest and longest track) from the Kalman fit, which is then retained as the best track. The second algorithm is used when there is insufficient calorimeter information for track finding. This generally occurs with low particle energies or inclination angles within the tracker. The method is similar to the first one but the second cluster is chosen at random in the next

closest layer to the calorimeter.

The single tracks are then combined into vertices. The best fit track is combined with the second best track, which is chosen from the same associated event. If the second track approaches the first to within 6 mm, a vertex solution is found. This process is repeated with subsequent unused tracks from the same event, with tracks that are not satisfactorily paired being assigned to a vertex by themselves.

For the energy reconstruction, the raw signals for each crystal end are converted into energy deposition, which provides us with a 3D array of energies with total energy and position for each crystal. The moments of energy deposition in each crystal combined with the 3D centroid provide us with the direction of the shower. The sum of the energies deposited in the crystals provides the initial estimate of the event energy. Corrections are applied to this initial estimate of the energy based on the shower track direction, which can be used to estimate energy leakage from the back and sides of the calorimeter. Further corrections are also applied with low energy ($\lesssim$ 100 MeV) events as a significant fraction of the energy can be deposited in the tracker, which must be estimated and contributed to the energy estimated by the calorimeter.

2.3.3 Classification and Background Rejection

Before the final data sample is made available for public access, it must first be classified. This involves the selection of the best estimate of the event direction and energy, as well as dramatic reductions in background signals from the sample. This is achieved by a combination of classification tree (CT) generated probabilities (Breiman *et al.*, 1984) and a selection criteria. For the energy estimate, a CT is used to find the best energy estimate and another CT is used to evaluate the

probability that the measured value is within 68% of the true value. For the direction estimate, the events are initially divided into four catagories based on the conversion point in the tracker (front or back section) and vertexing properties (either vertex or single track). A CT is then used on each catagory to evaluate the probability that the measured direction is within 1σ of the true arrival direction. The events are then merged so that each event has a best energy and direction as well as the corresponding estimate of the accuracy.

Background events triggering the Fermi-LAT exceed the gamma-ray events by 10^5 and therefore must be significantly reduced before the data are ready for public use. The onboard filter is designed to reduce the signal-to-noise ratio down to $\sim 1 : 300$ in order to fit the available bandwidth for data downlink to Earth. The background signal is further reduced at Earth by three orders of magnitude. The main component of the Fermi-LAT responsible for background reduction is the ACD, which is combined with measured tracks. Events that are found to have tracks leading to hits in the ACD are removed. Furthermore, events that have tracks leading to gaps in the ACD are also discarded, which leads to an efficiency loss of $\sim 2\%$. CTs are also used to estimate the probability of events being background or not based on the event topology in the tracker and the shower profile in the calorimeter.

In order to help with source analysis, a few event classes were defined pre-launch that have different efficiencies and background contamination. The *Diffuse* class was designed to have a background rejection factor of the order of 10^6 and efficiency for gamma-ray detection of $\sim 80\%$. The *Transient* class has the largest efficiency but with background residuals at the gamma-ray detection rate. The *Dataclean* class (defined after launch) was specifically developed for the study of extragalactic

gamma-ray background. It must be noted that all event classes have a residual background contamination. The majority of these background contaminations are caused by background particles interacting with materials surrounding the Fermi-LAT and producing real gamma-rays that then enter the detector. The remaining minority background contamination is caused by events that have not been correctly identified as being background.

2.4 Instrument Response Functions

The Fermi-LAT performance is primarily dependent on hardware design, event reconstruction algorithms as well as background and event quality selections. The Instrument Response Functions (IRFs) describe the performance of the Fermi-LAT as a function of angular resolution, energy resolution and efficiency. The analysis classes (see Section 2.3.3) are based on different cuts for background elimination, effective area and the energy and spatial resolution. The IRFs are defined by three terms: point spread function, effective area and energy dispersion. The Point Spread Function (PSF) is the comparison between the reconstructed and true photon incident angles. The effective area is the efficiency of the Fermi-LAT for detecting gamma-rays and is derived from Monte Carlo simulations. The energy dispersion is the comparison between the reconstructed and true photon energies. These are discussed in turn in sections 2.4.1 - 2.4.3.

2.4.1 Point Spread Function

The Point Spread Function (PSF) is the probability distribution for the reconstructed direction of the incident gamma-rays from a point source. It is the primary

concern for point source analysis as the distribution of photons in the field of view is fundamental in distinguishing between sources. For optimal results, gamma-ray pair production must be measured immediately after a conversion in the tracker as multiple scattering of the pair particles (the e^- and e^+) and bremsstrahlung production will impact on the telescope's resolution. For example, missing the first hit in the silicon tracker at 100 MeV results in a loss of resolution by a factor of two (Atwood *et al.*, 2009).

Achieving a balance in the thickness of the tungsten converter is vital for the optimisation of the PSF. Thinner converters achieve a good PSF at lower energies as it is primarily determined by the $\sim 1/E$ dependence of multiple scattering. However, thicker converters offer increased effective area which is important at higher energies. The Fermi-LAT achieves a balance of both by using 16 tungsten converters separated into 12 thin layers of 0.03 radiation length at the top of the instrument (referred to as the "front") followed by 4 thick layers of 0.18 radiation length in the bottom section (referred to as the "back"). See Section 2.2 for details on tracker design.

The PSF is defined in terms of a scaled-angular deviation[1]:

$$\delta p = \left| \hat{p'} - \hat{p} \right| \tag{2.4}$$

Where $\hat{p'}$ is the reconstructed direction and $\hat{p}$ is the true direction of the photon.

$$x = \frac{\delta p}{S_p(E)} \tag{2.5}$$

[1]For more information, see http://fermi.gsfc.nasa.gov/ssc/data/analysis/documentation/Cicerone/Cicerone_LAT_IRFs/IRF_PSF.html

Where the scale factor $S_p(E)$ describes the variation of the PSF with energy and is given by (when E is expressed in MeV):

$$S_p(E) = \sqrt{\left[C_0 . \left(\frac{E}{100MeV}\right)^{-\beta}\right]^2 + C_1^2} \tag{2.6}$$

The parameters for C_0 and C_1 have fixed values depending on whether the event was converted in the front or back of the tracker. The value for β is shared between the front and back. Table 2.2 shows the values used with respect to the different event classes. The values were originally calculated based on Monte Carlo simulations but values for event classes P7SOURCE_V6 and P7CLEAN_V6 have since been updated with in-flight data. Graphical representation of the 68% and 95% containment angles as a function of energy for the P7SOURCE_V6 event class is shown in figure 2.4.

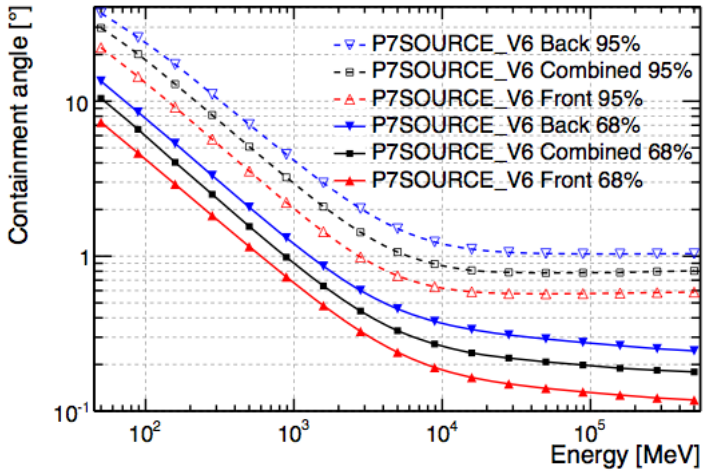

Figure 2.4: *Graphical representation of the 68% and 95% containment angles as a function of energy for the P7SOURCE_V6 event class. Figures from Ackermann* et al. *(2012)*

	C_0 Front	C_1 Front	C_0 Back	C_1 Back	β	Version
P7TRANSIENT_V6	$5.80e^{-2}$	$3.77e^{-4}$	$9.60e^{-2}$	$1.30e^{-3}$	0.800	Monte Carlo
P7SOURCE_V6	$2.45e^{-2}$	$5.68e^{-4}$	$4.18e^{-2}$	$1.34e^{-3}$	0.778	In-Flight
P7CLEAN_V6	$2.47e^{-2}$	$5.99e^{-4}$	$4.00e^{-2}$	$1.32e^{-3}$	0.778	In-Flight

Table 2.2: *The values used for different event classes in calculating the scale factor. The values were originally calculated based on Monte Carlo simulations but values for event classes P7SOURCE_V6 and P7CLEAN_V6 have since been updated with in-flight data.*

2.4.2 Effective Area

The effective area (A_{eff}) is defined as the detector surface area perpendicular to an incident photon under an assumed detection efficiency of 100%. However, for the Fermi-LAT, the A_{eff} is dependent on the geometrical cross section as well as the efficiency for gamma-rays to be converted and correctly identified. Due to the complex nature of calculating these, Monte Carlo simulations are used to evaluate A_{eff}, which is then updated with in-flight data. The A_{eff} is defined as a function of the incident gamma-ray photons energy and direction within the Fermi-LAT tracker.

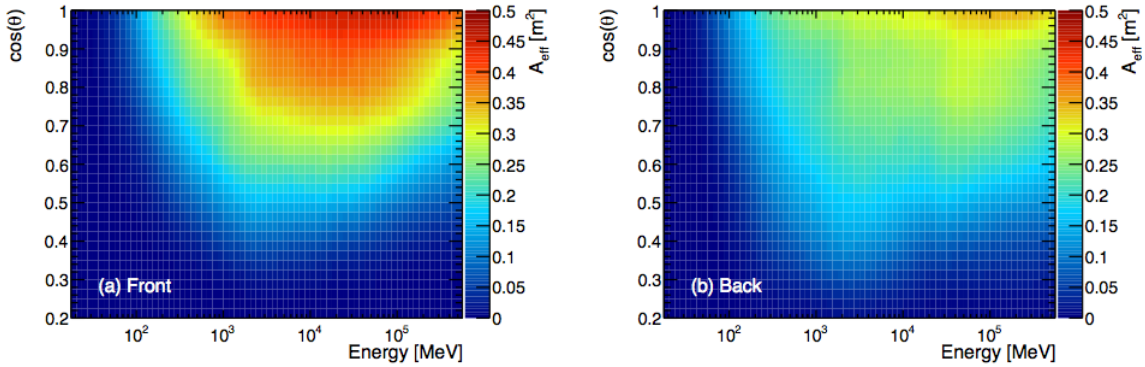

Figure 2.5: *Graphical representation of the effective area as a function of energy and incident angle. The plots are for the P7SOURCE_V6 event class, showing the front and back sections of the Fermi-LAT. Figures from Ackermann et al. (2012)*

2.4.3 Energy Dispersion

The energy dispersion can be defined as the fractional difference between the reconstructed energy (E$'$) and the true energy (E) of the events:

$$\frac{\delta E}{E} = \frac{E' - E}{E} \tag{2.7}$$

For the Fermi-LAT, the energy dispersion is of order 15%. Since the LAT covers 4 orders of magnitude in energy (between 30 MeV to 300 GeV), for many source analyses the energy dispersion can be neglected. The energy resolution as a function of energy on axis and incidence angle at 10 GeV for the P7SOURCE_V6 event class is shown in figure 2.6.

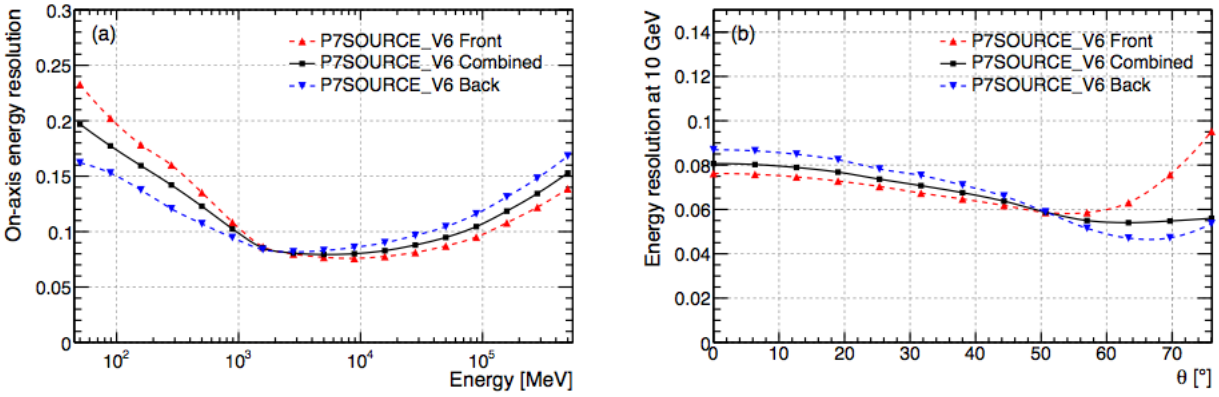

Figure 2.6: *Energy resolution as a function of energy on-axis (a) and incidence angle at 10 GeV (b). The plots are for the P7SOURCE_V6 event class, showing the front and back sections of the Fermi-LAT. Figures from Ackermann* et al. *(2012)*

2.5 Fermi Data Analysis

The full Fermi data are available online at http://fermi.gsfc.nasa.gov/ssc/data/access/ where the user can specify parameters for a source of interest and download for analysis. The parameters required for data access are source name or coordinates, observed time range and energy limits of interest. For all sources analysed in this thesis, a radius of 30° centred on the source was chosen with a time range from the start of Fermi observations to the date of data download from the server. The energy range was also constrained to within 100 MeV to 300 GeV for all sources. Although the Fermi-LAT can detect sources down to 30 MeV, the higher energy threshold of 100 MeV was chosen so as to reduce background contamination during the data analysis. The initial acceptance radius around the source will vary with analysis type and source location. For example, performing a spectral analysis on a point source in the Galactic plane will require a larger initial analysis region than for a source off the plane, to allow for fitting of multiple nearby sources. An acceptance cone radius of 10° is appropriate for spectral analysis of point sources off the Galactic plane, while 15° may be necessary for point sources located near the Galactic Plane. In order to keep all analysis consistent, the acceptance cone radius for all data was set to 15°. The output of the Fermi-LAT data extraction is a set of photon data files with the above cuts and the corresponding spacecraft file.

The flow chart for the full data analysis routine is shown in figure 2.7. After the download of the photon and spacecraft data files, they are then reduced at the data selection stage using the gtselect and gtmktime tools. The gtselect tool creates a new FITS file of selected rows from the input event data file based on

detailed user-specified cuts that are applied to each row of the input file. Typical selections are those involving time and energy range (minimum and maximum time and energy). Each applied data selection results in Data Subspace (DSS) keywords being written to the EVENTS header of the output FITS file describing the selection. This information is used later by analysis tools such as the likelihood tools. The gtmktime tool reads the spacecraft data file and, based on specific selection cuts, creates a set of good time intervals (GTI), which are then combined with existing GTIs in the event file, and all events outside this new set of GTI are removed from the file. Good time interval is a time range when the data can be considered valid. The default cut is to select times when the spacecraft is not in the Southern Atlantic Anomaly (SAA).

After the data selection cuts above, the next stage in the data reduction is to create an exposure map. The created exposure map consists of an integral of the total response over the entire region of interest (RoI) data-space. Therefore, separate exposure maps must be made for every distinct set of DSS cuts. There are two tools needed for generating exposure maps, gtltcube and gtexpmap. The Fermi-LAT instrument response functions are dependant on the angle between the direction to a source and the instrument z-axis. Therefore, the number of counts detected for a source of a given intensity is dependant on how long that source spends at various inclination angles over the course of an observation. The number of counts will also depend on accumulated time during which the Fermi-LAT is actively taking event data (also known as the livetime). The gtltcube tool uses the spacecraft data file along with the GTI selections in the event file to compute livetime cubes that cover the entire sky. One of the advantages to producing the livetime cubes for the entire sky is that the output can be used to generate

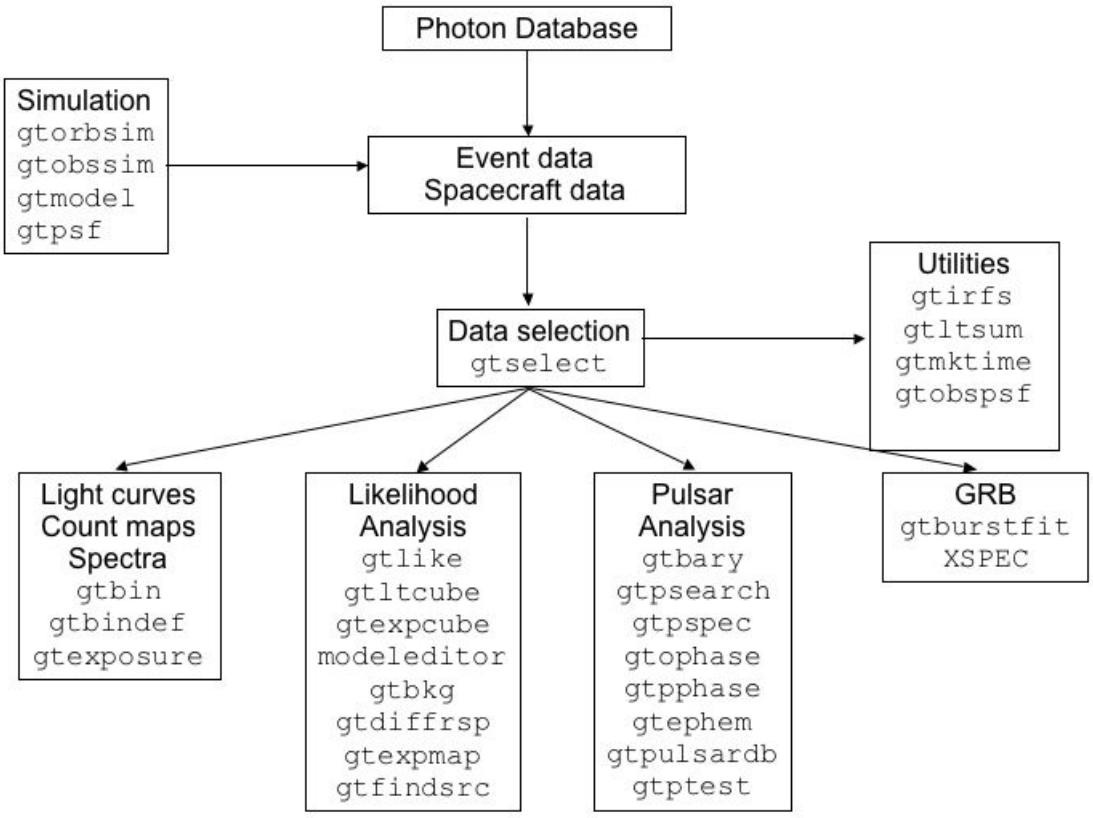

Figure 2.7: *Flow chart showing the tools used for Fermi analysis. Initial data reduction on the event and spacecraft data are done using gtselect and gtmktime. Further analysis is dependant on the source and the tools shown in each respective source type are the ones most commonly used. Note that tools are not constrained to specific source types and can be used for other analysis such as producing counts maps with gtbin and using the same tool for binned likelihood analysis. Figure from* http://fermi.gsfc.nasa.gov/ssc/data/analysis/scitools/overview.html .

exposure maps for regions of interest in other parts of the sky that have the same time interval selections.

After the production of a livetime cube using gtltcube, the tool gtexpmap is then used to produce exposure maps based on the event selection used on the input photon file and the livetime cube. It is typical to produce an exposure map that is larger than the acceptance cone radius specified for gtselect so as to ensure that photons from sources outside the ROI are accounted for owing to the size of the instrument point spread function. Note that the exposure map must be recalculated if the ROI, energy selection, zenith or the time interval selection of the events is changed.

Further analysis of the data will depend on what the user requires and on the source being analysed. For example, the pulsar analysis part of the flow chart shown in figure 2.7 lists tools that can be used to obtain pulsar timing and phase. For unidentified pulsars, gtephem can be used to deduce preliminary ephemeris and further analyses done with other tools. Note that analysis tools are not constrained to a particular part of the flow chart. For example, gtbin in the "Counts maps" can also be used when doing binned likelihood analysis.

Most Fermi-LAT analysis requires tools from the "Likelihood Analysis" path of the flow chart. The main tool in that chain is gtlike which can be used to find the significance of a source. The likelihood statistic L (see section 4.6) is the probability of obtaining observational data given an input model. In Fermi analysis, the input model is the distribution of gamma-ray sources in the sky, and includes their intensity and spectra, as well as taking into account the galactic and extragalactic contributions given the source region. The statistic can then be used to find the best fit model parameters including the description of a source's

spectrum, position and intensity. There are several spectral functions, with the most commonly used being the PowerLaw function which has the form:

$$\frac{dN}{dE} = N_0 \left(\frac{E}{E_0} \right)^{\gamma} \tag{2.8}$$

where N_0 is the prefactor, E_0 is the scale and γ is the index. For analysis in the 100 MeV to 300 GeV range, the scale parameter E_0 can be fixed to 100. However, for differential energy analysis such as in the 1 GeV - 5 GeV range, the scale parameter E_0 must be fixed with a value in that range (i.e. 2500 could be used for our example). The prefactor and index parameters are allowed to vary so that gtlike can fit them. For all sources, spatial parameters such as the RA and Declination are fixed.

Initial analysis of data was done manually using the tools with command line prompts. However, after the use of the tools was understood, several analysis scripts were developed so that analysis and plotting could be automated. Detailed analysis method and scripts that are used for sources in this thesis are explained in chapter 4.

All analysis in this thesis use the latest IRF[1]: Pass 7 version 6. This IRF is superior to the Pass 6 used at launch (Ackermann *et al.*, 2012) and includes updates from in-orbit performance of Fermi. The diffuse models for all analysis are the iso_p7v6 and can be found on the Fermi website[2]. Note that these models are continuously being updated and improved.

[1]For the latest IRF and improvements, see http://fermi.gsfc.nasa.gov/ssc/data/analysis/documentation/Cicerone/Cicerone_LAT_IRFs/IRF_overview.html

[2]For the latest diffuse models, see http://fermi.gsfc.nasa.gov/ssc/data/access/lat/BackgroundModels.html

Chapter 3

Current Status of Gamma-ray Binaries

The Fermi-LAT Collaboration has released two point source catalogues of the GeV sky. The first catalog (Abdo *et al.*, 2010) was released in 2010 and contained 1451 sources. The second catalog (Nolan *et al.*, 2012) was released in 2012 and contained 1873 sources, with only 127 of those sources firmly identified (based on factors such as matched spatial morphology, correlated variability and periodicity). Of the 127 identified sources, 83 are pulsars, 28 are AGN, 6 are supernova remnants, 4 are high mass binaries, 3 are PWN, 2 are galaxies and one is a nova. There are 572 sources in the second catalog that don't have any positional association with sources from other catalogs (such as X-ray and Radio catalogs). The remaining sources have positional associations (but not confirmed identification) with sources from other catalogs. The large number of unidentified sources means that interesting physics could be discovered and there is an active field of research in the identification of these sources.

3.1 Known Gamma-ray Sources

There are currently 5 known gamma-ray binaries[1] that have firmly been detected by Fermi.

3.1.1 LS I +61°303

LS I +61°303 was initialy proposed as a gamma-ray source more than 25 years ago based on the *CosB* detection (see figure 3.1). It was the third gamma-ray binary to be detected in the TeV domain (Albert *et al.*, 2006) and contains a B0.5Ve star and a compact object of unknown mass. The orbital period of the compact object is 26.5 days with an eccentricity of e $\approx 0.5 - 0.7$. The flux is highly variable with marginal detections at close to periastron (phase 0.23) and maximum flux of $\approx$ 16% of the Crab Nebula at apastron.

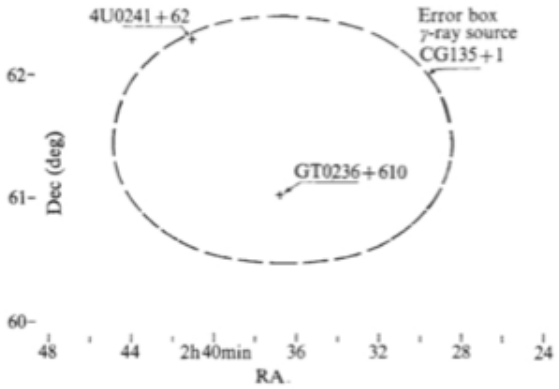

Figure 3.1: *The error circle of the Cos B source 2CG 135+01. There is a possible association with the binary LS I +61° 303 which is marked as the radio source GT0236+610. Figure from Gregory & Taylor (1978).*

LS I +61°303 is also detected by Fermi (Abdo *et al.*, 2009a). The emission

[1]PSR B1259-63, LS 5039, LS I +61°303, Cygnus X-3, 1FGL J1018.6-5856

is highly variable but the peak emission occurs immediately after the periastron passage suggesting an interesting and complex relationship with the TeV emission (see Section 2.1.1 for details on TeV emission and instrumentation). The power spectrum and phase folded light curve of the Fermi detection are shown in Figure 3.2. In March 2009, LS I +61°303 showed an unexpected ≈ 30% increase in flux with Fermi (Hadasch *et al.*, 2012). Interestingly, the increased flux resulted in the power of the observed binary orbital period decreasing until it was no longer detectable (see figure 3.3).

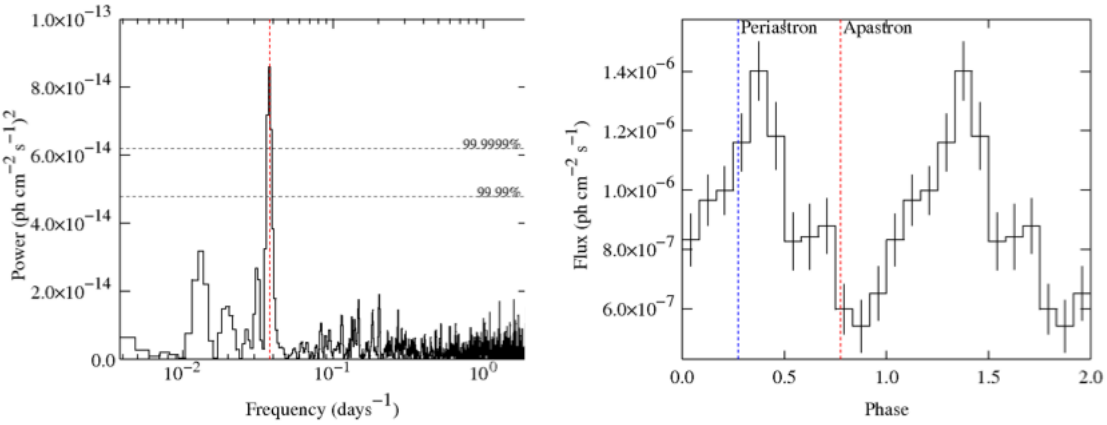

Figure 3.2: *The power spectrum (left) and phase folded light curve (right) of LS I +61° 303. The power spectrum shows the weighted Lomb-Scargle periodogram of the Fermi light curve with the vertical dashed line representing the known orbital period of 26.5 days. The horizontal dashed lines represent the the shown significance levels. The dashed lines on the phase folded light curve represent the periastron and apastron of the system. Figure from Hill* et al. *(2011).*

X-ray observations with Swift have shown regular emission period consistent with the orbital period of the system Esposito *et al.* (2007). The X-ray modulation is seen on multiple timescales. There is also a modulation on ≈ 4.5 year timescale (Chernyakova *et al.*, 2012), which is similar to the known 4.5 year modulation of the radio period (Gregory, 2002). However, there have neen no definitive links

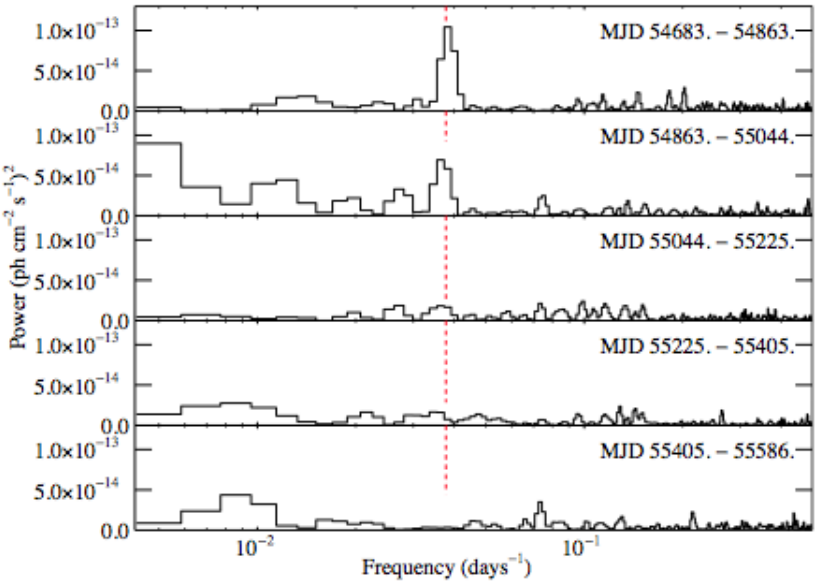

Figure 3.3: *The Lomb-Scargle periodograms of LS I +61°303 consisting of 30 months of Fermi data split into five consecutive segments. The earliest segment is at the top and the red line indicates the orbital period of the system (Hadasch* et al.*, 2012).*

between the processes producing the X-ray and radio emissions.

There is no consensus on the engine that powers the particle acceleration in LS I +61°303. It was originally thought to be a microquasar system due to the observation of extended radio jets by Massi *et al.* (2001). The system would be powered by a variably fed accretion disc, which would power a relativistic jet. The orbital period observed in radio, X-ray and GeV gamma-ray regimes could then be explained by the accretion disc's interaction to the varying levels of the strong stellar wind. However, this model does not explain the TeV emission being at a maximum near the apastron of the system.

Further observations in the radio have detected what appears to be the cometary emission from the interaction between the pulsar and stellar companion winds (Dhawan *et al.*, 2006). This is direct contradiction to the microquasar model and

classifies the system as a pulsar binary. In this scenario, the emission from the system would be powered by the shock front between the two winds and the variability is explained by the varying levels of the stellar wind density. However, this model also does not explain the detection of maximum TeV emission near the apastron of the system.

Furthermore, there have been no detections of accretion-like X-ray spectrum or pulsations from the system (Aliu *et al.*, 2013) so models containing a black hole or pulsar cannot be ruled out.

3.1.2 LS 5039

LS 5039 was first identified as a high mass X-ray binary by Motch *et al.* (1997) from a cross correlation of unidentified ROSAT X-ray sources with a catalogue of OB stars. LS 5039 is also within the 0.5° error box of the EGRET unidentified source 3EG 1824-1314 and Paredes *et al.* (2000) suggested it as a possible candidate. LS 5039 was first detected in the VHE by the HESS Collaboration (HESS Collaboration, 2005c) with orbital period of 3.9 days (Dubus *et al.*, 2005). The mass of the compact object is currently unknown but the orbit is slightly eccentric with e $\approx$ 0.35. There are some indications of a persistent jet-like feature suggesting a microquasar system (Paredes *et al.*, 2000) but there have been no detections of an accretion disc or accretion variability. In fact, there have been no indications of long term gamma-ray variability in the system (Hadasch *et al.*, 2012). Both the TeV and GeV emissions are modulated with the orbital period of the binary system but they are in anti-phase with each other (Dubus *et al.*, 2005).

Radio observations of LS 5039 show morphological information at milliarcsecond scales that cannot be explained with a microquasar model (Ribó *et al.*, 2008). X-ray observations show the absence of accretion features (Martocchia *et al.*, 2005) leading to the suggestion that the system is a pulsar-massive star binary (Dubus, 2006c).

Theoretical models have been suggested for the type of compact object in the system. The gamma-ray emission is produced by the inverse Compton (see section 1.3.1) scattering of the stellar light by very high energy electrons accelerated near the compact object. For a black hole companion, the gamma-ray emission would be from particles accelerated in the jet (Bednarek, 2007). The other scenario

would involve the relativistic wind of a young, rotation powered pulsar, where the particle acceleration could occur in the wind interaction region (Dubus, 2006c) or by a process within the pulsar wind Cerutti *et al.* (2008).

The Fermi Collaboration detected LS 5039 from 2008 August to 2009 June (Fermi LAT Collaboration, 2009a) and observed multiple orbits of the system. A power spectrum of the results is shown in Figure 3.4 and the known orbital period of 3.90603 days (Casares *et al.*, 2005) can clearly be seen. The phase folded light curve and the changes in hardness ratio are shown in Figure 3.5.

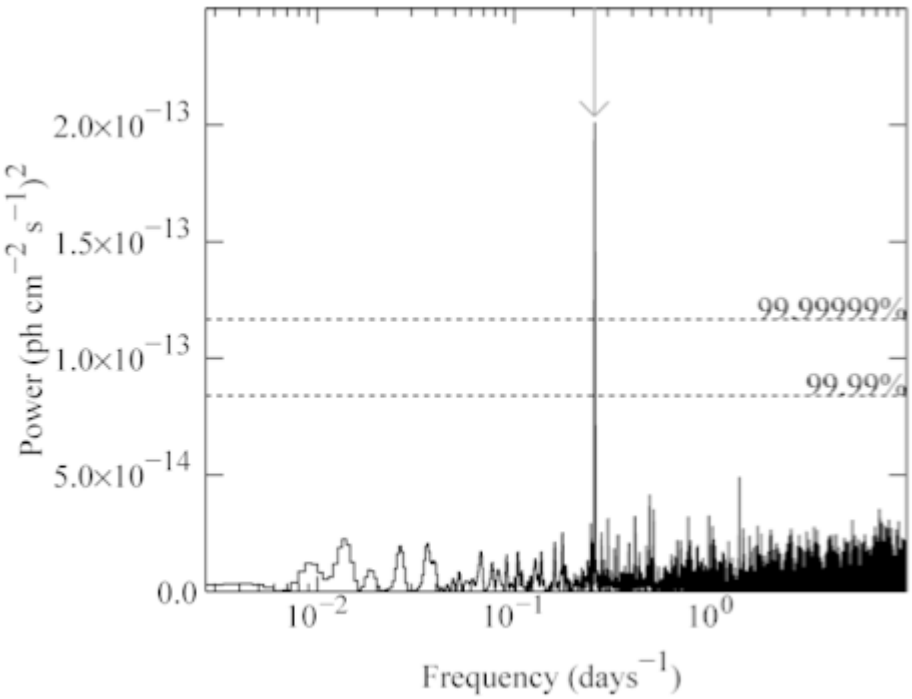

Figure 3.4: *Power spectrum of the LS 5039 light curve from Fermi. The arrow represents the known orbital period of 3.90603 days (Casares* et al., *2005). The dashed lines indicate the significance levels. Figure from Fermi LAT Collaboration (2009a).*

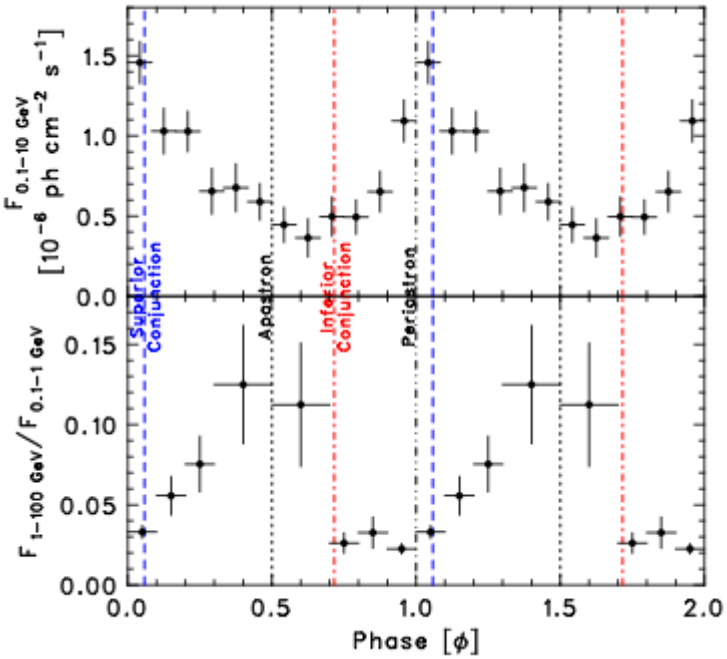

Figure 3.5: *Phase folded light curves of LS 5039 from Fermi observations. Top: Flux variations between 0.1 - 10 GeV with orbital phase. Bottom: The changes in hardness ratio across the orbit where the hardness ratio is given by flux(1100 GeV)/flux(0.11 GeV). Figure from Fermi LAT Collaboration (2009a).*

3.1.3 1FGL J1018.6-5856

1FGL J1018.6-5856 is the latest addition to the small list of gamma-ray binaries and was detected by Fermi (Corbet *et al.*, 2011) and found to exhibit periodic emission with a period of 16.6 days. It is one of the brighter Fermi catalogue sources (flux of 2.9 x 10^{-8} photons cm^{-2} s^{-1}) with a spectrum similar to a pulsar but with no detectable pulsations (Corbet *et al.*, 2011). Detections in the TeV domain are more complicated. HESS detects a point like source at the position of 1FGL J1018.65856 but there is also an extended structure (see Figure 3.6) that might not be associated with the binary system (de Ona Wilhelmi, 2011). No modulations are detected in the TeV which would confirm the possible connection to the GeV emission.

Swift X-ray observations of the region reveal a source consistent with the location of the gamma-ray source (see Figure 3.7). The source is highly variable in X-ray with 0.3 to 10 keV count rate ranging from $\approx$ 0.01 to 0.05 counts s^{-1} (The Fermi LAT Collaboration *et al.*, 2012). However, the highest count rates are obtained close to the epoch of maximum gamma-ray flux (top panel in Figure 3.8).

Radio observations of the region obtained with the Australia Telescope Compact Array (ATCA) at frequencies of 5.5 and 9 GHz. There is a radio source with positional coincidence to 1FGL J1018.6-5856, which is clearly variable (see Figure 3.8). However, unlike the gamma-ray and X-ray observations, the radio detection does not show any obvious brightening at phase zero.

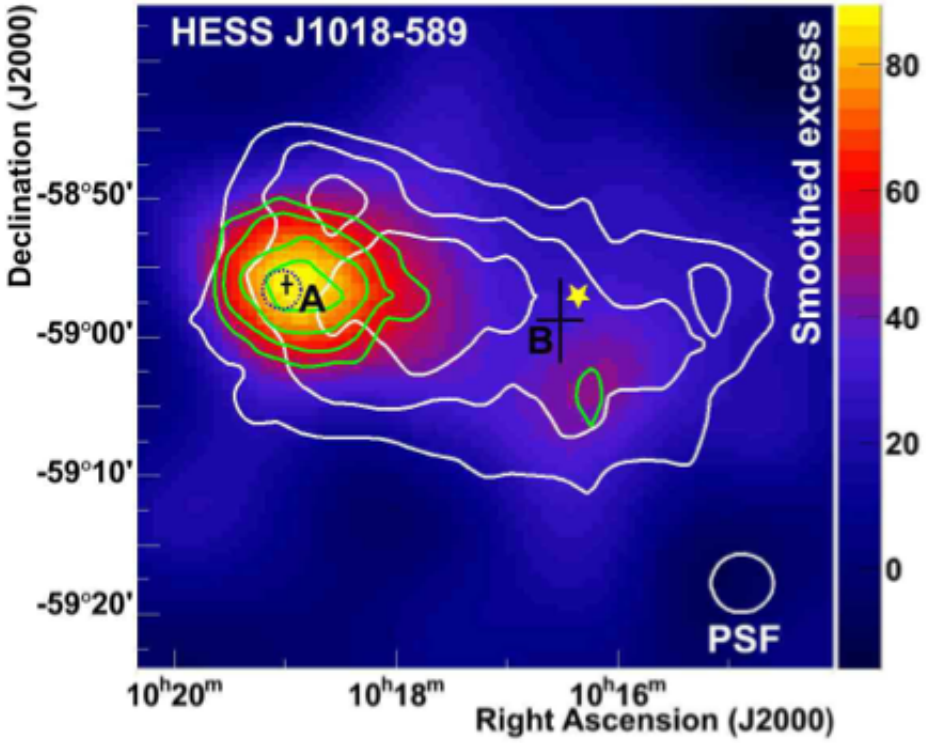

Figure 3.6: *HESS excess image of the HESS J1018589 region with Gaussian smoothing of width $\sigma = 0.07°$. The position of 1FGL J1018.6-5856 is shown with a blue dashed ellipse (at the 95% confidence level). The nearby pulsar PSR J10165857 is marked with a yellow star. Figure from HESS Collaboration (2012).*

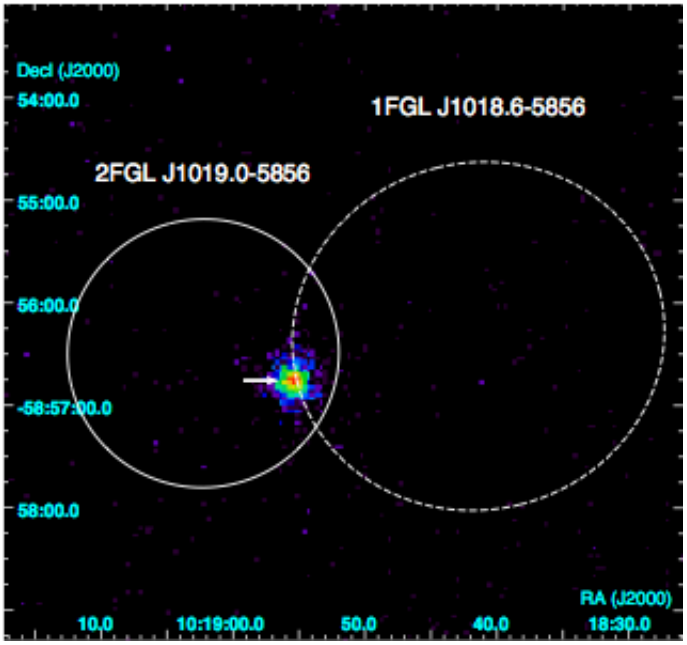

Figure 3.7: *Swift X-ray image of the region around 1FGL J1018.6-5856. The Fermi 95% confidence ellipses from the first (right) and second (left) catalogues are shown. The X-ray counterpart is marked by an arrow near the centre. Figure from The Fermi LAT Collaboration* et al. *(2012).*

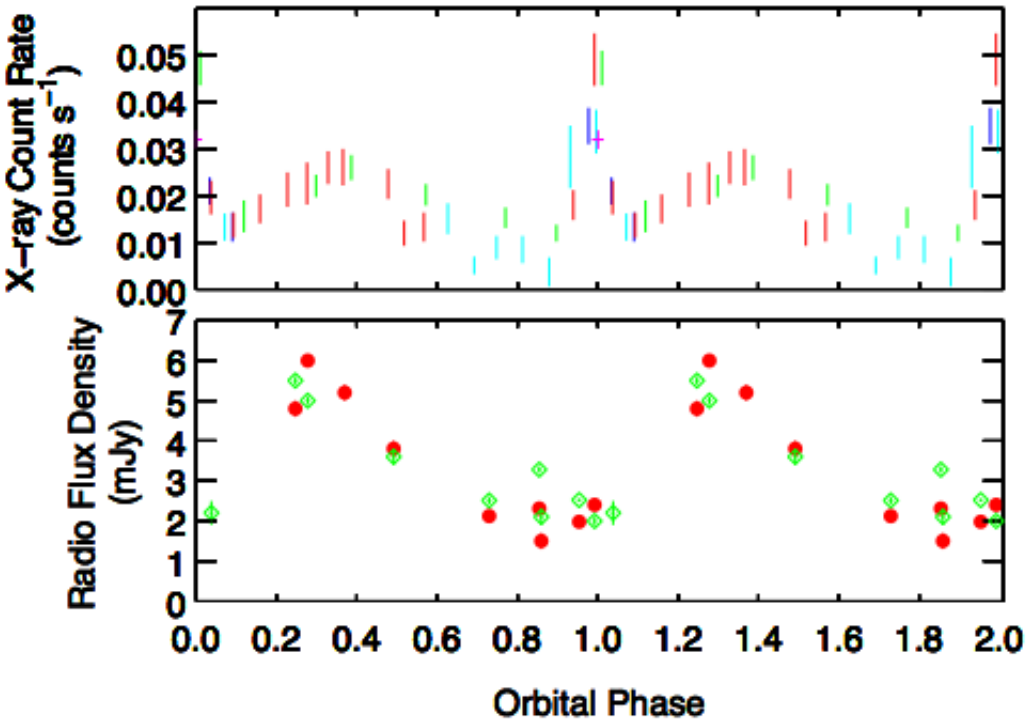

Figure 3.8: *X-ray (top) and radio (bottom) observations of 1FGL J1018.6-5856 folded on the binary orbital period. The X-ray observations are from Swift and cover the energy range 0.3 to 10 keV with the different colours representing data taken from different orbital cycles. The radio observations are from ATCA with the different colours representing data in 9 GHz (green) and 5.5 GHz (red). Figure from The Fermi LAT Collaboration* et al. *(2012).*

3.1.4 PSR B1259-63

PSR B1259-63 was discovered emitting at VHE using the HESS telescope array in 2004 (HESS Collaboration, 2005a) and became the first binary system to be established as emitting in VHE. The system is formed of a 48 ms pulsar and a Be star at a distance of 1.5 kpc (Tavani & Arons, 1997). It is believed that particle acceleration takes place at the shock between the pulsar wind and the wind of the stellar companion LS 2883 (HESS Collaboration, 2005a) resulting in gamma-ray emission (see Section 1.3 for explanation on gamma-ray emission mechanisms).

The orbit of the system is highly eccentric at e = 0.87 and has a period of 3.4 years. Apestron occurs at a distance of around 10 AU, while periastron happens at 0.7 AU. Near periastron, the pulsar travels through the stars circumstellar disc, which has an inclination of 10-40^o to the orbital plane. The stellar disc is inclined with respect to the orbital plane such that the pulsar passes through the disc shortly before and after the periastron passage (Wex *et al.*, 1998). The radio pulse is absorbed in the disc during the 15 days before and after periastron. A geometrical diagram of PSRB1259 during periastron is shown in figure 3.9. The interaction of the pulsar with the circumstellar disc during periastron is expected to produce a broad-band spectrum.

The X-ray flux changes with the orbital phase, increasing from $\approx 10^{12}$ erg cm^{cm} s^{-1} at apastron to $\approx 10^{11}$ erg cm^{cm} s^{-1} at periastron (Chernyakova *et al.*, 2009). The X-ray photon index also changes with the orbital phase with the hardest spectra of ≈ 1.2 occuring around the same time as the observed rapid increase in X-ray flux (Chernyakova, 2006).

No gamma-ray emission was detected from the source when it was far from peri-

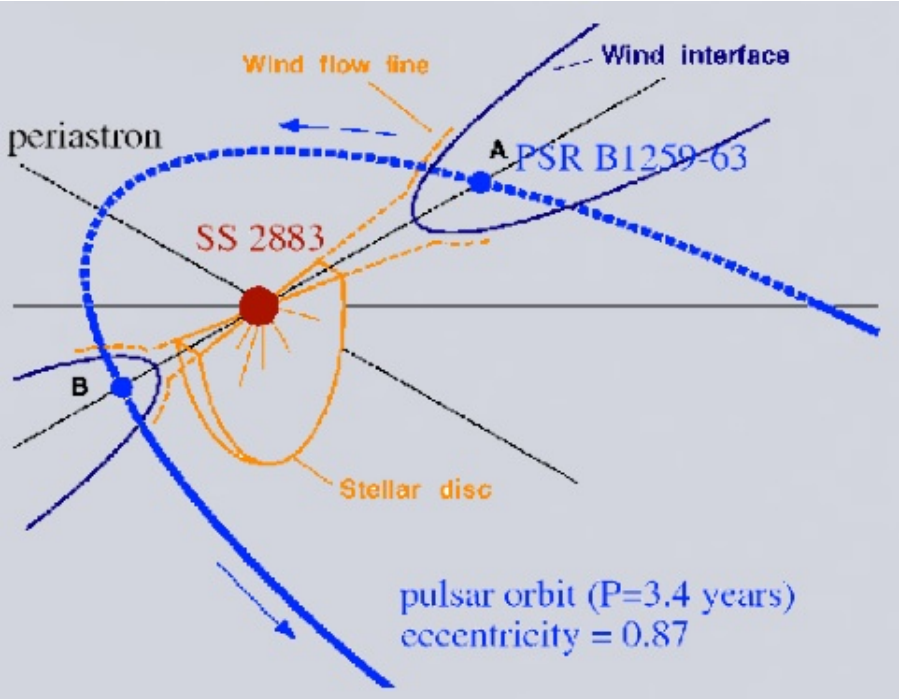

Figure 3.9: *Schematic showing the geometry of the PSRB1259 during periastron. Observations of the pulsed emission suggest that the pulsar orbit takes it through the excretion disc of its companion just before and after periastron. From our line of sight, the pulsar is behind the disc during periastron. Figure from Ball* et al. *(1998).*

astron. The Fermi Collaboration reported the detection of gamma-ray emission as the pulsar approached periastron Abdo *et al.* (2011). The gamma-ray flux peaked at approximately 30 days after periastron and started fading at approximately 57 days after periastron. The source was also observed in radio and X-ray simultaneously but showed no corresponding changes in flux between pre-periastron and post-periastron.

PSR B1259-63 was observed and detected independently from the Fermi Collaboration during the periastron of 2010 for this thesis using Fermi data and the results are shown in Section 5.3.

3.1.5 Cygnus X-3

Cygnus X-3 is a bright X-ray binary close to the Galactic plane at a distance of 7 kpc (Ling *et al.*, 2009). The nature of the compact object is still under intense debate with Stark & Saia (2003) suggesting a neutron star of 1.4 $M_{\odot}$ and Shrader *et al.* (2010) suggesting a black hole of approximately 10 $M_{\odot}$. The donor star has been identified as a Wolf-Rayet star (van Kerkwijk *et al.*, 1996), which classifies the system as a high-mass X-ray binary. However, observations in both X-rays and infrared emissions show a short orbital period of 4.8 hours, which is typical of low-mass binary systems.

The system can produce outflows containing energetic particles that are accelerated away from the compact object up to relativistic speeds in collimated jets. These high energy particles are entangled in the magnetic field of the jet and lose their energy via synchrotron (see section 1.3.2) and/or inverse Compton (see section 1.3.1) emission, resulting in a broad-band spectrum from radio up to gamma-rays (see Georganopoulos *et al.* (2002), Atoyan & Aharonian (1999), Romero *et al.* (2003) for details).

Cygnus X-3 is interesting as it displays bright radio emission during outbursts that last for several days and reveals the presence of collimated relativistic jets (Miller-Jones *et al.*, 2004), which classifies the system as a microquasar. In fact, Cygnus X-3 is one of the brightest Galactic transient radio sources (Mioduszewski *et al.*, 2001). The X-ray spectrum changes between hard and soft states similar to those observed in other accreting X-ray binaries, and is heavily absorbed at low energies by the dense stellar wind (Hjalmarsdotter *et al.*, 2009).

Historically, Cygnus X-3 has attracted a great deal of attention due to claims

of detection at TeV and PeV gamma-rays (for example Brazier *et al.* (1990)). In 1985, Chadwick *et al.* (1985) reported the detection of an enhancement which coincided with the X-ray phase maximum. A period search of the data between 10 ms and 50 seconds revealed the best candidate period of 12.5908 ms with a chance probability after all the tries were taken into account of 3.3 x 10^{-3}. This result was corroborated by Gregory *et al.* (1990) who found the 12.6 ms periodicity at 100 TeV. However, other groups (such as the Whipple group) did not see the 12.6 ms periodicity (Fegan *et al.*, 1987).

Modern instruments with improved sensitivity have failed to confirm those claims for energies above 500 GeV (Albert & the MAGIC collaboration, 2008). Nevertheless, Cygnus X-3 is a good candidate for high energy gamma-ray observations as a microquasar with strong X-ray and radio emission. It has already been detected by AGILE (AGILE Collaboration, 2009b) with five gamma-ray flares above 100 MeV. The Fermi LAT Collaboration have also reported on the detection of Cygnus X-3 (Fermi LAT Collaboration, 2009b) with clear evidence of the orbital period (see Figure 3.10). However, the 4.8 hour orbital period is only detected during periods of enhanced emission. The Fermi entire data set does not show the orbital period.

Cygnus X-3 was observed and detected for this thesis using Fermi data and the results shown in Section 5.2.

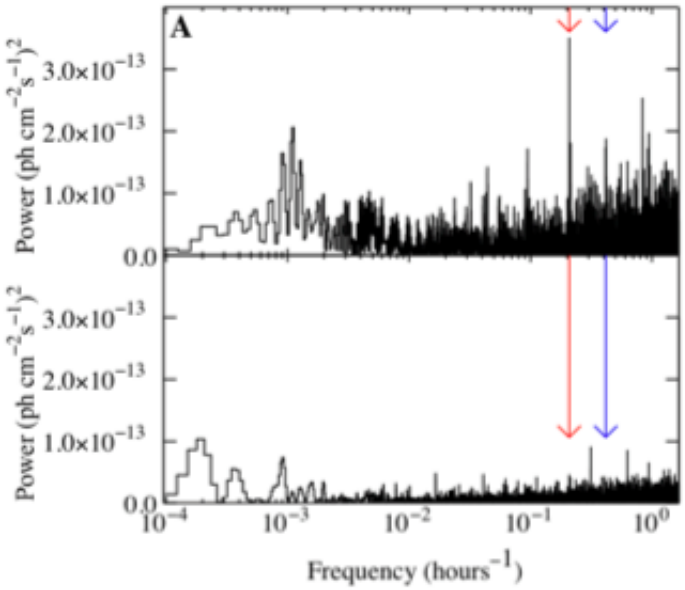

Figure 3.10: *The Fermi power spectrum for Cygnus X-3 showing the frequencies of the orbital period (red arrow) and the second harmonic (blue arrow). The results for the periods of enhanced emission (top) and for the entire data set between August 2008 and September 2009 (bottom) are shown. Figure from Fermi LAT Collaboration (2009b).*

3.1.6 Summary

Gamma-ray binaries have definitively been detected in the GeV regime as well in radio and X-rays. Most are also detected in the TeV regime. Table 3.1 shows a summary of known gamma-ray binaries that have been detected with Fermi.

Source	P_{orb} (days)	Compact Source	Companion	Detected
LS I +61°303	26.5	Pulsar?	Be	Radio, X-ray, GeV and TeV
LS 5039	3.9	Pulsar?	O6.5V	Radio, X-ray, GeV and TeV
1FGL J1018.6-5856	16.58	Pulsar?	O6V	Radio, X-ray, and GeV
PSR B1259-63	$\sim$ 1240	Pulsar	Be	Radio, X-ray, GeV and TeV
Cygnus X-3	0.2	Black hole?	Wolf-Rayet	Radio, X-ray, GeV and TeV

Table 3.1: *Gamma-ray binaries with confirmed detections from Fermi showing the binary period (in days), compact and companion source types as well as the energy regimes that have detected with. Results with (?) are not confirmed.*

LS I +61°303 and LS 5039 have both been detected with clear signs of orbital modulation in the Fermi observed flux with the GeV flux peaking around periastron for both sources. Both orbital modulations of the GeV flux was found to be anti-correlated with the observed modulations at TeV energies.

1FGL J1018.6-5856 is the latest addition to the list of gamma-ray binaries and

was detected by Fermi (Corbet *et al.*, 2011) with a period of 16.6 days. The TeV image of the region shows an extended source with no modulations that could confirm association with 1FGL J1018.6-5856. The source has also been detected in X-ray (Swift) and radio (ATCA). Both show variability consistent with the Fermi observations. However, the gamma-ray and X-ray observations show obvious brightening at phase zero, which is absent from the radio observations.

PSR B1259-63 is the only known millisecond pulsar in a binary system with a main sequence star and was detected by Fermi (Abdo *et al.*, 2011) near periastron. The gamma-ray flux peaked at approximately 30 days after periastron and started fading at approximately 57 days after periastron. Radio and X-ray simultaneous observations show clear detections of the source but no orresponding changes in flux between pre-periastron and post-periastron

Cygnus X-3 was firmly detected by Fermi (Fermi LAT Collaboration, 2009b) and confirmed the microquasar as a source of gamma-ray emission. The Fermi detections show the 4.8 hour orbital period of the system. Furthermore, the gamma-ray emission is correlated with radio flaring events.

Chapter 4

Techniques

4.1 Temporal Analysis

Temporal variation of the observed flux from X-ray binaries is not only common, but is to be expected given the dynamic nature of these systems, which harbour rapidly evolving radiative environments. Important information regarding the physical processes taking place in binary systems is embedded within the observed temporal characteristics. Radio observations of variability in binary systems have revealed rapid changes in flux density, which can correspond to the production of ultra-relativistic ejecta (Fender, 2006). X-ray observations have revealed insights into the process of accretion in strong gravitational fields (Romero *et al.*, 2003).

For binary systems, the most relevent variability search is for periodic variability due to an inherent periodicity due to the orbital motion. Under the assumption that gamma-ray production occurs within a region of the binary system undergoing regular environmental changes due to the binary orbit, it is reasonable

to expect observable periodic modulation in the gamma-ray flux (Dubus, 2006a). For example, PSR B1259-63 is a binary system with a period of 3.4 years and is only detectable in gamma-rays during periastron (see section 5.3 for analysis and results).

Periodic gamma-ray signals are vital for the identification of multi-wavelength counterparts. Potential source confusion is effectively eliminated if observed gamma-ray modulations are consistent with established periodicities at other wavelengths. For example, gamma-ray detections of Cygnus X-3 can only be confirmed with the observation of the 4.8 hours orbital period that was previously observed via X-rays and infrared (see section 5.2).

4.2 Statistical Techniques

The majority of gamma-ray observations in search of pulsed emission are made with low signal to noise ratios and are typically dominated by counting statistics. Therefore, regular modulations are usually not possible to observe directly by, for example, a plot of counts as a function of time. Statistical techniques are required to identify periodic emission in data dominated by background emission.

Statistical techniques test the null hypothesis, defined here as the photon arrival times being randomly distributed and therefore exhibiting a uniform distribution of phase at all periods. If this null hypothesis is not consistent with the data, the alternative hypothesis - that periodic modulation due to a genuine source is present - must be accepted at some chosen level of confidence. A periodicity test is therefore a test of uniformity of phase, and any statistical significance identified in a time series is expressed as the degree of confidence that the null hypothesis

can be rejected.

There are several shapes of light curves that might be expected. For example, pulsars emitting observable gamma-rays during a large fraction of each rotation will have broad peaks in their light curves, but pulsars with tight beaming will typically have narrow peaks - and maybe more than one - in their light curves. In many cases, the expected light curve shape is not known, a priori, so the most effective test is one that can identify periodic components in the largest variety of light curve shapes. Although there are several techniques (see Feigelson & Jogesh Babu (2012) for general discussion), this section will discuss the three most commonly used in gamma-ray astronomy.

4.2.1 χ^2 Test

χ^2 tests whether the observed distribution of the deviations of an observed set of k histogram bins from the expected number in each bin is consistent (null hypothesis) with just statistical fluctuations. Often, the values in each bin will consist of just a number count of photons - in which case the fluctuations can be ascribed to Poisson fluctuations about the expected number in each bin. Take a data set with time series corresponding to n events folded to the candidate period p. In the case of a random time series, the number in each bin will be Poisson distributed with an expected number of E = $\frac{n}{k}$. The test statistic is given by

$$\chi^2 = \sum_{i=1}^{k} \frac{(O_i - E_i)^2}{E_i} \tag{4.1}$$

where O_i is the number of events observed in the i^{th} phase bin. The statistic is then distributed as χ^2 and the number of degrees of freedom, ν, is k - 1. The

distribution is "perfectly" uniform when the value of χ^2 is 0. Values of the reduced χ^2 ($= \chi^2/\nu$) $>> 1$ suggest fluctuations greater than expected under the null hypothesis. Equally, if $\chi^2/\nu << 1$, the fluctuations appear too small to be attributed to the null hypothesis.

The significance of any periodic component in the data are expressed as the probability that any periodicity observed has arisen by chance:

$$Pr(\text{null hypothesis is true}) = Pr_\nu(\chi^2 > \chi_0^2) \tag{4.2}$$

where ν is the number of degrees of freedom, χ_0^2 is the value of the observed statistic and Pr_ν is obtained from reference tabulated probabilities. The tables for Pr_ν assume Gaussian distribution, to which the Poissonian distribution of the number in the phase bins is approximated well when the expected number E is large. The lower limit for the expected number E is generally taken to be 5. At values lower than 5, the test statistic given by equation 4.1 is not distributed as χ^2 and therefore cannot be used to reject the null hypothesis with confidence.

The χ^2 test works well for phasegrams with narrow and high peaks, which are commonly seen in radio observations. However, for expected signals with broad and relatively small peaks, the χ^2 test is not as efficient and other tests (such as Z_n^2 (see section 4.2.2)) are used. The reason for χ^2's lack of sensitivity to broad peaks is obvious when it is recognised that it is "blind" to correlated excesses or defecits in neighboring bins. Another criticism of the method is that the phase origin and number of bins can be chosen arbitrarily.

4.2.2 Rayleigh and Z_n^2 Tests

The Rayleigh test (de Jager *et al.*, 1989b) probes for the fundamental sine and cosine harmonics and is therefore most efficient with sinusoidal pulse profiles, which are often observed in the case of X-ray pulsars. The test is independent of any event binning. For this test, each event phase ϕ_i is taken as a rotational phase between 0 and 2π. The test statistic is calculated by:

$$Z^2_{Rayleigh} = \frac{1}{N}\left(\left(\sum_{i=1}^{N} sin(\phi_i)\right)^2 + \left(\sum_{i=1}^{N} cos(\phi_i)\right)^2\right) \tag{4.3}$$

where N is the total number of events. With a large number of events and the absence of periodic modulation, the test statistic is approximately χ^2 distributed with 2 degrees of freedom.

The Z_n^2 test is a generalization of the Rayleigh test and was initially proposed by Buccheri & Sacco (1985). The test is independent of any event binning as it is calculated from the trigonometric moments α_j and βj of all events, where α_j and βj are

$$\alpha_j = \frac{1}{N}\sum_{i=1}^{N} cos\ (j\ \phi_i) \tag{4.4}$$

$$\beta_j = \frac{1}{N}\sum_{i=1}^{N} sin\ (j\ \phi_i) \tag{4.5}$$

where N is the number of events and ϕ_i is the phase of the event i. For a

candidate pulse period with n harmonics, the Z_n^2 test for uniformity is given by

$$Z_n^2 = \frac{2}{N} \sum_{j=1}^{n} \left(\left(\sum_{i=1}^{N} sin(j\ \phi_i) \right)^2 + \left(\sum_{i=1}^{N} cos(j\ \phi_i) \right)^2 \right) \tag{4.6}$$

The Rayleigh test can be recovered from equation 4.6 when $n = 1$. The distribution of Z_n^2 for a sample of random time events is χ^2 with $2n$ degrees of freedom.

There are several advantages to using the Z_n^2 test over the χ^2 test. For example, photon binning issues are eliminated. The Rayleigh test - in its simplest form (equation 4.3) - tests only for modulation at the fundamental frequency. It is totally "blind" to pure signals at higher harmonics. Higher harmonics can be tested by separately determining higher harmonics in equation 4.3 but the Z_n^2 test provides a way of accumulating the power at all harmonics up to the nth. However, studies (see de Jager *et al.* (1989a) and de Jager (1994)) have shown that the significance of a detection is a strong function of the number of harmonics chosen. Each fixed index n is powerful against a certain range of pulse profiles and relatively weak against the rest. Furthermore, for a specific candidate pulse profile, choosing a small value for n may 'wash out' any signal that may be present. On the other hand, choosing a large value for n results in the signal being swamped by the noise from the higher harmonics.

4.2.3 H-Test

To overcome the issues with having one free parameter n in the Z_n^2 test, de Jager *et al.* (1989a) proposed the H-Test. This test performs an automated search for

the optimum number of harmonics n, as can be seen from the test statistic

$$H = \max_{1 \leqslant m \leqslant 20} (Z_n^2 - 4n + 4) \tag{4.7}$$

where the maximum number of harmonics was chosen for practical reasons to be 20. Simulations of the sensitivity of H over a wide range of reasonable pulse profiles suggest the $4n + 4$ as an ad hoc reasonable moderator to Z_n (which of course increases monotonically as n increases). The distribution, in the absence of a signal, was found, by simulation, to be approximately exponential with a mean of 0.4. For a large number of events, the probability of obtaining a value larger than H is

$$P(\geq H) \sim e^{-0.4H} \tag{4.8}$$

Studies (de Jager *et al.*, 1989a) have shown the good sensitivity of the H-Test. However, for pulse profiles with sinusoid shapes expected a priori, the Rayleigh test is preferred. This is just a consequence of the general rule that the more a priori information that can be provided to a test, then the more sensitive the test can be. Pulse profiles with narrow or multiple peaks can, in some circumstances, be better detected by the Z_n^2 and χ^2 tests.

4.3 Time Series of Photons

One of the important issues with Fermi satellite data are source confusion caused by the relatively poor reconstruction of photon arrival directions. This is obvious to see from the second year catalogue, which contains a total of 1746 sources of

which 572 are unidentified or unassociated. At 100 MeV, the Fermi reconstruction of single photons at 68% confidence is within 3.5^o, which might contain several hundreds to thousands of X-ray and radio sources. For a typical Fermi source (with average $\approx$ 1000 photons), point-source reconstruction is accurate to within $\approx$ 6 arcminutes [A convenient, approximate rule of thumb is that point source location is given by the typical single photon reconstruction accuracy divided by the square root of the number of source photons detected]. This region can still contain several tens to hundreds of X-ray and radio sources, leading to source confusion.

Source location can be dramatically improved if source photons exhibit a short ($\ll$ 1 second) periodic arrival at Earth. Due to the Earth's orbit about the Solar System barycentre, an intrinsic periodicity in the arrival time of photons can be lost if the photon direction is not accurately assessed.

For example, a pulsar with a period of a few hundred milliseconds (say between 100ms and 600ms) would require photons timed correctly to within an order of 10ms (a 2D schematic of this scenario is shown in figure 4.1). Otherwise, any narrowly pulsed features in the folded light curve would be smoothed out. To overcome this issue, the pulsar source location technique developed by Ray *et al.* (2011) is used. The technique will be demostrated here and further developed to incorporate pulsars in binary systems. Unless otherwise specified, all results presented in this chapter are those of the thesis author.

The pulsar positon is taken to be at infinity so that parallax is not considered. Take two photons (from figure 4.1), both emitted from pulsar source within 1ms of each other (i.e. in phase). Each photon direction is reconstructed (exaggerated in figure 4.1 to make point) with errors of $\approx$ 1 degree. The times of arrival

(TOAs hereafter) for each photon will also be different (by several seconds in the example). However, if both photons are made to come from the true pulsar direction, then the difference between the TOA for each photon will be zero and the pulse profile can be seen. The error in the reconstructed photon direction is forced by timing to be within a few arcseconds. The approximate light travel time between two opposite positions of the Earth's orbital motion about the Solar System barycentre is ≈1000 seconds. Therefore, a fractional accuracy of 1:10^5 can be achieved, resulting in a positional accuracy of ≈ 2 arcsec. This is an impressive level of accuracy considering the point-source reconstruction from Fermi is accurate to within ≈ 6 arcminutes, given a source with average ≈ 1000 photons.

An actual example of this is shown in figure 4.2. Using the standard Fermi analysis and reconstruction techniques, all the observed X-ray sources in the large green ellipse would be potential candidates. The pulsar timing technique reduces the number of possible sources in this case to one.

Figures 4.3-4.5 show some of the analysis results for PSR J1836+5925. All the analyses use the same cuts for energy, RoI and time. The only difference between the figures is where the putative source location is centered. In figures 4.3 to 4.5 the upper left panel shows the photon number binned as a function of phase; the right panel shows the individual photon times (Y-axis) and phases (X-axis) and the lower left panel shows H-test TS as a function of event times. Figure 4.3 is centered 1.6° away from the true PSR J1836+5925 position and shows the phaseogram, pulse profile and H-test (described in section 4.2.3) TS results. Note the low number of events and the H-test TS compared to the other two figures. Figure 4.4 is centered 0.8° away from the true PSR J1836+5925 position. In comparison with figure 4.3, note the increased number of events and the improved H-test TS result. Figure

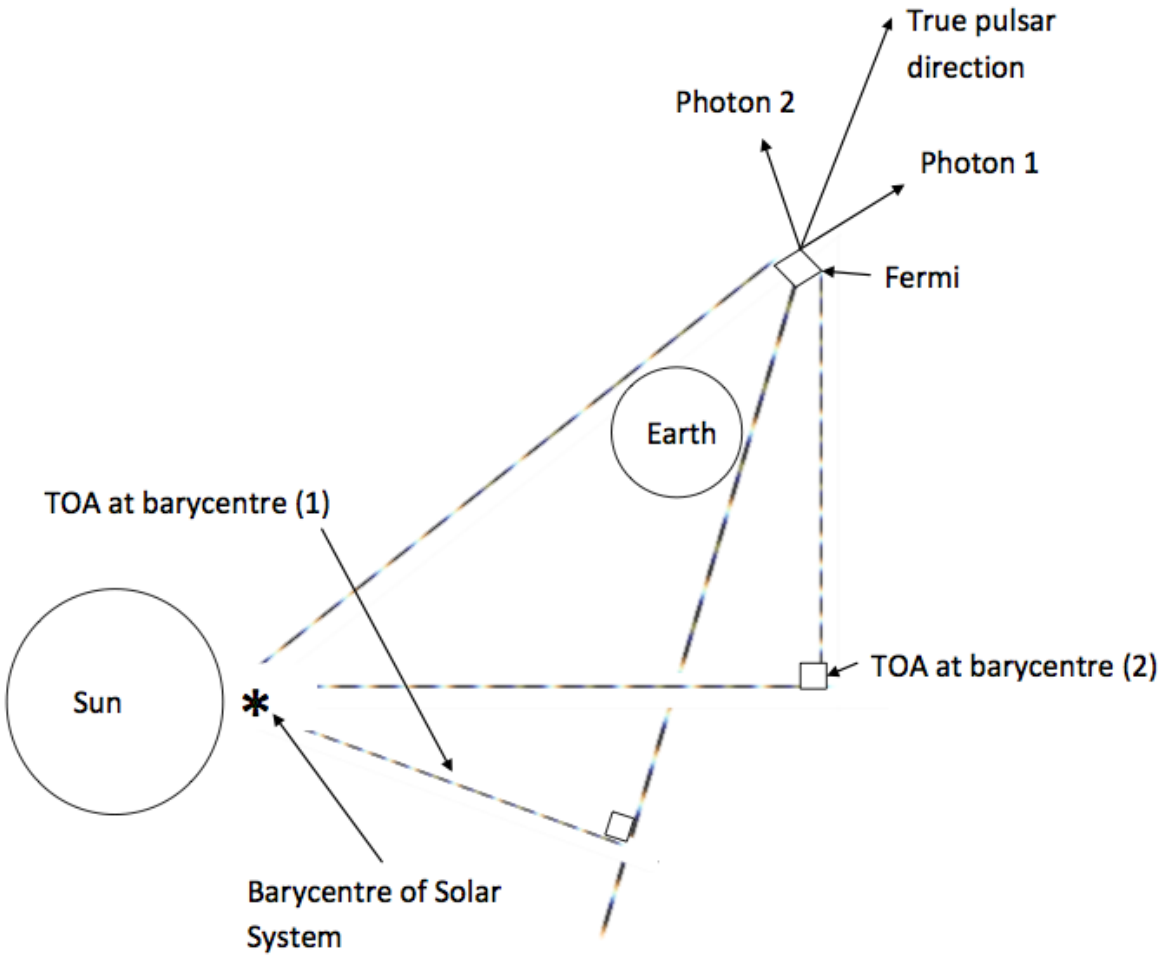

Figure 4.1: *2D schematic of a scenario where two photons from a pulsar are reconstructed by Fermi. The photons are emitted within 1ms of each other (i.e. in phase) but the TOA difference is of the order several seconds. However, if both photons are made to come from the true pulsar direction, then the difference between the TOA for each photon will be zero and the pulse profile can be seen. The error in the reconstructed photon direction is forced by timing to be within a few arcseconds.*

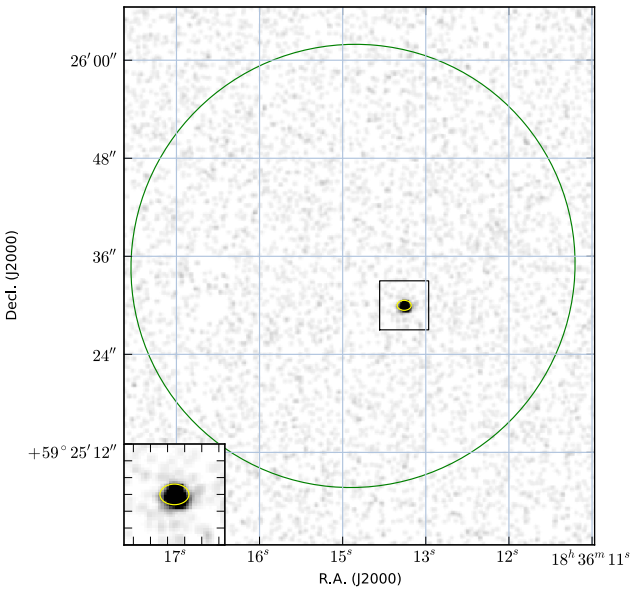

Figure 4.2: *X-ray image from Chandra of the region around PSR J1836+5925. The large green ellipse is the Fermi 95% reconstruction using standard techniques. The yellow ellipse is the result from the timing position technique and is shown in greater detail in the inset (3″ in width). Image from Ray* et al. *(2011).*

4.5 is centered on PSR J1836+5925 and shows as increased number of events and improved H-test TS. Compare this figure to 4.6, which is from Ray *et al.* (2011). Both contain the same cuts except figure 4.5 uses a longer time cut and hence a greater number of events observed.

When the source is incorrectly attributed to be 1.6^o away from the true source location (figure 4.3) the pulsar - via timing - is not detected. The H-test TS, maximising at only ≈ 5 is not statistically significant (P ($>$ H $= 5$) $\approx 13.5\%$ by chance).

When the source is better located, but 0.8^o away (figure 4.4), the pulsar begins to be detectable - the binned phaseogram (upper left) shows the characteristic narrow main pulse, and the source could be claimed detectable (at chance prob-

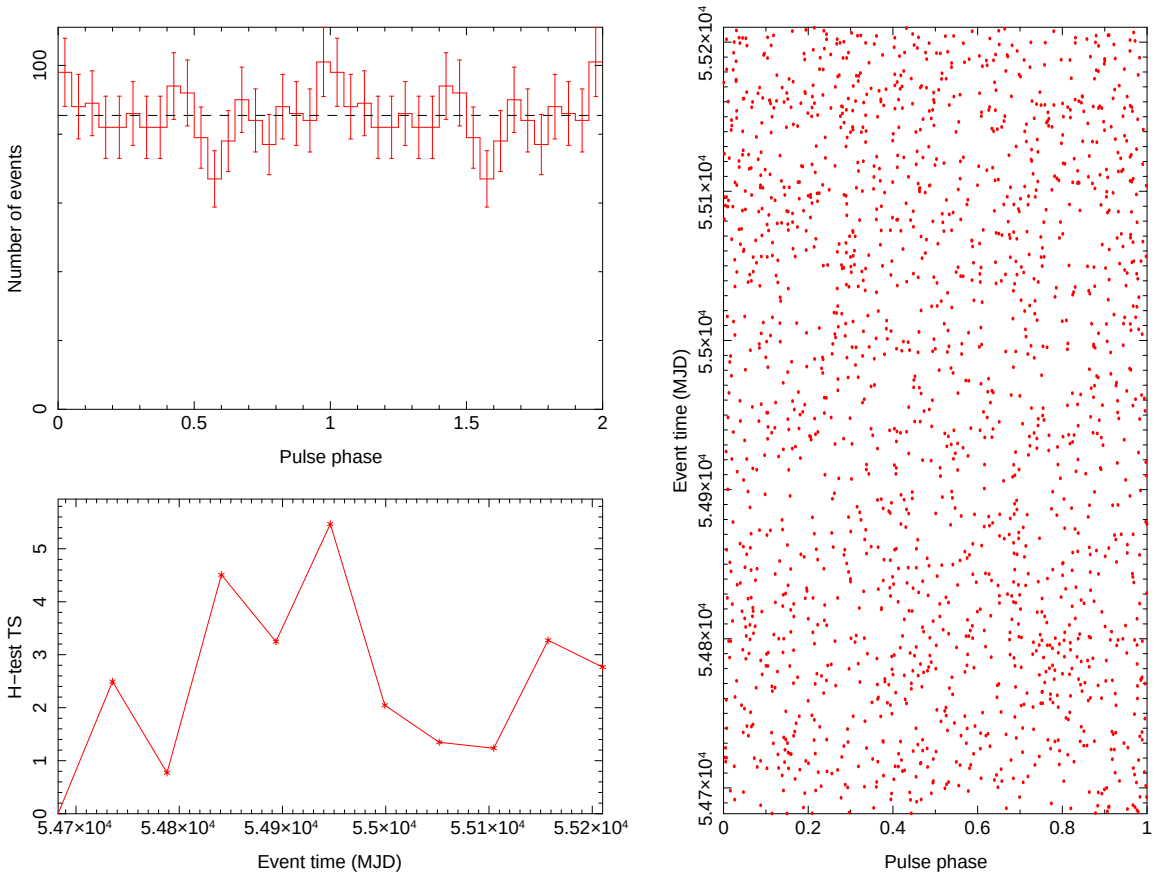

Figure 4.3: *2-D phaseogram, pulse profile and H-test TS of PSR J1836+5925. Two rotations in phase are shown on the X-axis. The centre for this analysis is 1.6° away from PSR J1836+5925. Note the low number of events and H-test TS in comparison with figure 4.5.*

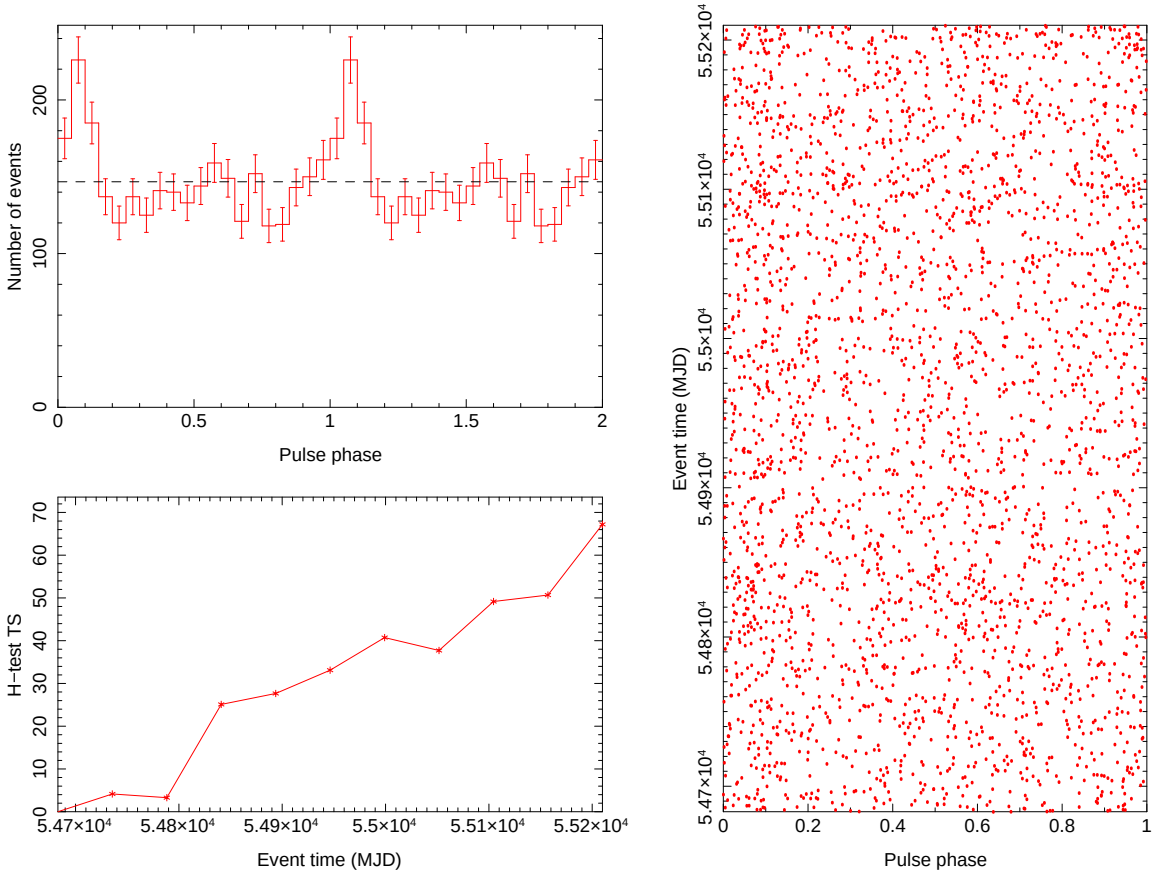

Figure 4.4: *2-D phaseogram, pulse profile and H-test TS of PSR J1836+5925. Two rotations in phase are shown on the X-axis. The centre for this analysis is 0.8° away from PSR J1836+5925. Note the increased number of events and H-test TS in comparison with figure 4.3.*

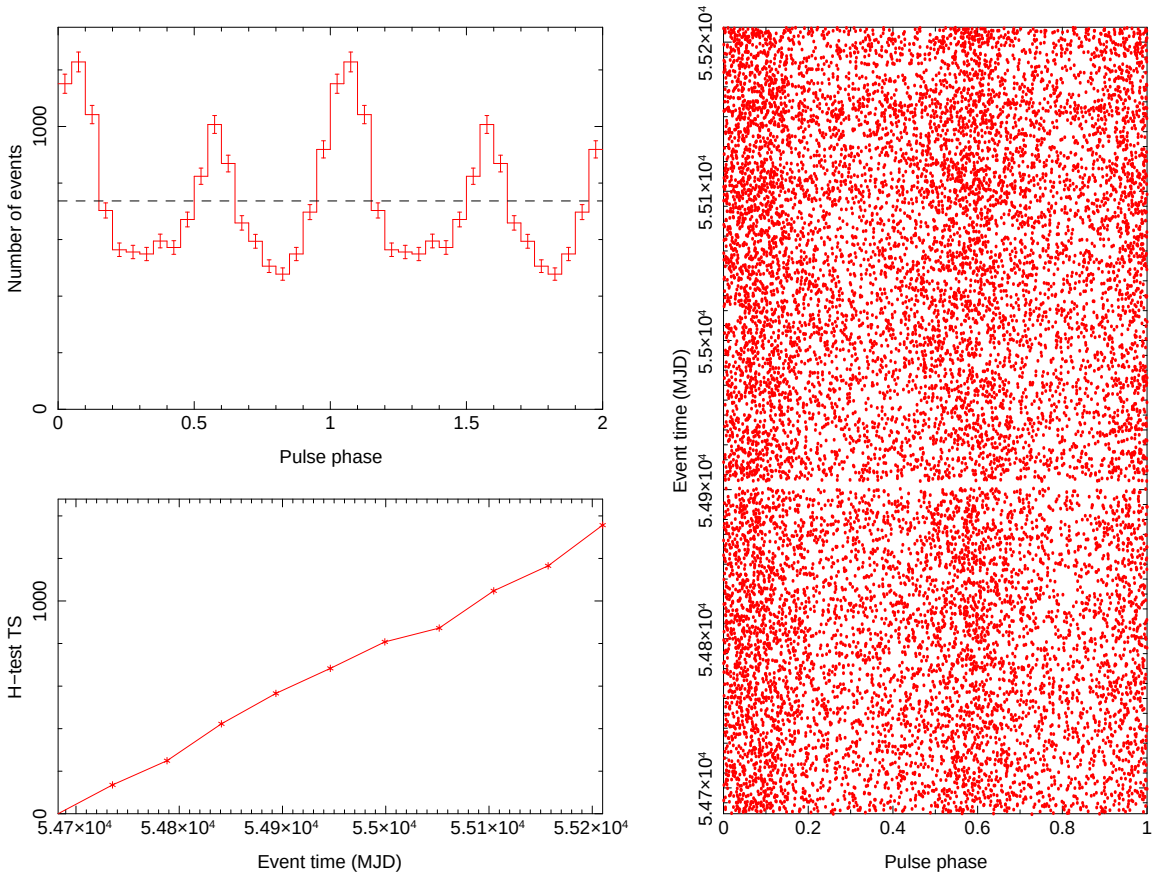

Figure 4.5: *2-D phaseogram, pulse profile and H-test TS of PSR J1836+5925. Two rotations in phase are shown on the X-axis. This analysis is centered on PSR J1836+5925. Note the increased number of events and H-test TS in comparison with figures 4.3 and 4.4.*

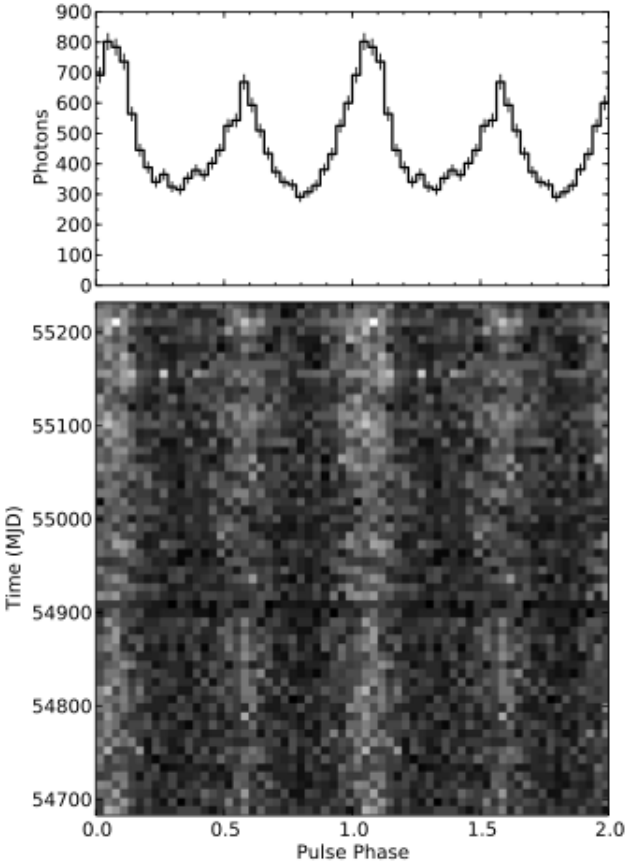

Figure 4.6: *2-D phaseogram and pulse profile for PSR J1836+5925. Compare these results with those in figure 4.5 which use the same energy and RoI cuts with longer observation time.*

ability level, say, of 10^{-4} when H $\approx$ 20), which is reached (lower left panel) after an accumulation of $\approx$ 140 days.

When accurately located, enhanced detectability is very evident: the folded light curve (figure 4.5 upper left) shows the full double peaked light curve; the H-test succeeds at detection after only 20 days (lower left) and shows the statistically stable linear increase of H with exposure time, and the pulse structure is even evident in the single photon time/phase plot (figure 4.5 right).

For the case of solitary pulsars, timing involves making precise measurements

of pulse TOA at an observatory and then fitting the parameters of a model to those measurements. However, for Fermi, the only option for pulsar timing is to time them directly using gamma-ray data. The accuracy of a pulse time of arrival measurement for Fermi is determined mainly by photon statistics and is accurate to the order of a millisecond (i.e. each photon is tagged to less than 1ms).

To determine a TOA in a given data set, a pulse phase is assigned to each photon based on an initial model. The phase offset (Δ) required to align a standard template profile with the measured pulse profile (see figure 4.7) is then measured. The standard template profile used is selected from the best fitting of several models. For example, in many cases, the statistics are limited such that the pulse profile can be described as the sum of a constant background and a small number of Gaussian peaks.

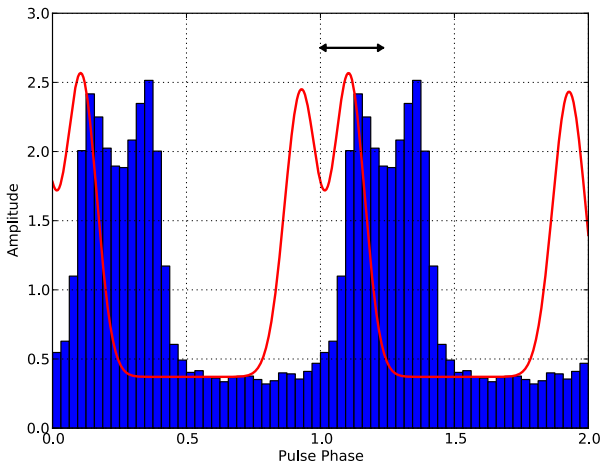

Figure 4.7: *An example of measuring TOA. The blue histogram is a pulse profile from observed photons. The red curve is a template profile and the black arrow represents the measured phase offset required to align the observed histogram with the template profile. Image from Ray* et al. *(2011).*

The TOA from each data set can then be fit to the chosen template with the

pulse profile defined by the template. An approximate timing solution is used to fold the photon arrival times and obtain a set of phases, which are then compared with the template light curve. The probability of observing the phases from the data and the model light curves is used to form a log likelihood that can then be maximised and therefore determine precise pulse timing and position of the pulsar.

For the catalogue of binary pulsars analysed in section 6, the above analysis is only used if the standard Fermi analysis chain (see section 2.5) results in TS above a threshold of 25 that can't be associated with a known gamma-ray source. For each source, the full time range is split into 20 bins. Any bins with TS $\geq$ 16 are then split into 4 bins, with each bin containing approximately 30 days of data. Any remaining bins with TS $\geq$ 16 are then analysed with the above technique.

Pulsar PSR J1836+5925, which was first observed with Fermi by Ray *et al.* (2011), will be used to demonstrate this technique. The data are initially analysed using the standard Fermi analysis chain, which identifies the best cuts for time to maximise signal to noise ratio. For the catalogue sources in section 6 (and PSR J1836+5925 in this example), the energy and RoI cuts are fixed for consistency (energy cuts of 200 MeV - 300 GeV, and RoI of 10 deg). For unidentified candidates, there is typically no publicly available ephemeris to use for phase folded analysis. To overcome this issue, known pulsar ephemeris within 1.5 deg of the candidate sources are used to either confirm or eliminate them as being the source of the possible emission. For PSR J1836+5925, there is a publicly available ephemeris from Ray *et al.* (2011) and the result of the phase folded analysis is shown in figure 4.5. For the case of the wrong ephemeris being used (i.e not from the candidate source), the resulting plot is shown in figure 4.8. The low TS of 1.2 (which is a chance probability level of 62 %) effectively rules out the wrong ephemeris as a

possible candidate.

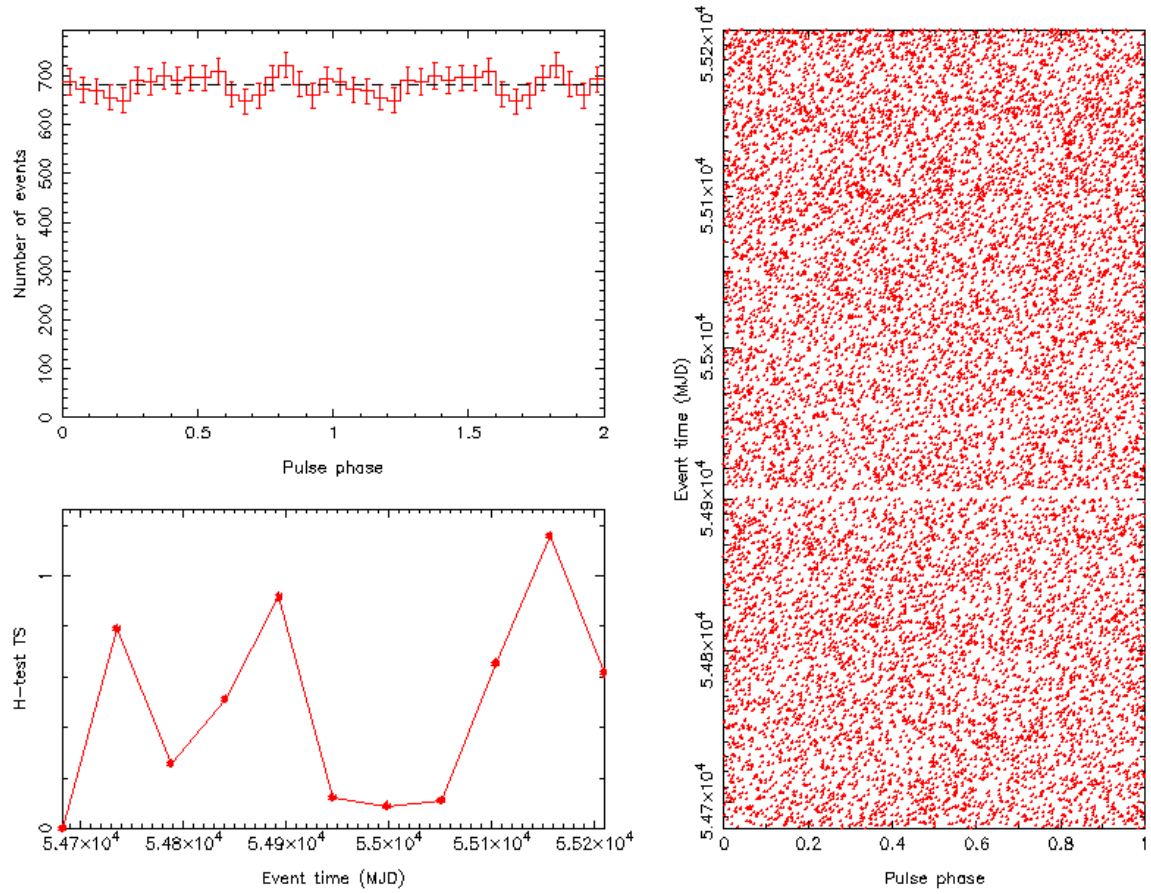

Figure 4.8: *2-D phaseogram, pulse profile and H-test TS of PSR J1836+5925. Two rotations in phase are shown on the X-axis. The data are fitted with an ephemeris from a different source to demonstrate the effect of using the wrong ephemeris on a candidate source. The chance probability level for this ephemeris is 62 %.*

Any sources with H-test TS of ≥ 20 (which is chance probability level of 10^{-4}) are potential candidates that are analysed further. The phase folded light curves are fitted with three template profiles: Gaussian, Kernel Density (KD) and Empirical Fourier (EF) (see Ray *et al.* (2011) for information on these profiles). The resulting fits for PSR J1836+5925 are shown in figures 4.9 - 4.11. The timing

models can then be further refined and used to produce an updated ephemeris for the source.

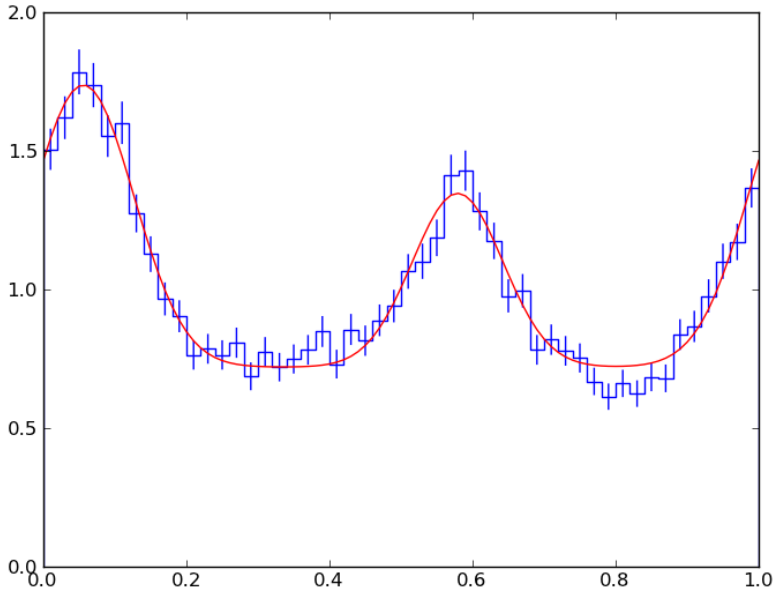

Figure 4.9: *Pulse profile of PSR J1836+5925 fitted with a Gaussian template. The blue histogram shows the measured pulse profile with 32 bins, but the Gaussian template is fitted to the unbinned photon phases.*

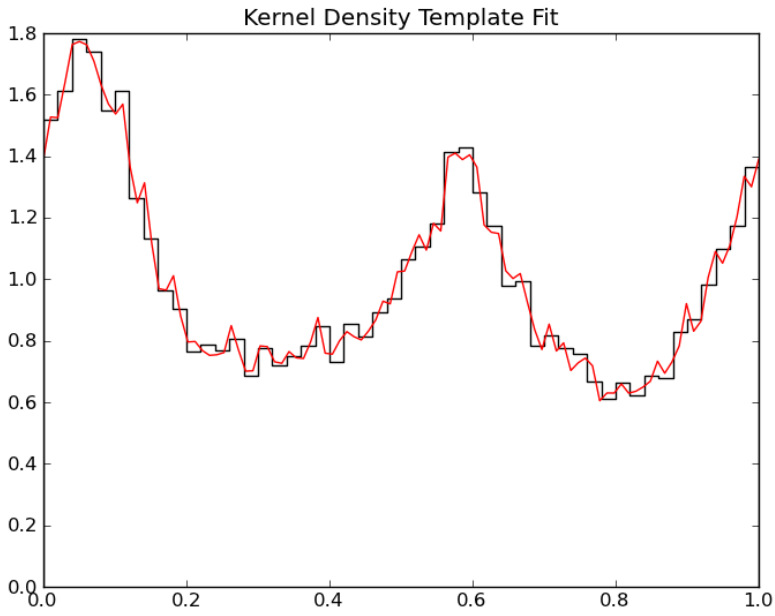

Figure 4.10: *Pulse profile of PSR J1836+5925 with the unbinned photon phases being fitted by a Kernel Density template. The black histogram shows the measured pulse profile with 32 bins.*

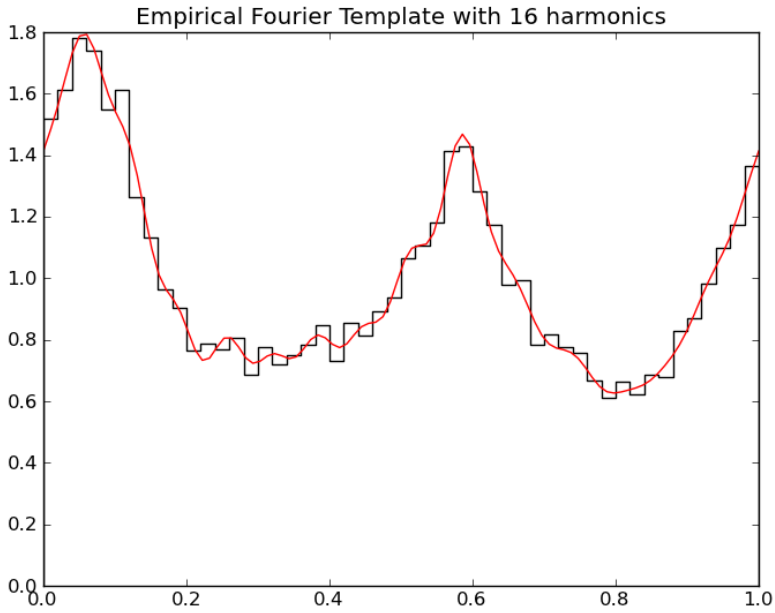

Figure 4.11: *Pulse profile of PSR J1836+5925 fitted with a Empirical Fourier template with 16 harmonics. The black histogram shows the measured pulse profile with 32 bins, but the Empirical Fourier template is fitted to the unbinned photon phases.*

For some sources, complimentary data from other wavelengths are available and cross correlation techniques can be used to identify the sources.

4.4 Cross Correlation

The cross correlation function is used in many fields such as pattern recognition and waveform analysis. In it's simplest form, the cross correlation measures the similarity of two patterns. In astrophysics, it is most commonly used to search for known features within long duration signals. The input for the cross correlation is therefore two time series, one with features of interest and the other with unknown features.

Given two continuous time series, x_i and y_i, with mean values $\bar{x}$ and $\bar{y}$, and variances s_x and s_y respectively, the cross correlation function of each bin is estimated by

$$\tau_{dcf}(\tau) = \frac{1}{n} \sum_{\tau_{ij} \epsilon bin} \frac{(x_i - \bar{x})(y_i - \bar{y})}{s_x s_y} = \frac{1}{n} \sum_{\tau_{ij} \epsilon bin} u_{ij} \tag{4.9}$$

and the error on the estimate by the scatter of the u_{ij} terms. The autocorrelation function is the cross correlation of a signal with itself.

To demonstrate equation 4.9, consider a function x_i (figure 4.12(a)) which has features of interest in the test signal y_i (figure 4.12(b)). The cross correlation equation 4.9 is effectively the sliding of the test signal y_i along the time axis and calculating the integral (or for discrete functions, the sum) of the product of x_i and y_i at each step of the slide. The cross correlation value (x_i * y_i) maximizes when the two functions are aligned. Inverting the sign of either function will result in a minimum (anti-correlation) appearing at the position of the correlation.

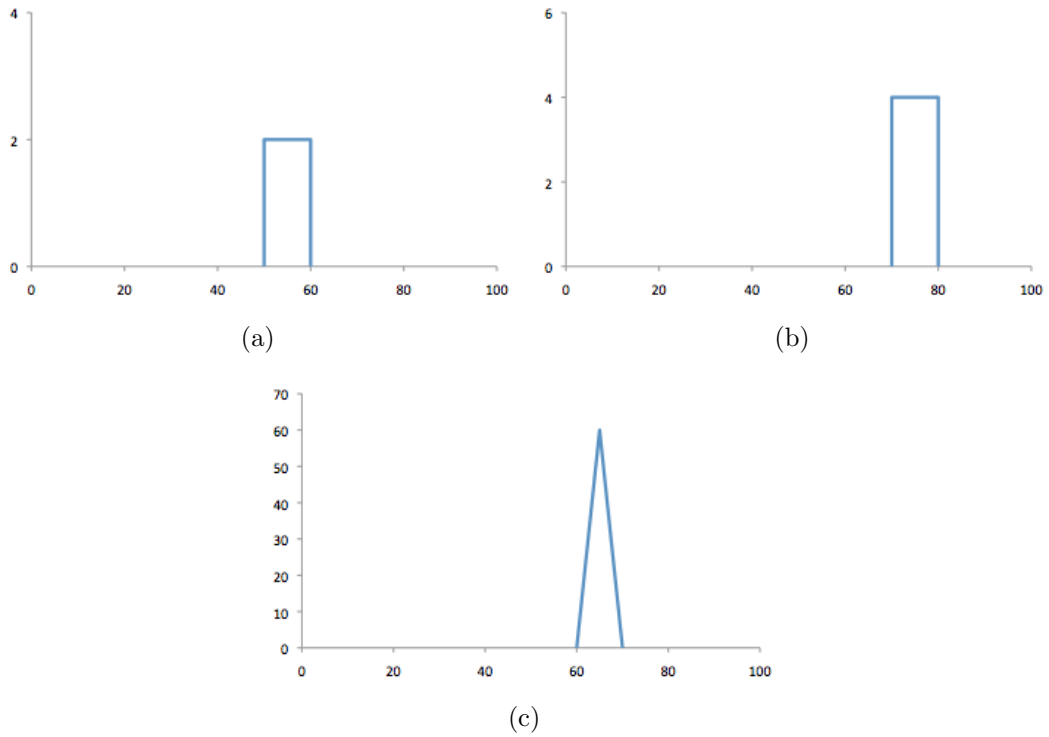

Figure 4.12: *Simple diagram to demonstrate the principal of the cross correlation function. (a) Function with features of interest and amplitude of 2. (b) Test signal with an amplitude of 4. (c) The resulting cross correlation.*

Since the sampling of the light curves is often uneven (due to data gaps in one or both series, for example), equation 4.9 cannot be used directly and the technique has to be adapted. Two commonly used adaptations are the interpolated cross correlation function (Gaskell & Peterson, 1987) and the discrete correlation function (DCF) (Edelson & Krolik, 1988). For the DCF, all pairs of points from the two continuous time series are ordered according to their time difference, τ_{ij}, and binned by the user where the cross correlation function of each bin is given by equation 4.9. A modified version of DCF, the z-transformed discrete correlation function (ZDCF) (see Alexander (1997) for details), is used to analyse the Cir X-1 data (see section 5.1). ZDCF has the advantage of being more efficient in

uncovering correlations and deals with under-sampled light curves better than the DCF.

4.5 Pulsar Gating

For some sources, the periodic modulation in the data are swamped by the contributions of a bright pulsar in the region of interest. For these sources, a pulsar gating technique must be applied first in order to minimise the pulsar contributions.

Pulsar gating is the technique of removing the contributions of a bright pulsar to a region of interest so that analysis of fainter sources is possible. To demonstrate this technique, the Vela pulsar is used in this section.

The technique requires prior knowledge of the pulsar ephemeris and so is not suitable for blind searches. The pulsar ephemeris is used to assign pulse phases to the pulsar as shown in figure 4.13 for the Vela pulsar. The figure clearly shows the bridge emission between the two peaks and the off-pulse interval in the phase-space after the second peak at phase > 0.6.

Once the phases are assigned, the unwanted phase periods can be filtered out. This effectively removes the pulsar from the data, which can then be analysed for fainter sources. Figure 4.14 shows two plots for the Vela pulsar. The data sets for both plots are exactly the same and the only difference is the removal of the two peaks and bridge emission shown in figure 4.13.

This technique is important for regions containing multiple bright sources, such as the Cygnus or Carina regions, and could significantly improve the detection of faint sources or those with binary periods. The technique is used in section 5.2

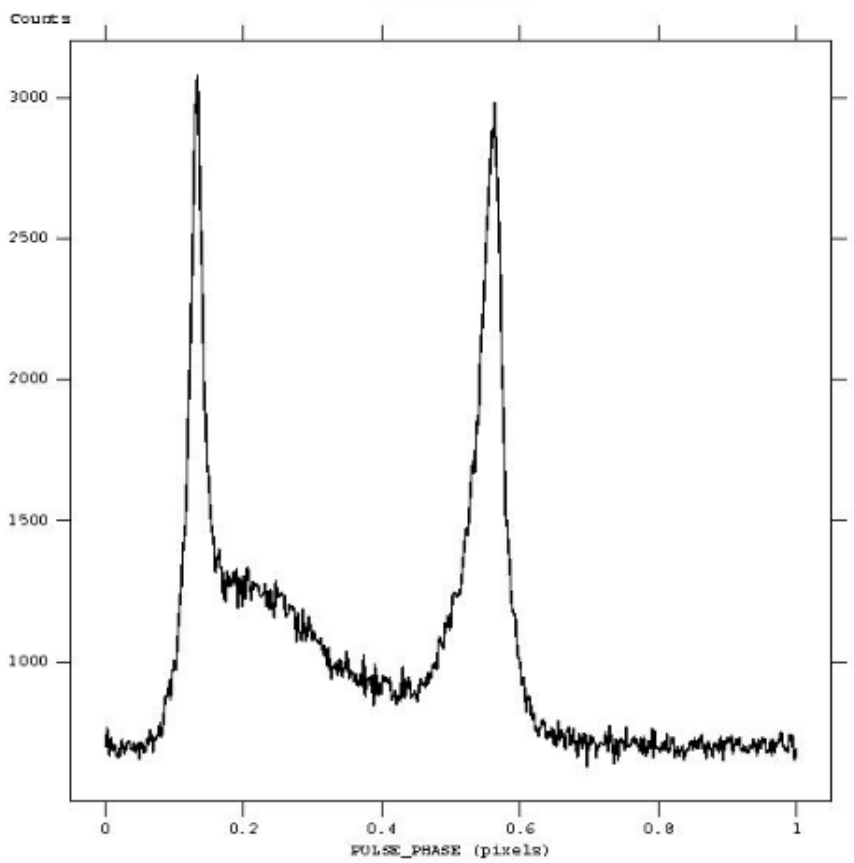

Figure 4.13: *Phase folded light curve for the Vela Pulsar. The bridge emission between the two peaks and off-pulse interval in the phase-space after the second peak at phase > 0.6 can clearly be seen.*

to detect Cygnus X-3. However, each removal of a pulsar costs a large fraction of telescope livetime and must be used cautiously.

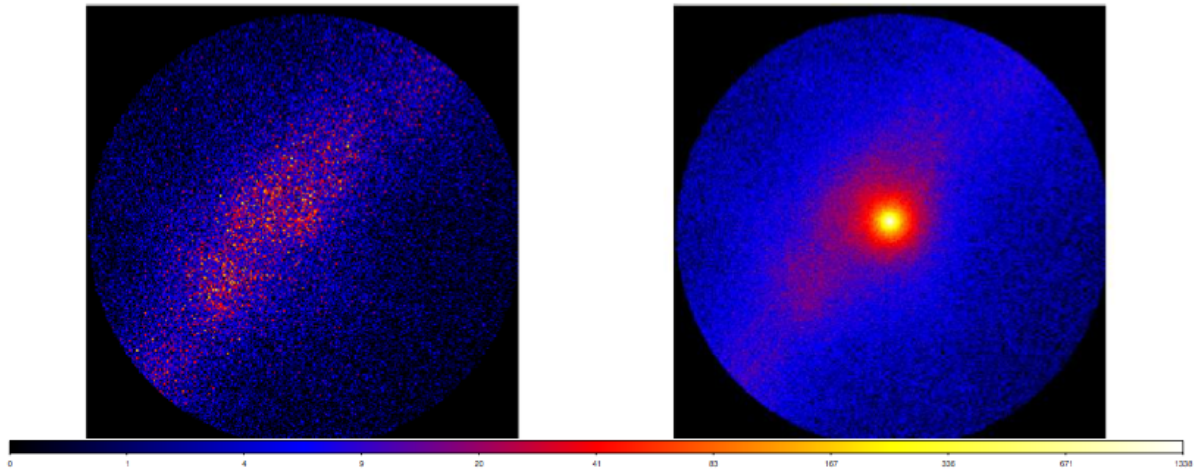

Figure 4.14: *Counts map of the Vela pulsar region. Both plots are centred on the Vela pulsar and have a radius of 15 degrees. The plot on the right is the full data set. The plot on the left shows the effect of removing the two peaks and bridge emission from figure 4.13 as discussed in the text. The scale at the bottom represents the number of counts per pixel.*

4.6 Likelihood Analysis

In many fields of science, from physics to psychology, the purpose is to uncover general laws and principles that govern the behaviour under investigation. As these laws are not directly observable, they are conceived as hypotheses. In statistical mathematics, these hypotheses are formulated in terms of parametric families of probability distributions called models. The aim of modeling is to deduce the underlaying principles via the testing of the viability of each model.

Each model with specific parameters can be evaluated for goodness of fit: how well the parameters fit the observed data. This procedure is referred to as *parameter estimation*. There are two common methods of parameter estima-

tion: least-squares and maximum likelihood estimation. Least-squares estimation is tied to many statistical concepts such as sum of squares error, linear regression and root mean squared deviation. It is often used in areas such as psychology as Least-squares estimation requires minimal disribution knowledge and is useful for obtaining a descriptive measure of the observed data.

The other method, and the one used in this thesis, is the maximum likelihood estimation. It is widely used in statistics and is a prerequisite for the χ^2 test, Bayesian methods and inference with missing data. This section will discuss the maximum likelihood estimation technique and its use in this thesis.

4.6.1 Model Specification

4.6.1.1 Probability Density Function

Consider a data vector $y = (y_1, ..., y_m)$ as a random sample of an unknown population. The aim of statistical data analysis is to identify the population that is most likely to have generated the data sample. Each population is identified by a corresponding probability distribution. Each probability distribution is associated with a unique value of the model's parameter. Different probability distributions are generated as the model's parameters change in value. The model is defined by the collection of probability distributions indexed by the model's parameters.

The probability density function can be defined as $f(y|w)$, which specifies the probability of observing data vector y given the model parameter w. The parameter $w = (w_1, ..., w_k)$ is a vector defined on a multi-dimensional space. Consider the individual observations, y_i, as statistically independent of one another. The probability density function for the data, $y = (y_1, ..., y_m)$, given the parameter

vector w can then be defined as the multiplication of probability density functions for individual observations:

$$f(y = (y_1, y_2, ..., y_n)|w) = f_1(y_1|w)f_2(y_2|w)...f_n(y_m|w) \tag{4.10}$$

To demonstrate the probability density function, consider a simple case with one observation and one parameter (i.e. $m = k = 1$). The data (y) represents the number of successes in a sequence of 10 trials. The probability of success on any one trial (represented by w) is 0.2. The probability density function is given by:

$$f(y|n = 10, w = 0.2) = \frac{10!}{y!(10-y)!}(0.2)^y(0.8)^{10-y}(y = 0, 1, ..., 10) \tag{4.11}$$

which is the binomial distribution with parameters $n = 10$ and $w = 0.2$. Changing the parameter value (for example, $w = 0.7$) produces a new probability density function:

$$f(y|n = 10, w = 0.7) = \frac{10!}{y!(10-y)!}(0.7)^y(0.3)^{10-y}(y = 0, 1, ..., 10) \tag{4.12}$$

The number of trials (n) is also considered as a parameter. The shapes of the probability density functions represented in Equations 4.11 and 4.12 are shown in Figure 4.15.

The probability density function of the binomial distribution for arbitary values

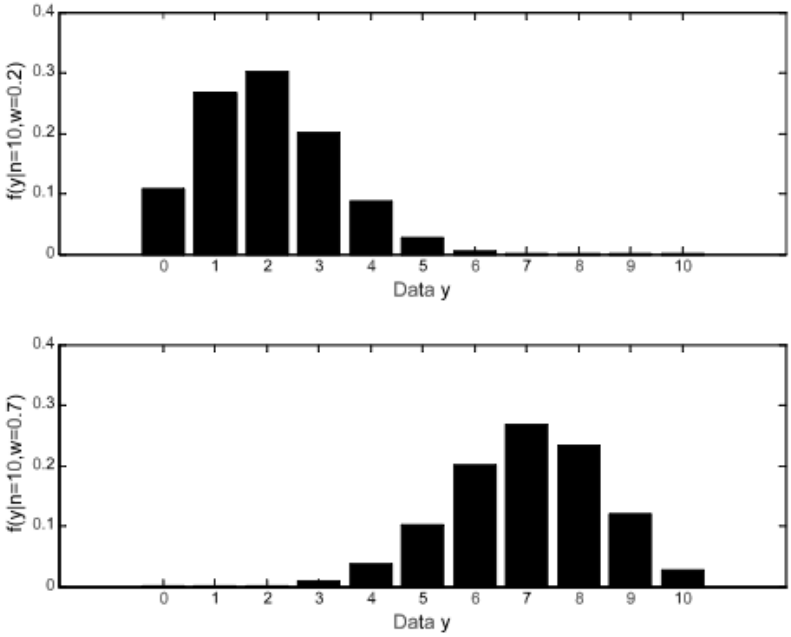

Figure 4.15: *Binomial probability distributions for probability parameters* $w = 0.2$ *(top panel) and* $w = 0.7$ *(bottom panel). The sample sizes in both cases are taken to be* $n = 10$. *Figure from Myung (2003)*

of w and n has the general expression:

$$f(y|n,w) = \frac{n!}{y!(n-y)!}(w)^y(1-w)^{n-y}(0 \leqslant w \leqslant 1; y = 0, 1, ..., n) \tag{4.13}$$

For given values of n and w, the function in Equation 4.13 specifies the probability of data y. The model can then be defined as the collection of all probability density functions created by varying the parameters across their range (for the above example, 0 - 1 for w).

4.6.1.2 Likelihood Function

Using a set of parameter values, the resulting probability density function will demonstrate that some data are more likely than other data. From the previous example in Section 4.6.1.1, the probability distribution function with $y = 2$ is more probable to occur than $y = 5$ (0.302 and 0.026, respectively). However, in most cases, the data has already been observed and the interesting question is to find the one probability density function that is most likely to have produced the data. The solution is to define the likelihood function as the reverse of the roles of the data y and parameter w in $f(y|w)$:

$$L(w|y) = f(y|w) \tag{4.14}$$

where $L(w|y)$ is the likelihood of the parameter w given the observed data y. The likelihood function for $y = 7$ and $n = 10$ from the one parameter binomial example in Equation 4.13 is:

$$\begin{aligned} L(w|n = 10, y = 7) &= f(y = 7|n = 10, w) \\ &= \frac{10!}{7!3!} w^7 (1 - w)^3 \quad (0 \leqslant w \leqslant 1) \end{aligned} \tag{4.15}$$

with the resulting shape of the likelihood function shown in Figure 4.16. Note that there is an important difference between Figures 4.15 and 4.16. The probability density function ($f(y|w)$) and the likelihood function ($L(w|y)$) are defined on different axes in Figures 4.15 and 4.16, respectively. The probability density function in Figure 4.15 is a function of the data given a particular set of parame-

ter values (defined on the data scale). The likelihood function in Figure 4.16 is a function of the parameter given a particular set of observed data (defined on the parameter scale). Therefore, the probability density function and the likelihood function are not directly comparable. The probability density function (shown in Figure 4.15) is the probability of a particular data value given a set of fixed parameters, whereas the likelihood function (shown in Figure 4.16) is the probability of a particular parameter value given a set of fixed data.

Note that the assumption in the likelihood function shown in Figure 4.16 is that there is only one parameter beside n, which is assumed to be known (this is why the likelihood is a curve).

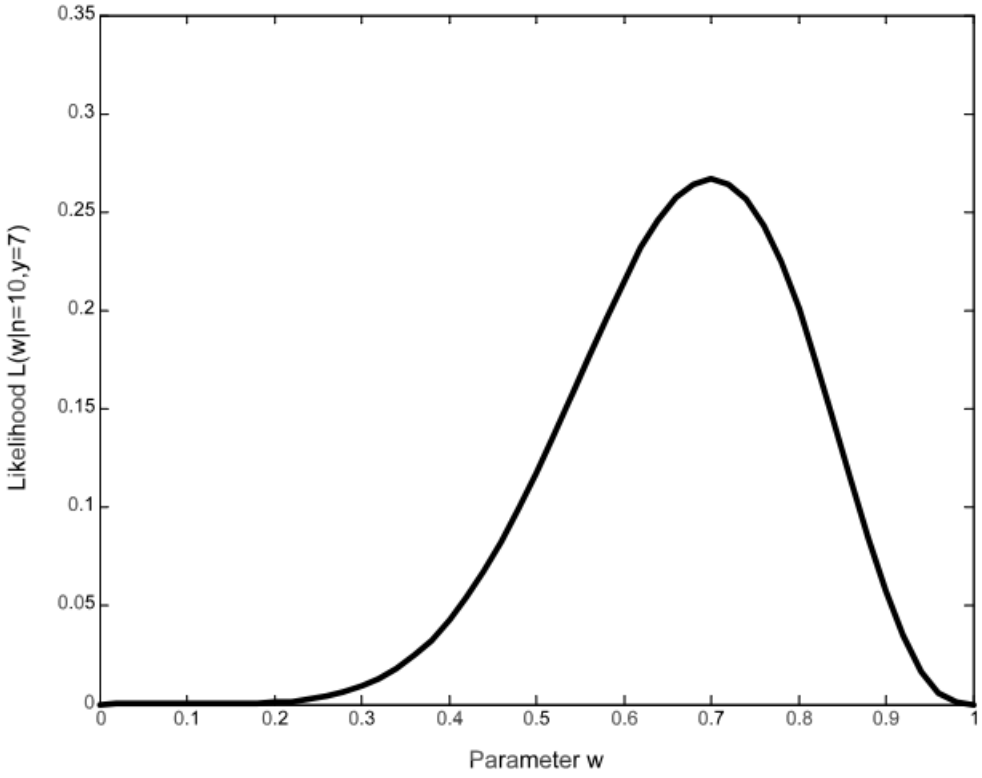

Figure 4.16: *The likelihood function from sample size* $n = 10$ *and observed data* $y = 7$. *Figure from Myung (2003)*

4.6.2 Maximum Likelihood

Once the likelihood function of a model given the data are determined, statistical inferences can be achieved on the probability distribution that underlines the data. The aim is to find the parameter value that corresponds to the desired probability distribution, given that different parameter values index different probability distributions (see Figure 4.15).

Maximum likelihood estimation, originally developed by Fisher (1920), aims to find the value of the parameter vector that maximizes the likelihood function $L(w|y)$ (i.e. the desired probability distribution is the one that makes the observed data "most likely"). The resulting parameter vector is the maximum likelihood estimate (denoted by w_{MLE}). For example, the maximum likelihood estimate in Figure 4.16 is $w_{MLE} = 0.7$ with maximized likelihood value of $L(w_{MLE} = 0.7|n = 10, y = 7) = 0.267$ and the corresponding probability distribution shown in the bottom panel of Figure 4.15. Therefore, according to the maximum likelihood principle, this population is the most likely to have produced the observed data of $y = 7$.

4.6.2.1 Likelihood Equation

It is computationally convenient to obtain the maximum likelihood estimate by maximizing the log-likelihood function, $\ln L(w|y)$. The two functions, $L(w|y)$ and $\ln L(w|y)$, are monotonically related to each other so that maximizing either will produce the same maximum likelihood estimate. The maximum likelihood estimate, w_{MLE}, must satisfy the following partial differential equation (known as the

likelihood equation):

$$\frac{\delta \ln L(w|y)}{\delta w_i} = 0 \tag{4.16}$$

where $w_i = w_{i,MLE}$ for all $i = 1, ..., k$, since the maximum or minimum of a continuous differential function has first derivatives that disappear at these points. The log-likelihood function, $\ln L(w|y)$, must also be a maximum (peak) and not a minimum (valley) as the first derivative would not show this. However, this can be checked by calculating the second derivatives of the log-likelihood function

$$\frac{\delta^2 \ln L(w|y)}{\delta w_i^2} < 0 \tag{4.17}$$

and show whether they are negative at $w_i = w_{i,MLE}$ for all $i = 1, ..., k$.

To demonstrate the maximum likelihood estimate process, consider the previous one parameter binomial example with a fixed value of n. The likelihood function $L(w|n = 10, y = 7)$ can be substituted into Equation 4.15 to obtain the log-likelihood:

$$\ln L(w|n = 10, y = 7) = \ln \frac{10!}{7!3!} + 7 \ln w + 3 \ln(1 - w) \tag{4.18}$$

And the first derivative of the log-likelihood is:

$$\frac{\delta \ln L(w|n = 10, y = 7)}{\delta w} = \frac{7 - 10w}{w(1 - w)} \tag{4.19}$$

The maximum likelihood estimate can be obtained by requesting that the above equation equal to zero. The resulting estimate would be $w_{MLE} = 0.7$. The second derivative of the log-likelihood is then calculated to ensure the result is a maximum

and not a minimum:

$$\frac{\delta^2 \ln L(w|n=10, y=7)}{\delta w^2} = -\frac{7}{w^2} - \frac{3}{(1-w)^2} \quad (4.20)$$

$$= -47.62 \quad (4.21)$$

The above result is negative, which shows that the output is a maximum as desired.

However, it is typically not possible to obtain an analytic result for the maximum likelihood estimate. This occurs in particular when the model involves several parameters and the probability density function is non-linear. The solution is to obtain the maximum likelihood estimate numerically using non-linear optimization, which attempts to find the optimal parameters that maximize the log-likelihood. Rather than search exhaustively in the whole parameter space, non-linear optimization searches in smaller sub-sets via iterative steps. Each iteration obtains a new set of parameter values by adding small changes from the previous parameters. The new parameters are more likely to lead to improved performance compared to the previous iteration. The iterative process is judged to have succeeded when it converges on an optimal set of parameters.

4.6.3 Likelihood Ratio Test

The likelihood ratio test, first introduced by Neyman & Pearson (1933), is used for hypothesis testing. The likelihood ratio is the likelihood of the null hypthesis for the data divided by the likelihood of the model for the same data. The likelihood ratio test became more useful with the introduction of Wilks's theorem, which

established an analytical expression of the likelihood ratio in the null hypothesis (i.e. the null hypothesis is true). Wilks's theorem demonstrated that twice the natural logarithm of the likelihood ratio is distributed as χ^2 in the null hypothesis with $h - m$ degrees of freedom, except for terms of order $(N)^{-\frac{1}{2}}$. Here, $h - m$ is the number of additional parameters that are optimized for the model hypothesis and N is the number of samples.

The application of the likelihood ratio test to photon-counting experiments was first described by Cash (1979) and later applied to COS-B gamma-ray data by Pollock *et al.* (1981). Maximum likelihood was also used to analyse data from COMPTEL, the Compton telescope on the Compton Observatory (Schoenfelder *et al.*, 1993).

4.6.4 Likelihood Uncertainty

For Fermi analysis, the likelihood ratio is given by:

$$TS = -2\log_e\left(\frac{L_o}{L_s}\right) \tag{4.22}$$

where L_o and L_s are the null and model likelihood, respectively. For each paramter, Wilk's theorem dictates that the χ^2 distribution holds. Therefore, a decrease in ln L of 0.5 from its maximum value corresponds to the 68% (1 σ) confidence region for that parameter.

As an example, in preparotory work done for this thesis on the Hydra A galaxy cluster (Ali & the HESS collaboration, 2012), the spectral index was fixed and the flux was allowed vary. The resulting log likelihood with varying flux is shown in figure 4.17. Note that this is the minus log likelihood and so the likelihood is

minimised instead of maximised. The minimum value in figure 4.17 occurs at a flux of 1.0 x 10^{-10} photons cm^{-2} s^{-1}. The confidence region for that flux at the 68% (1 σ) level is given by increasing the minus log likelihood by 0.5.

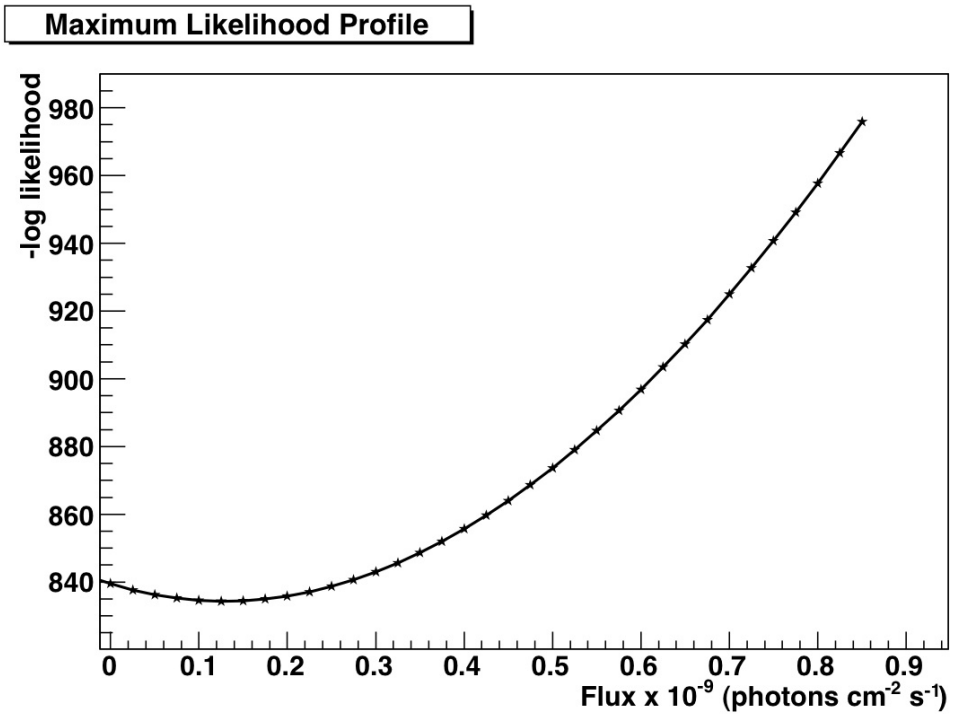

Figure 4.17: *The maximum likelihood profile showing the minimisation of the minus log likelihood with respect to flux.*

The Fermi analysis tools use several different minimisations. The Minuit minimisation tool was used for all analysis in this thesis.

4.6.5 Source Model Characterisation

A source is characterised by its photon flux density, which is the rate of photons incident per unit time/energy/area from a solid angle $d\Omega$ about the position $\vec{\Omega}$. The photon flux density is defined as $F(t, E, \vec{\Omega})$, where the observable properties

of the source are denoted by time of arrival (t), energy (E) and direction of origin ($\vec{\Omega}$).

The emission mechanisms (see section 1.3 for details) that power gamma-ray sources typically produce spectra spanning multiple decades of energy with a modest curvature (i.e. broadband spectra). These spectra are often modeled with a simple power law:

$$F(t, E, \vec{\Omega}; N_0, \gamma, E_0) = N_0(t, \vec{\Omega}) \left(\frac{E}{E_0}\right)^{-\gamma(t,\vec{\Omega})} f(\vec{\Omega}) \tag{4.23}$$

where N_0 is the prefactor, γ is the index and E_0 is the scale[1]. The normalized function $f(\vec{\Omega})$ describes the spatial morphology of the source. However, this thesis will only focus on sources that cannot be spatially resolved (i.e. point sources). The emission from most pulsars can be adequately characterised (Abdo *et al.*, 2009b) by an extension of Equation 4.23 with exponential suppression of the flux above a cutoff energy:

$$F(t, E, \vec{\Omega}; N_0, \gamma, E_0, E_c) = N_0(t, \vec{\Omega}) \left(\frac{E}{E_0}\right)^{-\gamma(t,\vec{\Omega})} exp\left(-\frac{E}{E_c(t, \vec{\Omega})}\right) f(\vec{\Omega}) \tag{4.24}$$

For the remainder of this chapter, the particular form of the spectral model will not be specified and instead will be replaced with a set of parameters denoted by $\vec{\lambda}$ so that the modeled flux density for a source can be expressed as $F(t, E, \vec{\Omega}; \vec{\lambda})$.

[1]For more information on models used by Fermi, check: http://fermi.gsfc.nasa.gov/ssc/data/analysis/scitools/source_models.html

4.6.6 Detector Signal

The instruments on Fermi are essentially particle detectors (see section 2.2 for Fermi instrumentation). Therefore, it is important to understand what the modeled source flux density looks like to the detector. The modeled flux density of a source is mapped onto the actual data via the instrument processing of actual events. However, detectors are imperfect and introduce errors on detected photons or fail to generate a signal from incident photons. For example, approximately 40% of photons at normal incidence in the Fermi tracker will pass through without interacting (Atwood *et al.*, 2007) resulting in photons that cannot be reconstructed[1]. The photons that interact will have a spread in reconstructed energies and positions. These factors are characterised by the instrument response function (see section 2.4 for detailed discription of the Fermi IRF), which contains the detector efficiency for successful reconstruction of incident photons and the dispersion from the true observed properties.

4.6.7 Fermi Likelihood

Photon events in Fermi are binned by their observed quantaties such as energy and position. The events can also be binned with respect to time or placed into a single bin for the observation length.

Consider $\vec{N}$ as the set of counts observed in individual bins and each element being Poisson distributed with unknown mean, r_i. The probability mass function for the data are the product of Poisson distributions with rates r_i, since the components of $\vec{N}$ and N_i are statistically independent. The probability to observe N

[1]It is possible to reconstruct some photons using the calorimeter alone, but this is not included in the standard Fermi analysis.

counts, given a Poisson distribution with mean r, is:

$$p(N;r) = \frac{r^N}{N!}\exp(-r) \tag{4.25}$$

However, the rate for a bin of phase space will have contributions from multiple sources due to a combination of strong diffuse background and the broad point spread function (see section 2.4.1) of Fermi. Thus, the logarithm of the binned likelihood for all selected data summed over all bins (N_{bins}) and sources (N_s) can be written as:

$$\begin{aligned}\log L(\vec{\lambda};\vec{N}) &= \sum_{i=1}^{N_{bins}}\left[-\iiint_{bin_i}\sum_{j=1}^{N_s} r_j(t^{'},E^{'},\vec{\Omega}^{'};\vec{\lambda}) + N_i\log\sum_{j=1}^{N_s}\iiint_{bin} r_j(t^{'},E^{'},\vec{\Omega}^{'};\vec{\lambda})\right] \\ &= \sum_{i=1}^{N_{bins}}\left[-\sum_{j=1}^{N_s} C_{ij} + N_i\log\sum_{j=1}^{N_s} C_{ij}\right]\end{aligned} \tag{4.26}$$

using the probability mass function in Equation 4.25. The triple integrals are over the time, energy and position for each bin. The observed counts in the ith bin are denoted by N_i and the expected number of counts in the ith bin from the jth source is defined as C_{ij}. The $N!$ term from Equation 4.25 is independent of the model parameters so is not used.

For Fermi analysis, a region of interest (ROI) is defined to be the section of the total data that is selected instead of using individual bins. The binned likelihood

is then defined as:

$$\log L(\vec{\lambda};\vec{N}) = -\iiint_{ROI}\sum_{j=1}^{N_s} r_j(t',E',\vec{\Omega}';\vec{\lambda}_j) + \sum_{i}^{N_{bins}} N_i \log \sum_{j=1}^{N_s} C_{ij} \tag{4.27}$$

This formulation can also be developed for the unbinned likelihood. Each bin width is taken to be infinitesimal so that only 0 or 1 counts can be observed. The unbinned likelihood is given by:

$$\log L(\vec{\lambda};\vec{N}) = -\iiint_{ROI}\sum_{j=1}^{N_s} r_j(t',E',\vec{\Omega}';\vec{\lambda}_j) + \sum_{i=1}^{N_{events}} \log \sum_{j=1}^{N_s} r_j(t_i',E_i',\vec{\Omega}_i';\vec{\lambda}_j) \tag{4.28}$$

where $\vec{N}$ contains every count and t_i', E_i' and $\vec{\Omega}_i'$ denote the reconstructed time, energy and position of the ith bin. The unbinned likelihood has the advantage of not losing information to binning but can become prohibitive for large samples.

Due to the large data sets analysed with Fermi, both binned and unbinned are computationally intensive. For example, to calculate flux for a typical Fermi source using 3 years of data would take approximately 2 days computer processing time and to produce a TS map for the source would take a week.

Chapter 5

Observations of Likely Fermi Binaries

All the sources analysed are placed into two categories: catalogue sources and non-catalogue sources. The non-catalogue sources (analysed in this chapter) include gamma-ray candidates of particular interest to Fermi. For example PSR B1259-63 (section 5.3) was originally detected by HESS in the periastron of 2004 and a detection with Fermi in the periastron of 2010 would provide a more complete understanding of the source. The catalogue sources (see chapter 6) include all known X-ray and radio binary pulsars with full Fermi analysis searching for any candidates in gamma-rays.

All analysis in this chapter use the latest IRF[1]: Pass 7 version 6. This IRF is superior to the Pass 6 used at launch (Ackermann *et al.*, 2012) and includes updates from in-orbit performance of Fermi. The diffuse models for all analysis are the iso_p7v6 and can be found on the Fermi website[2]. Note that these models

[1]For the latest IRF and improvements, see http://fermi.gsfc.nasa.gov/ssc/data/analysis/documentation/Cicerone/Cicerone_LAT_IRFs/IRF_overview.html

[2]For the latest diffuse models, see http://fermi.gsfc.nasa.gov/ssc/data/access/lat/

are continuously being updated and improved.

5.1 Circinus X-1

Unless otherwise specified, all data analysis and results of Circinus X-1 presented in this chapter are those of the author. The results from the Fermi Collaboration are presented where appropriate for the purposes of comparison with this thesis.

The discovery of Circinus X-1 (Cir X-1 hereafter) was first reported by Margon *et al.* (1971) using observations made from an Aerobee rocket. The first estimates of the distance to Cir X-1 were published by Goss & Mebold (1977), which found a lower limit of 8 kpc, using observations of the HI absorption profile and assuming that the distance to the Galactic centre is 10 kpc. This was later updated by Stewart *et al.* (1991) to a lower limit of 6.5 kpc to Cir X-1, based on the assumption that the distance to the Galactic centre is 8 kpc. Furthermore, Clark *et al.* (1975) placed an upper limit of 9 kpc on the Galactic plane using attenuation of X-rays.

The first determination of the 16.6 $\pm$ 0.1 day periodicity of Cir X-1 was made by Kaluzienski *et al.* (1976) using data obtained from Ariel V. The 16.6 $\pm$ 0.1 day period was also found in periodic radio flares by Whelan *et al.* (1977). Further multi-wavelength observations in the infra-red (Glass, 1978) and optical (Moneti, 1992) regimes found the same 16.6 $\pm$ 0.1 day periodicity, providing us with a firm understanding of the orbital period of the system.

Cir X-1 was analysed using three years (between July 2008 and August 2011) of Fermi data and a counts map of the region is shown in figure 5.1, which also shows the galactic diffuse emission that must be accounted for during further analysis.

`BackgroundModels.html`

Initially, a Test-Statistic Map (TS-Map hereafter; see Section 4.2 for details) was produced with no sources removed from a 5^o diameter field of view centred on Cir X-1 (shown in figure 5.2). The bright source at $\approx 0.5^\circ$ away is the point source 2FGL J1521.8-5735 from the Fermi second year catalogue. No sources are removed from the data for further analysis as we are searching for timing specific to Cir X-1. The significance at Cir X-1 is not high enough to claim positionally coincident detection. This result might be expected since Cir X-1 is known to be a transient X-ray source with periods of flaring separated by months of no activity. Nevertheless, these periods of flaring peaks are separated by 16.6 $\pm$ 0.1 days as expected from the periodicity of Cir X-1. During the periods of flaring, Cir X-1 is believed to be in a high/soft state (see section 1.2 for explanation on spectral states). This is also the spectral state which is believed to be most likely to produce gamma-ray emission. The flaring activity provides the required population of high energy particles that potentially produce gamma-ray emission (see section 1.3 for gamma-ray emission mechanisms).

To complement the Fermi data, X-ray observations of Cir X-1 from the monitor of all-sky X-ray image (MAXI hereafter) observatory are used. MAXI is an all sky X-ray imaging monitor mounted on the International Space Station and consists of sensitive X-ray slit cameras for the monitoring of more than 1000 sources over an energy band range of 0.5 to 30 keV. MAXI was specifically chosen due to the data being publicly available and the contineous monitoring of Cir X-1. The 16.6 $\pm$ 0.1 day periodicity of Cir X-1 is strongly observed in the MAXI data. The full energy range of MAXI (0.5 - 30 keV) is used for all the data in this thesis.

The next step in the analysis of Cir X-1 was to check for any cross correlations (see section 4.4) between the Fermi and MAXI data (light curves of both shown in

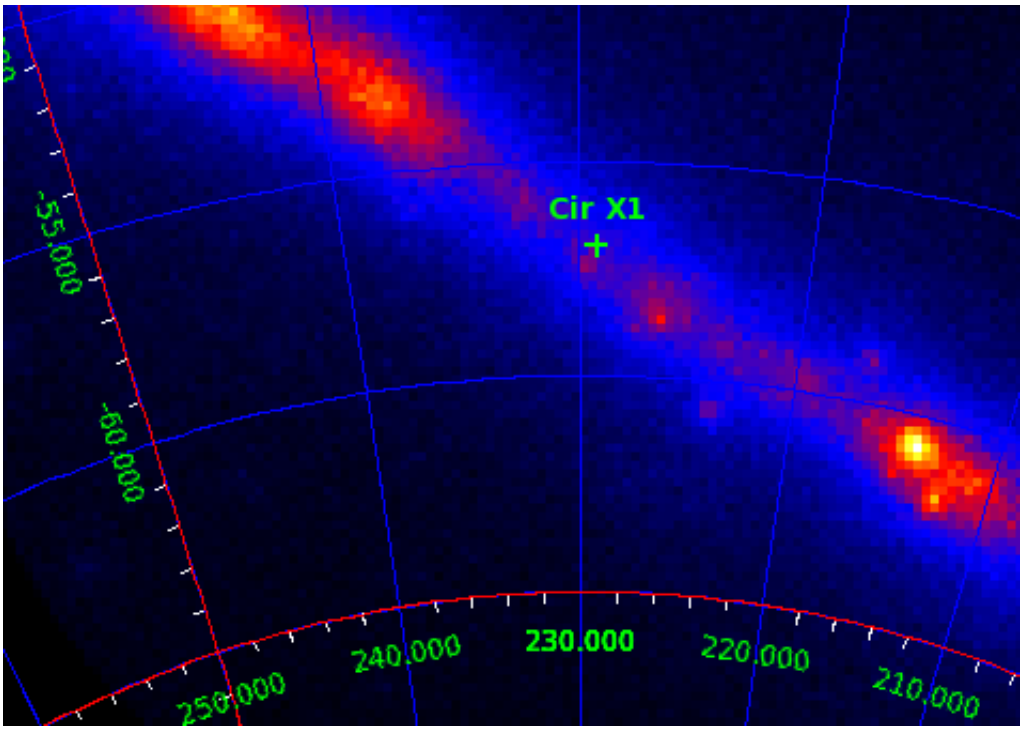

Figure 5.1: *Counts map from Fermi centred on Cir X-1. There are approximately 150 photons per pixel at the position of Cir X-1. The galactic diffuse emission can easily be seen. The minimum energy threshold for the counts map was set to 100 MeV. The colour scale for the photons per pixel is between 5 (dark blue) to 310 (white).*

figure 5.3). Active and quiet periods in the X-ray data from MAXI were correlated with the equivalent periods in the Fermi data. In MJD, the cuts for the quiet period are between 55070 and 55250, which results in 180 days of data for both Fermi and MAXI. The active period is taken between 55300 and 55480, which also provides 180 days of data for Fermi and MAXI. The active period of 180 days was chosen using the MAXI data which showed flaring of Cir X-1. The periods outside the selected 180 days showed no significant flaring activity. The quiet period was limited to 180 days to be consistent with the length of period used for the active time range. The results of the cross correlation for the active period is shown in

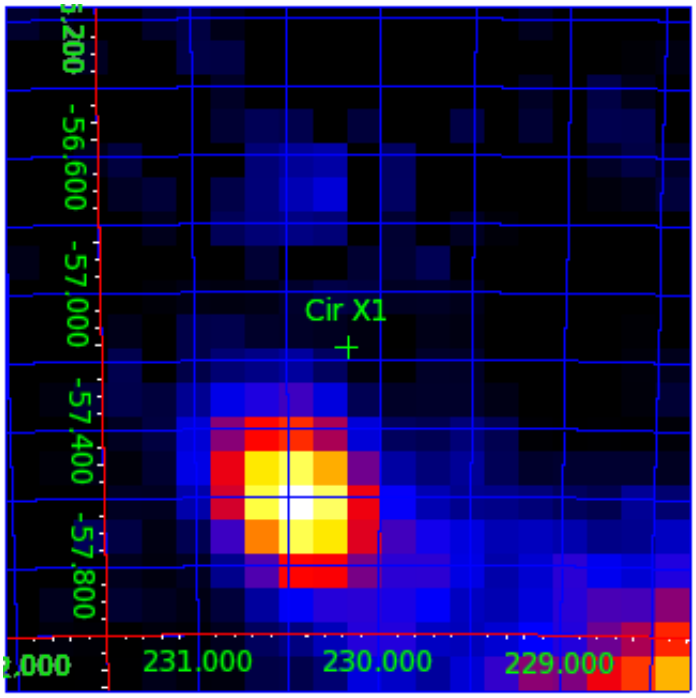

Figure 5.2: *TS-Map of 5º field of view centred on Cir X-1. There is a bright source close to Cir X-1 but the significance at Cir X-1 is not high enough to claim detection. However, timing analysis such as cross-correlation with X-rays can be used as an alternative method of detecting Cir X-1.*

figure 5.4, and the quiet period is shown in figure 5.5. Note that, for both figures, neighboring data points are not independent of each other - hence the fluctuations in the data appear to be less than the error bars would suggest.

The cross correlation results don't show any particular features to suggest a correlation between the X-ray and gamma-ray observations. The active period results shown in figure 5.4 just show a hint of a small correlation at $\sim$ 15 days. This however is not statistically significant (estimated chance probability of 23%) and cannot be definitively associated with the Cir X-1 period of 16.6 $\pm$ 0.1 days. Furthermore, the Fermi satellite precession period third harmonic is approximately 17 days. However, the results for the quiet period shown in figure 5.5 contain no

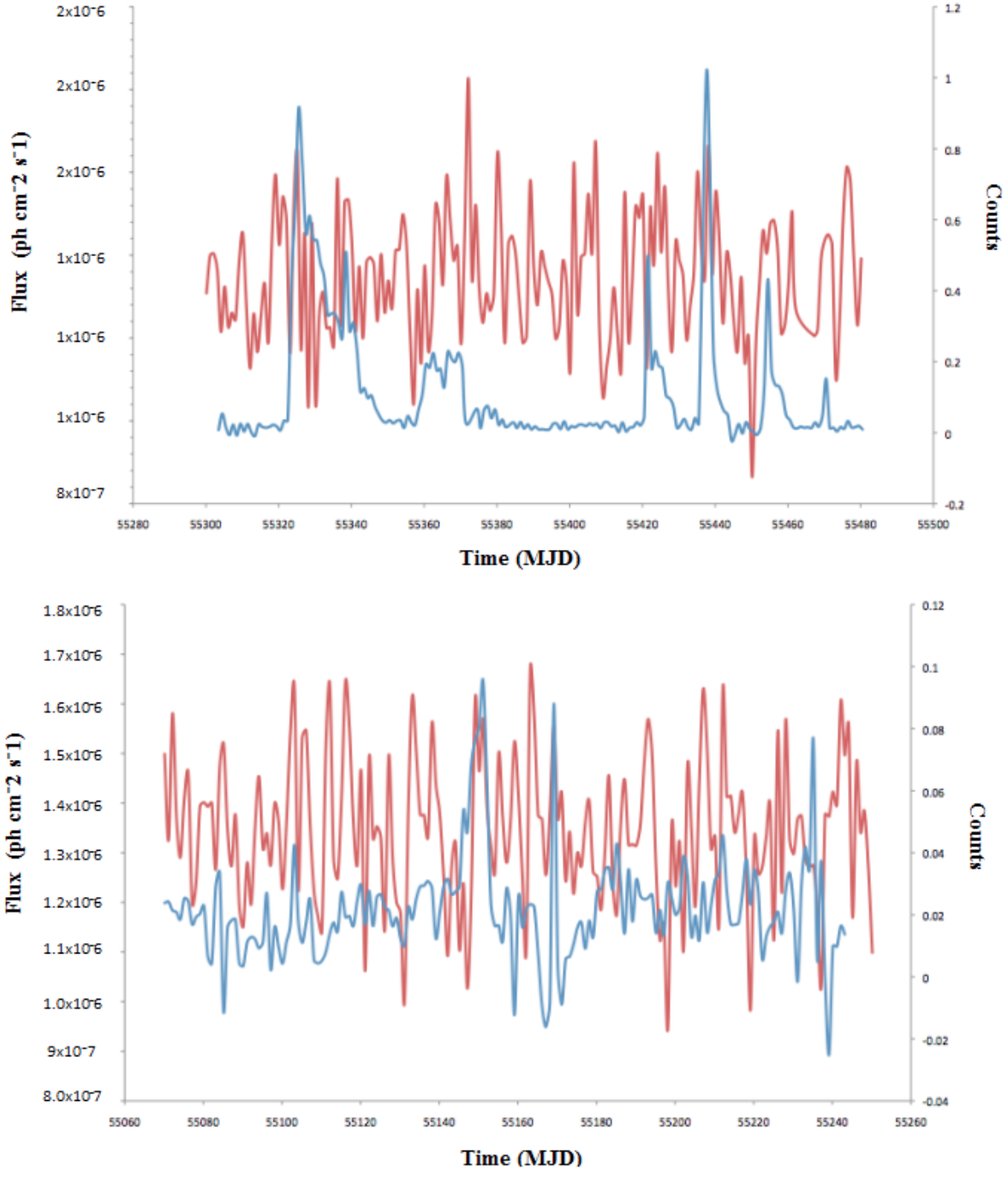

Figure 5.3: *Light curves showing the most active (top) and least active (bottom) period of Cir X-1 in X-rays (in blue) as observed by the Maxi observatory for the past 3 years plotted with the same period from Fermi (in red). The Fermi cuts include all photons with energies greater than 100 MeV and within 3.5º of Cir X-1. Error bars on Fermi are not shown for clarity.*

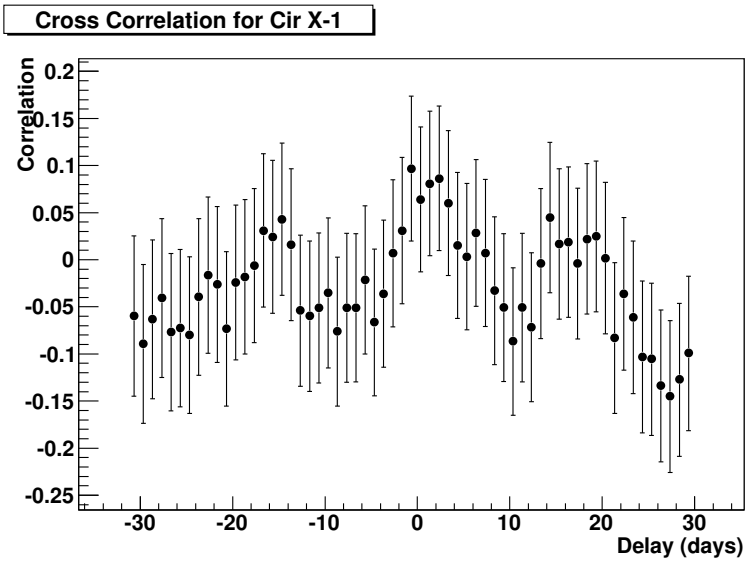

Figure 5.4: *Z-transformed discrete correlation function for the active period for Cir X-1. The data for both Fermi and MAXI are taken between 55300 and 55480 MJD. The Fermi cuts include all photons with energies greater than 300 MeV and within 3.5º of Cir X-1.*

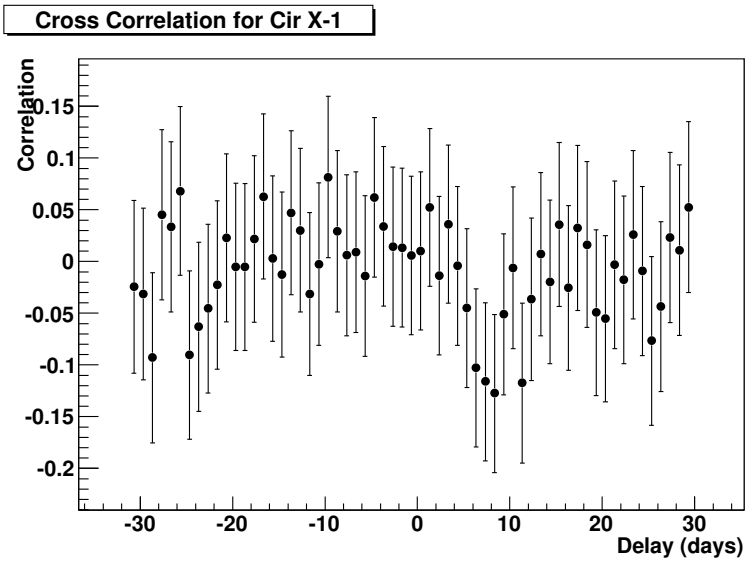

Figure 5.5: *Z-transformed discrete correlation function result on the quiet period for Cir X-1. The data for both Fermi and MAXI is taken between 55070 and 55250 MJD. The Fermi cuts include all photons with energies greater than 300 MeV and within 3.5º of Cir X-1.*

evidence for either the Cir X-1 orbital period or for a cross correlation with the X-ray data.

The 16.6 ± 0.1 day periodicity of Cir X-1 can also be searched in the Fermi data. For an evenly sampled data set, a fast Fourier transform (FFT) algorithm can be used. However, since Fermi is an orbiting satellite with all sky coverage, the data for Cir X-1 is unevenly sampled and there are several days with zero counts. The Lomb-Scargle periodogram is chosen for this analysis and the Fermi data are split into two 3.5^o fields of view and the resulting periodograms are shown in figures 5.6 and 5.7. The data for figures 5.6 and 5.7 are centred on Cir X-1 and approximately 9^o away from Cir X-1, respectively. They are both from the full Fermi data set and contain photons with energies greater than 300 MeV. Both figures clearly show the major issue with periodicity analysis of any Fermi data as the satellite itself has a precession period of approximately 52 days and this presents itself as peaks at 54 and 27 days in the periodogram. Neither figures show the 16.6 ± 0.1 day period of Cir X-1. However, in the 180 day data from the active period, the periodogram (figure 5.8) shows the position of the 16.6 ± 0.1 day period of Cir X-1, with a significance of 96% (i.e. a probability of occurrence by chance of 4%).

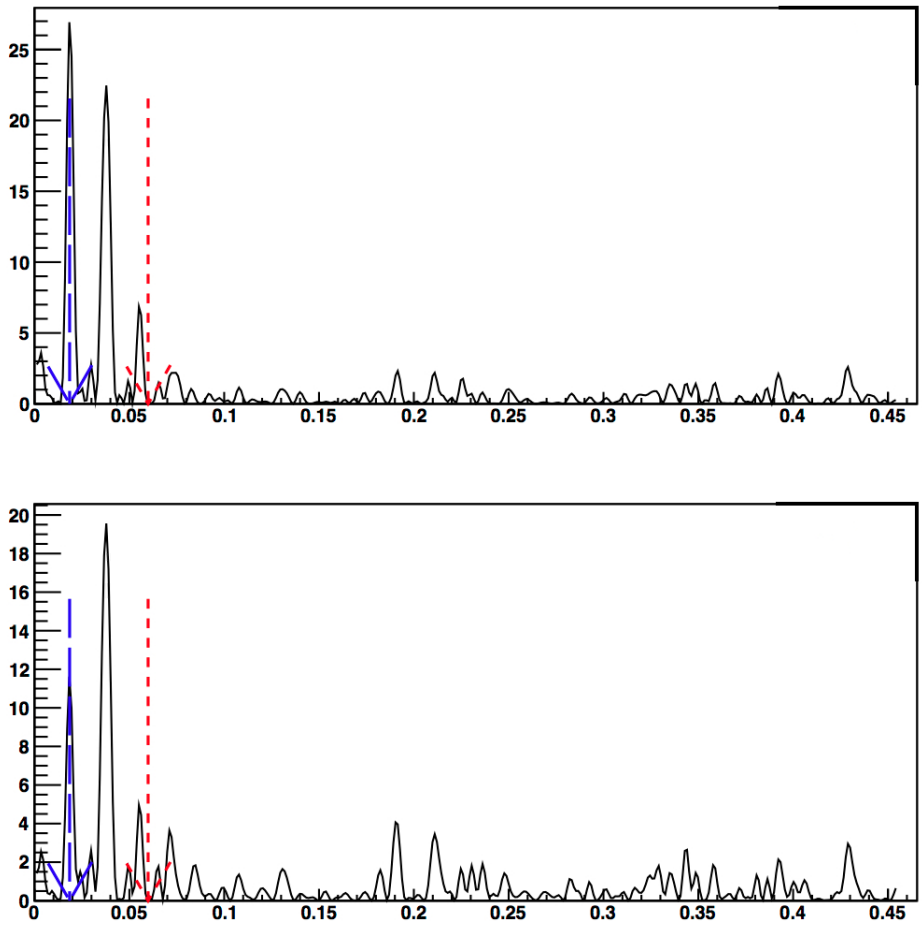

Figure 5.6: *Lomb-Scargle periodogram of the full Fermi data centered on Cir X-1, with minimum energy cuts of 100 MeV (top) and 300 MeV (bottom). The analysis includes all photons within 3.5^o of Cir X-1. The X-axis is the period in 1/days, with the red arrow representing the 16.6 $\pm$ 0.1 day period of Cir X-1 and the blue arrow representing the 54 day precession period of Fermi.*

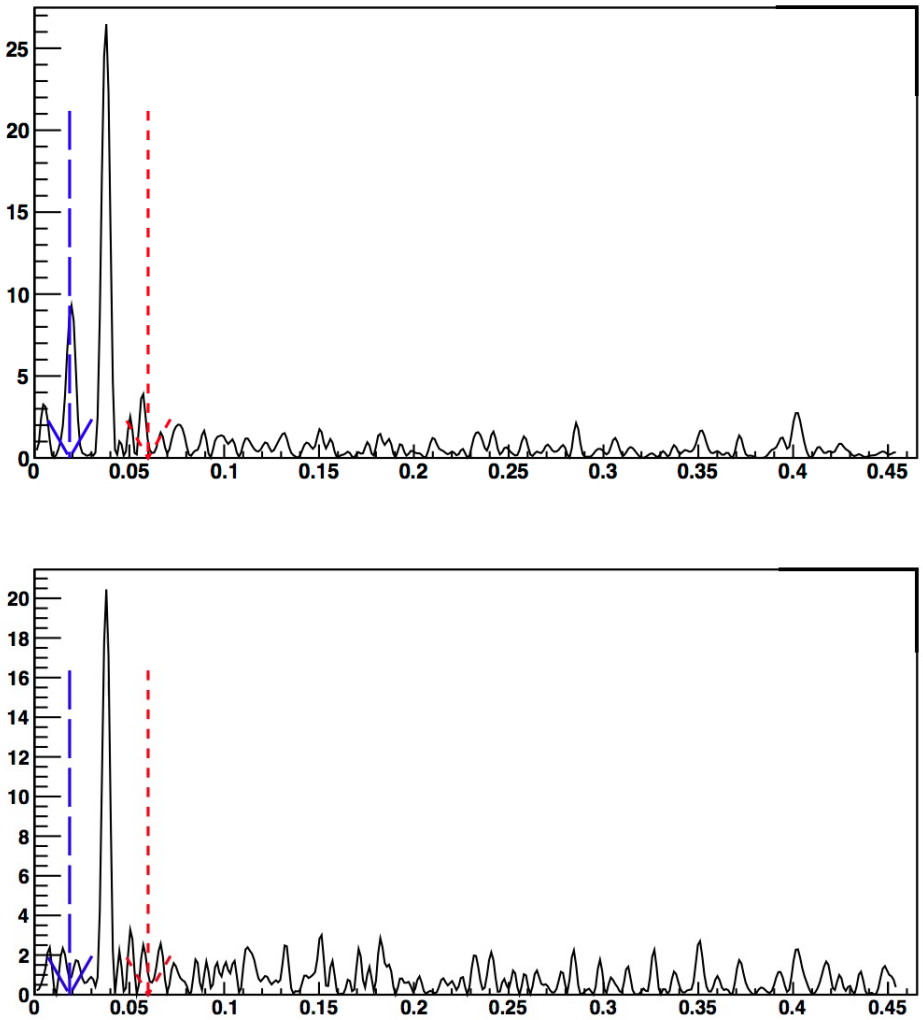

Figure 5.7: *Lomb-Scargle periodogram of the full Fermi data centered on approximately 9º away from Cir X-1, with minimum energy cuts of 100 MeV (top) and 300 MeV (bottom). The analysis includes all photons within 3.5º. The X-axis is the period in 1/days, with the red arrow representing the 16.6 ± 0.1 day period of Cir X-1 and the blue arrow representing the 54 day precession period of Fermi.*

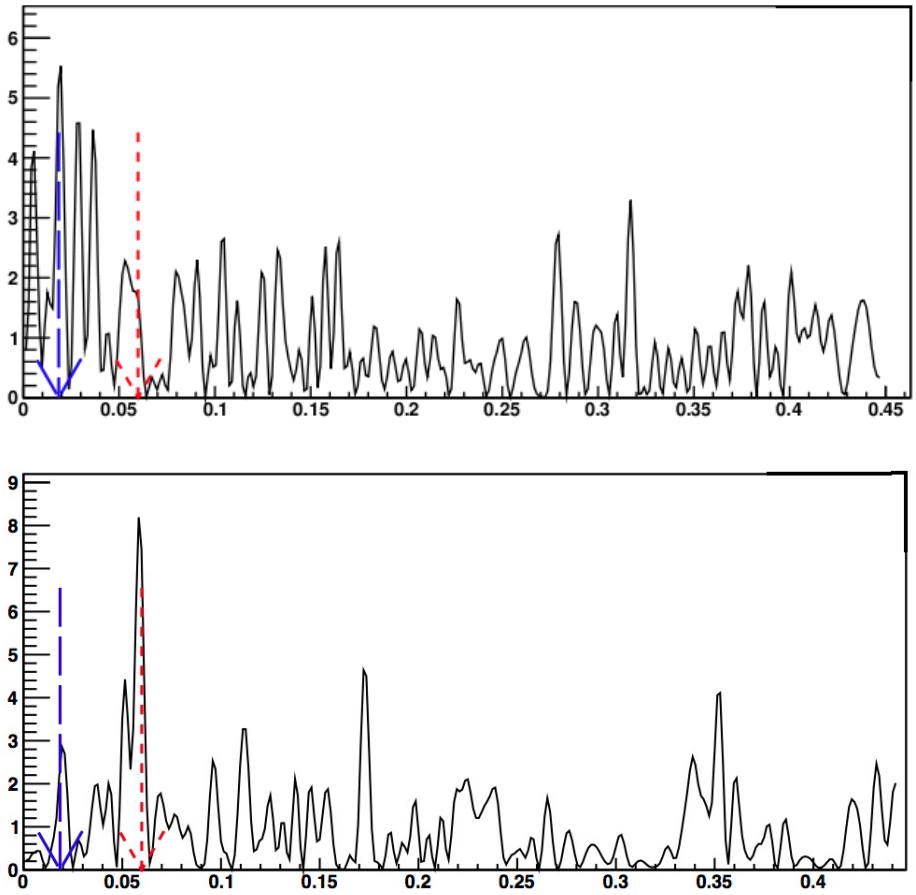

Figure 5.8: *Lomb-Scargle periodogram of Fermi data (the active 180 days) centered on Cir X-1. The X-axis is the period in 1/days, with the red arrow representing the 16.6 ± 0.1 day period of Cir X-1 and the blue arrow representing the 54 day precession period of Fermi. The Fermi cuts include all photons with energies greater than 100 MeV (top) and 300 MeV (bottom) and within 3.5º of Cir X-1.*

5.2 Cygnus X-3

Unless otherwise specified, all data analysis and results of Cygnus X-3 presented in this chapter are those of the author. The results from the Fermi Collaboration are presented where appropriate for the purposes of comparison with this thesis.

The region around Cygnus X-3 is challenging to analyse as it contains 3 bright gamma-ray pulsars combined with high levels of diffuse emission. PSR J2032+4127 is within 0.5 degrees of Cygnus X-3 and contributes a significant proportion of photons that are detected by Fermi in the location of Cygnus X-3. Figure 5.9 shows the counts map produced from the full 3 year Fermi data with a minimum energy cut of 100 MeV. The TS-Map of the region is shown in figure 5.10, which also shows the emission from PSR J2032+4127. The pulsar has a rotation period of 0.143 seconds.

The Fermi-LAT analysis of Cygnus X-3 spans data taken from 4 August 2008 to 2 September 2009 and yields a detection of a point source at the level of 5.5σ between 8 June to 2 August 2009 (MJD 54990 - 55045), which was an active flaring period (Fermi LAT Collaboration, 2009b). There is no detection of Cygnus X-3 in the data set outside of the active flaring period. The pulsar gating technique (see section 4.5) is used. By only accepting photons which arrive during the off-pulse phase of the pulsar we can preserve up to 80% of the photons from Cygnus X-3. However, this is strongly dependent on the cuts used for the off-pulse phase and there is still some pulsar emission present in the analysis. Nevertheless, the cleaned data was used to produce a phase folded light curve of Cygnus X-3 (using the ephemeris from Singh *et al.* (2002) - reproduced on table 5.1), which is shown in figure 5.11. For comparison, a phase folded light curve from RXTE between

1.5-12 keV (Levine *et al.*, 1996) is shown in figure 5.12.

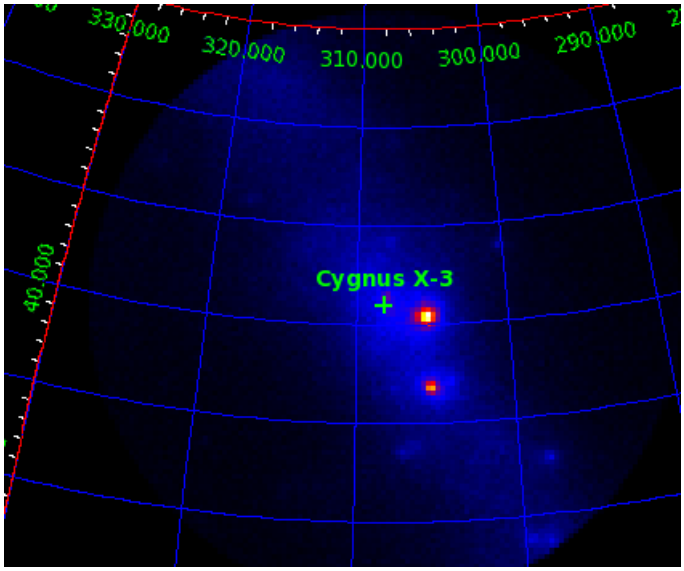

Figure 5.9: *Counts map from Fermi centred on Cygnus X-3. There are approximately 600 photons per pixel at the position of Cygnus X-3. The galactic diffuse emission can easily be seen. The minimum energy threshold for the counts map was set to 100 MeV. The colour scale for the photons per pixel is between 5 (dark blue) to 2450 (white)*

Parabolic ephemeris for Cygnus X-3
$T_0 = 2440949.892 \pm 0.001$ J D
$P_0 = 0.19968443 \pm 0.00000009$ d
$\dot{P} = (5.76 \pm 0.24)$ x 10^{-10}
$\dot{P}/P_0 = (1.05 \pm 0.04)$ x 10^{-6} yr^{-1}

Table 5.1: *Parabolic ephemeris for Cygnus X-3 from Singh et al. (2002), which is used to produce the phase folded light curve shown in figure 5.11.*

The association of Cygnus X-3 to the active flaring period is definitively confirmed with the detection of the 4.8 hour orbital period in figure 5.11. No orbital

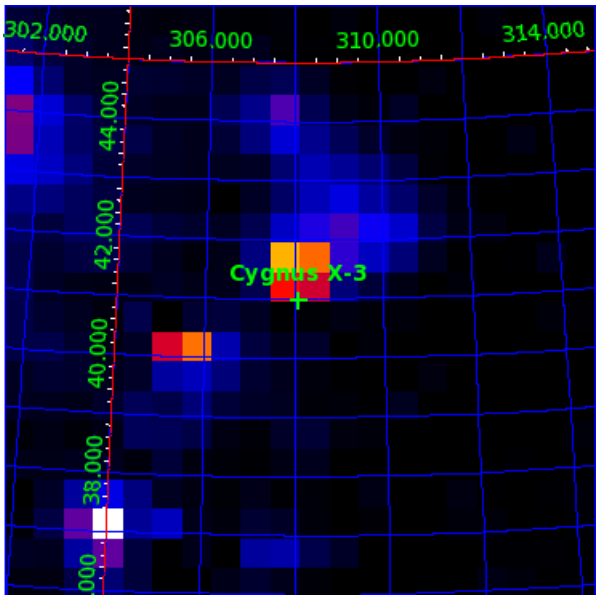

Figure 5.10: *TS-Map of 5º field of view centred on Cygnus X-3. There are two bright sources within close proximity to Cygnus X-3. Cygnus X-3 lies on the edge of two pixels with high significance but this is not enough to claim detection.*

periodicity is evident when using the full data set (between 4 August 2008 to 2 September 2009). Comparing the Fermi-LAT folded light curve in figure 5.11 with the RXTE folded light curve in figure 5.12 shows that both have the same asymmetric shape with a slow rise and faster decay. The Fermi-LAT maximum is in phase with the X-ray maximum. The Fermi-LAT detection is compatible with the extrapolation of the hard X-ray tail observed up to several 100 keV by Hjalmarsdotter *et al.* (2009). The gamma-ray emission detected by Fermi could be explained by the inverse Compton scattering (see section 1.3.1) of ultraviolet photons from the Wolf Rayet star off of high energy electrons. However, the emission region and accretion disc cannot be close as this would result in the gamma-ray emission being absorbed via pair production on the soft X-ray photons from the disc.

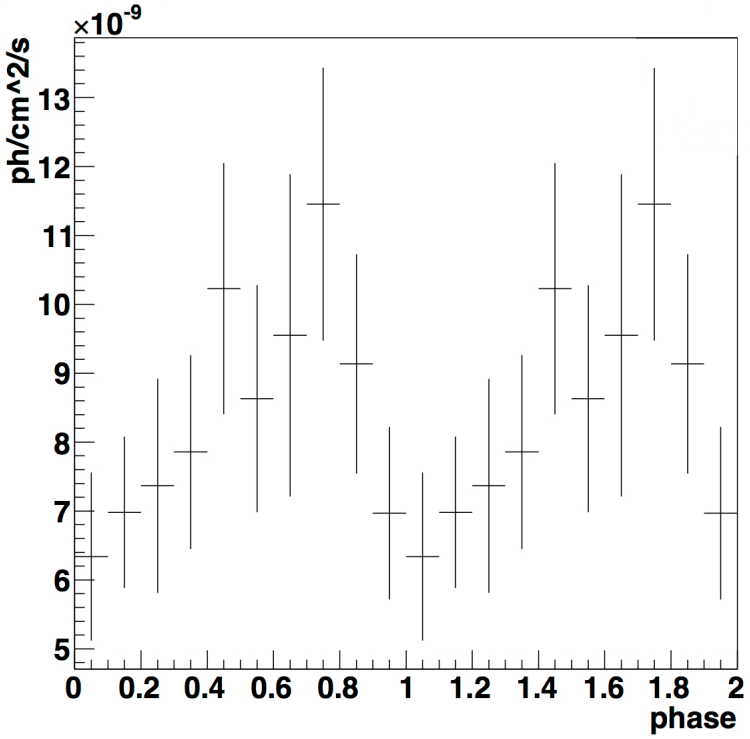

Figure 5.11: *Phase folded, on 4.8 hour orbital period, light curve of the region centred on Cygnus X-3. The data are phase gated to remove the effect of PSR J2032+4127. The Fermi cuts include all photons with energies greater than 100 MeV.*

In the above scenario where inverse Compton scattering (see section 1.3.1) is the dominant gamma-ray production method, the peak in gamma-ray detection would occur during the time of superior conjuction when the electrons are seen (from Earth) behind the Wolf Rayet star and therefore undergo head-on collisions with the ultraviolet photons. Under the assumption that the X-ray modulation is produced via the Compton scattering in the Wolf Rayet star, the peak in gamma-ray emission would correspond to the X-ray maximum. This is approximately observed in figures 5.11 and 5.12.

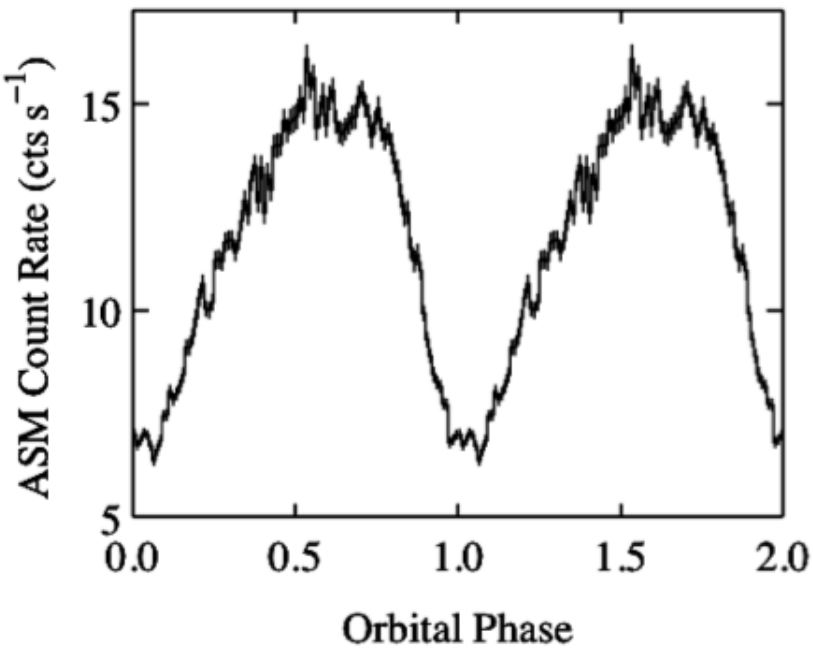

Figure 5.12: *RXTE ASM light curve of Cygnus X-3 folded on the orbital period. The light curve is built with the data over the entire lifetime of RXTE. Phase zero is set to be at the point of superior conjunction. Figure from citeAbdo09*

5.3 PSR B1259-63

Unless otherwise specified, all data analysis and results of PSR B1259-63 presented in this chapter are those of the author. The results from the Fermi Collaboration are presented where appropriate for the purposes of comparison with this thesis.

PSR B1259-63 was initially analysed using data from Fermi launch (July 2010) to November 2010. A detection was not expected as periastron was predicted to be 15th December 2010. The counts map of the region is shown in figure 5.13, which shows approximately 200 photons per pixel at the position of PSR B1259-63 with a minimum energy cut of 100 MeV. A TS-Map of the region is shown in figure 5.14 without a significant detection of PSR B1259-63. The total TS for the pre-periastron period (July to November 2010) is 0.01 with spectral index of -2.07 $\pm$ 1.1. The upperlimit flux above 100 MeV is 2.48 x 10^{-12} $\pm$ 2.30 x 10^{-11} photons cm^{-2} s^{-1}.

A set of tools were developed during the pre-periastron period (July to November 2010) by the author to automatically download and analyse Fermi data for PSR B1259-63. The data was automatically analysed every 3 days. A 4 sigma detection was found on the 21st of November 2010 at 5:00 UT. However, the author did not report this detection through Atel as the minimum threshold for detection was set to 5 sigma to be consistent with the standard used by the Fermi Collaboration.

The first published claim of a detection with Fermi was by Tam *et al.* (2010) on the 21st of November 2010 at 7:15 UT, which also found increased activity in Swift-XRT. After the 21st of November 2010, the flux from PSR B1259-63 decreased below the detection levels of Fermi and on the 24th of November, the

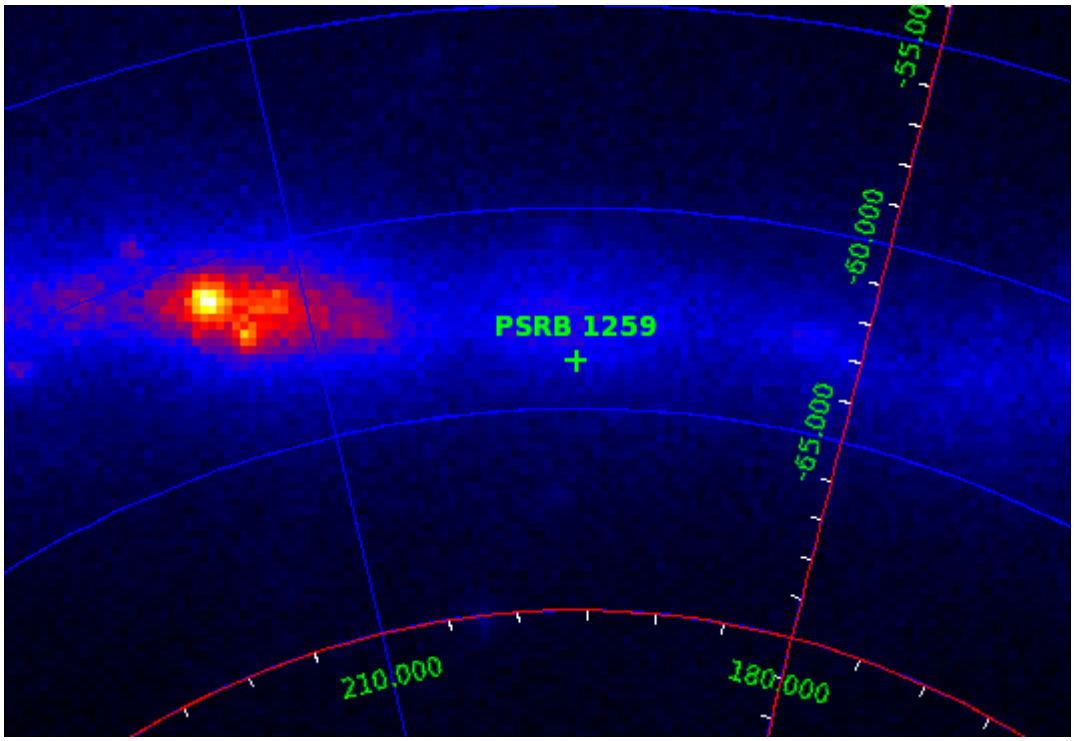

Figure 5.13: *Counts map from Fermi centred on PSR B1259-63. There are approximately 200 photons per pixel at the position of PSR B1259-63. The minimum energy threshold for the counts map was set to 100 MeV. The colour scale for the photons per pixel is between 5 (dark blue) to 850 (white).*

Fermi collaboration published an Atel stating that the chance probability of the detection on the 21st of November is of the order 1%, which they considered to be too high to establish a secure detection. There was another detection in the middle of December 2010 but this was also relatively weak. On the 27th of December, Fermi was put on a modified sky survey mode which increased the exposure received by the southern hemisphere by 30% without interrupting the rest of the sky too much as would have been the case for a pointed observation. There was also a continued multiwavelength monitoring of PSR B1259-63 up to April 2011, which is after the passage of the pulsar through the dense equatorial

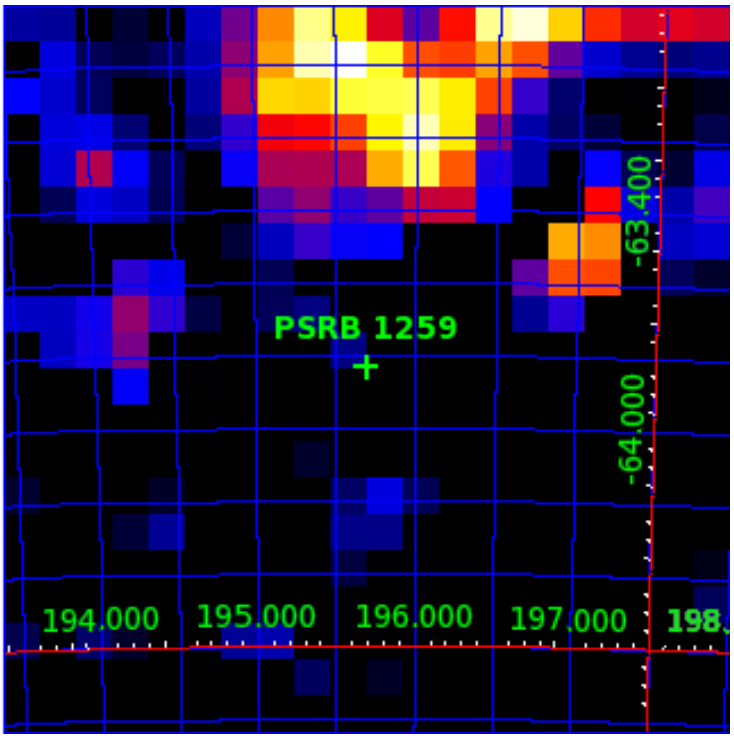

Figure 5.14: *TS-Map of 5º field of view centred on PSR B1259-63. There is no significant detection of PSR B1259-63, which is expected as there was no emission up to November 2010. The data used above contains all Fermi events from launch up to November 2010 centred on PSR B1259-63.*

wind of the massive companion star.

Data from Fermi between 15th November 2010 and 15th March 2011 was analysed and the light curve is shown in figures 5.15 - 5.18. Each light curve represents 30 days of data so that a total of 120 days is analysed during the PSR B1259-63 periastron. Each light curve is also split into 10 bins so that each bin contains 3 days of data. The Fermi Collaboration light curve (shown in figure 5.20) uses weekly bins in comparison. The first 60 days (figures 5.15 and 5.16) show very little activity, which is also corroborated by the Fermi Collaboration results (Abdo *et al.*, 2011). However, the third 30 days (between 15th January and 15th Febru-

ary) show clear detection of PSR B1259-63 with a test statistic of $\sim$ 25 which corresponds to a detection significance of $\sim 5\sigma$. There is also some detection for the first 9 days of the fourth 30 days (between 15th February and 15th March) but there is no detection of PSR B1259-63 after this and upperlimits are produced.

Note that all the figures use the profile method of maximum likelihood analysis. The profile technique assumes that the likelihood profile has a gaussian shape and that the minimum is in the physical parameter space. The integral method, on the other hand, computes the actual profile and searches for the 95% containement. For very low TS (1, 2 or less) then the assumption of gaussianity is wrong and Integral is the best suited method. However, the integral method is computationally more intensive so the profile method is used throughout. The reduced accuracy of the profile method at low TS results in some upper limits appearing higher than detections.

The spectral index of PSR B1259-63 during the same time range is shown in figure 5.19. The spectral index softens from 1.7-2.3 during the brightening to a peak of $\approx$ 4 at the flare. The index then hardens for the rest of the flare period. The Fermi Collaboration results (figure 5.20), in comparison, softens from 2-2.5 during the brightening to a value of 3.5 at the flare peak. However, the Fermi Collaboration flare peak occurs approximately 35 days after periastron compared to approximately 15 days for figure 5.19. However, there is also a spectral index of approximately 3.5 in figure 5.19 which occurs approximately 35 days after periastron and is consistent with the Fermi Collaboration results shown in figure 5.20. In fact, the analysis here and those of the Fermi Collaboration are consistent, except for the peak spectral index of approximately 4 occuring 15 days after periastron which is absent from the Fermi Collaboration results in figure 5.20. The

light curve for this time bin (shown in figure 5.17) also shows a clear detection of PSR B1259-63, which is absent from the Fermi Collaboration result in figure 5.20 (upper panel). One possible explanation for this difference is in the size of the data bins. The Fermi Collaboration results use 7 day bins compared to the 3 day bins used in this analysis. The smaller bin sizes were chosen to extract as much variability information from PSR B1259-63 as possible. The difference could also be due to the different IRF used for this thesis and that of the Fermi Collaboration. The IRF used here is Pass_7_V6 which is superior to the Pass 6 used by the Fermi Collaboration for the PSR B1259-63 analysis.

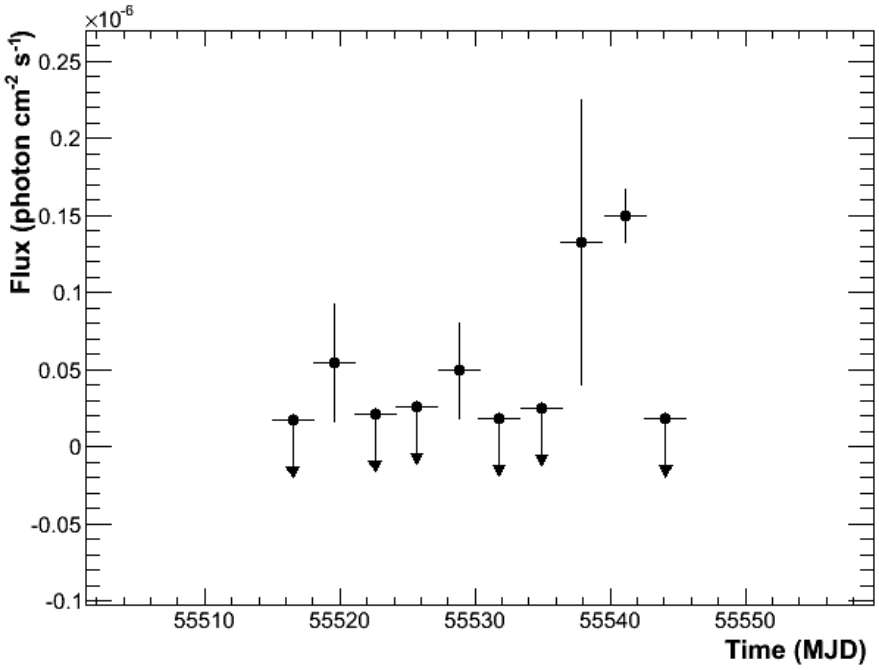

Figure 5.15: *30 day Gamma-ray flux of PSR B1259-63 between 15th November 2010 and 15th December 2010. The data are split into 10 bins so that each bin contains 3 days of data.*

Multiwavelength emission from the PSR B1259-63 system is produced via the interaction of the pulsar wind with the stellar wind of the companion star. The

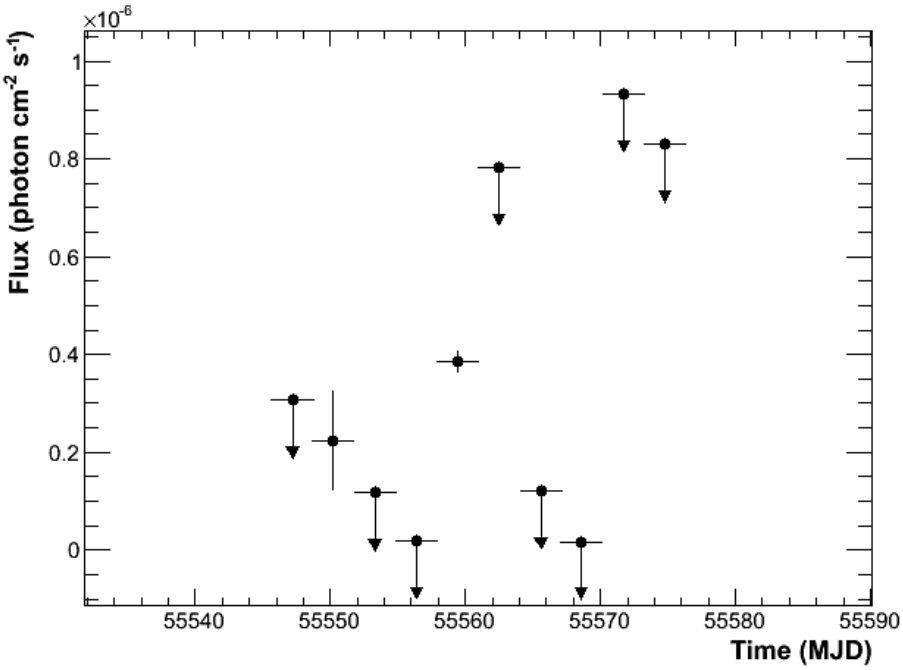

Figure 5.16: *30 day Gamma-ray flux of PSR B1259-63 between 15th December 2010 and 15th January 2011. The data are split into 10 bins so that each bin contains 3 days of data.*

characteristic variability of this emission during the periods of periastron passage have been observed in radio, X-ray and TeV gamma-ray bands (Johnston *et al.* (1992); Kawachi *et al.* (2004); Chernyakova (2006)). Therefore, detection of PSR B1259-63 in the GeV gamma-ray band was not unexpected. However, the analysis presented here reveal interesting characteristics of PSR B1259-63 that were not predicted in previous models of gamma-ray emission from the system. The strong flare that occured approximately 15 days after the periastron was not only unexpected, but also only observed in the GeV gamma-ray band. The flare also continued to be observed after the neutron star passage of the dense equatorial wind of the massive companion star.

Furthermore, the analysis of the flare shows an extremely efficient conversion of

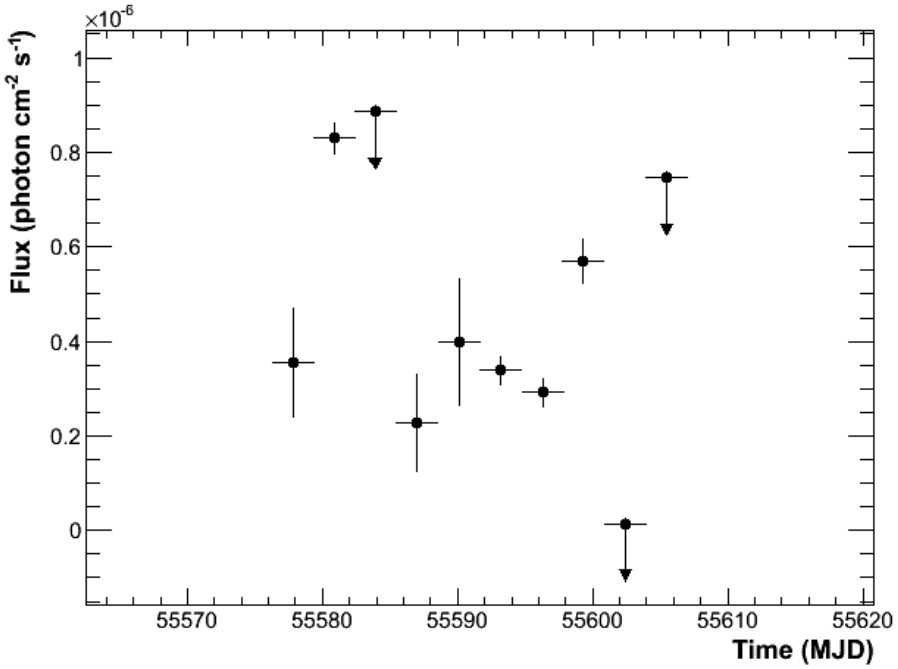

Figure 5.17: *30 day Gamma-ray flux of PSR B1259-63 between 15th January 2011 and 15th February 2011. The data are split into 10 bins so that each bin contains 3 days of data.*

pulsar spin down power into gamma-rays. The highest single day average flux was $\sim$ 3.6 x 10^{-6} cm^{-2} s^{-1}, which corresponds to an isotropic gamma-ray luminosity of $\sim$ 8.2 x 10^{35} erg s^{-1} at a distance of 2.3 kpc. This is almost the same as the estimated total pulsar spin down luminosity of $\simeq$ 8.3 x 10^{35} erg s^{-1} (Johnston *et al.*, 1992).

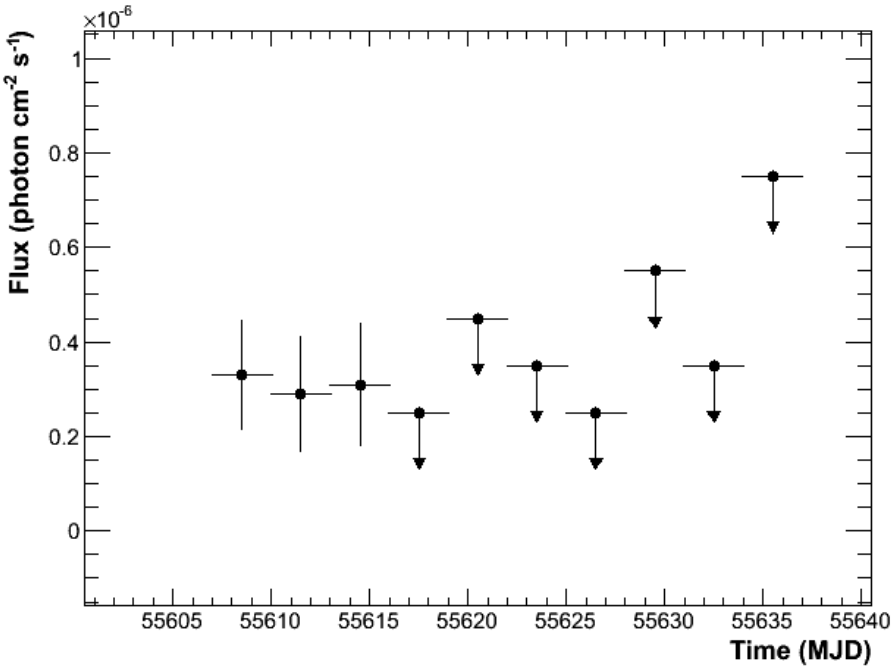

Figure 5.18: *30 day Gamma-ray flux of PSR B1259-63 between 15th February 2011 and 15th March 2011. The data are split into 10 bins so that each bin contains 3 days of data.*

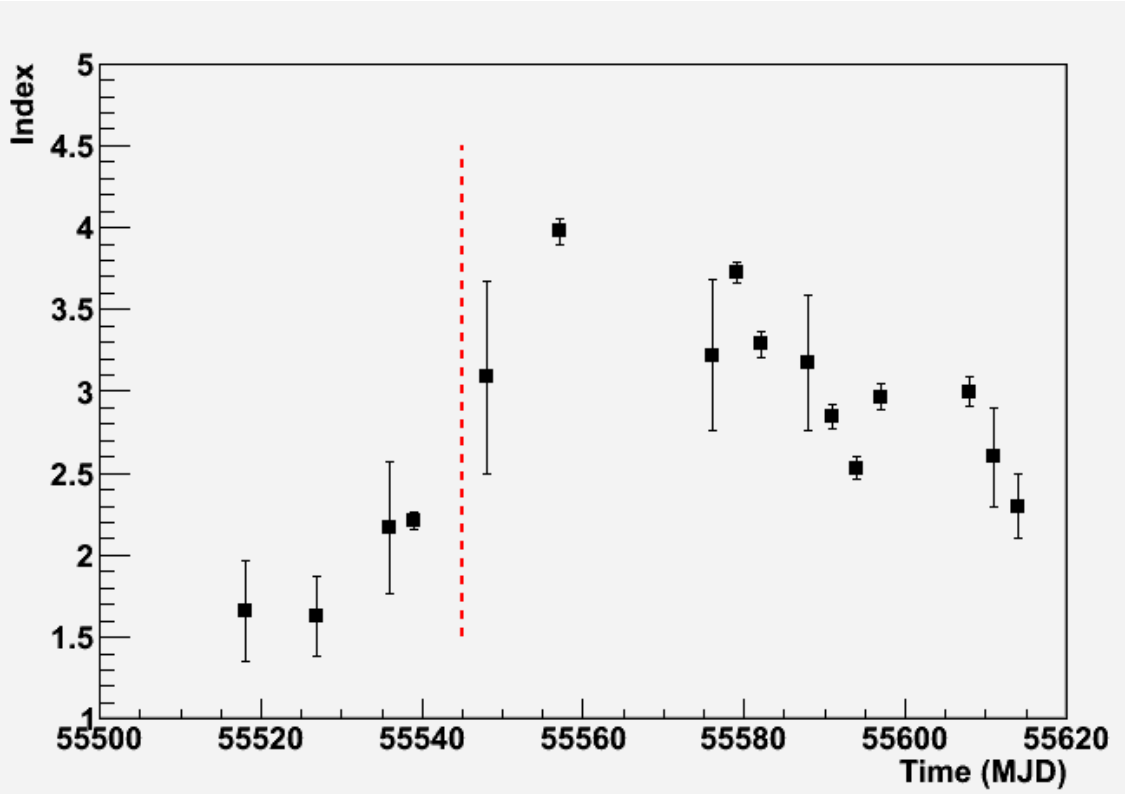

Figure 5.19: *Spectral index of PSR B1259-63 during the time of periastron. The red dashed line represents the expected date of periastron (15th December 2010). The minimum energy cut for this plot is 100 MeV to keep consistent with the Fermi Collaboration analysis shown in figure 5.20.*

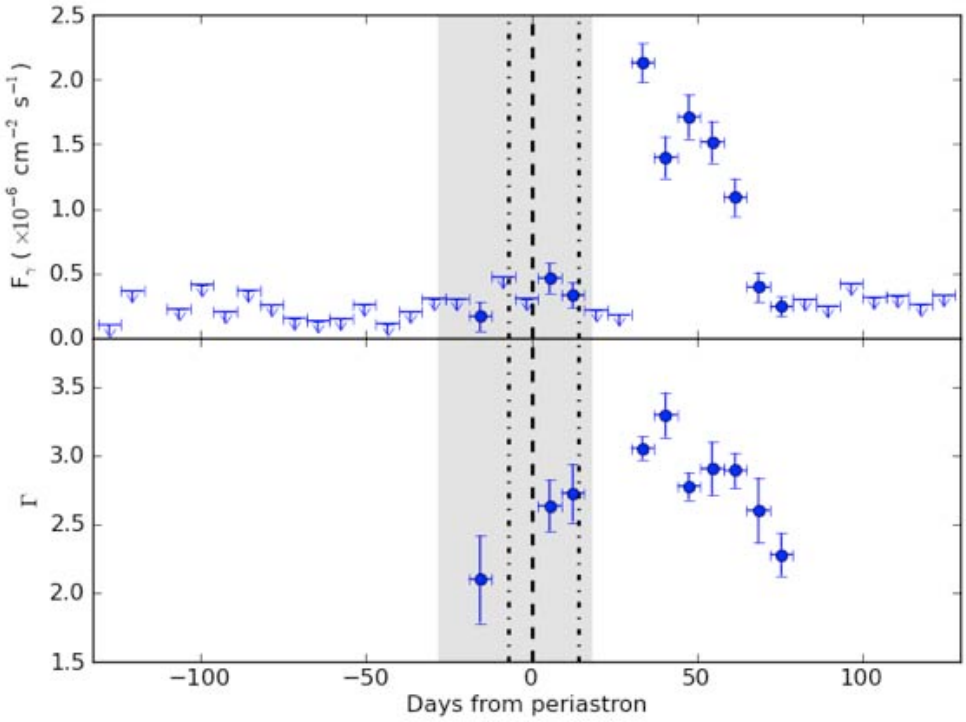

Figure 5.20: *Gamma-ray flux and photon index of PSR B1259-63 in weekly time bins (plot from Abdo et al. (2011)). The upper panel shows the flux above 100 MeV with 2σ upper limits for points with TS < 5. The lower panel shows the variations of spectral index of a power law spectrum with the shaded area representing the brightening period and the dashed like marking the time of periastron. The dashed-dotted lines represent the orbital phase during which EGRET observed PSR B1259-63 in 1994 (Tavani et al., 1996).*

Chapter 6

A Search for Binary Pulsars in the Fermi Data

Unless otherwise specified, all data analysis and results presented in this chapter are those of the author. The relevant X-ray light curves from MAXI are presented where appropriate for the purposes of comparison with this thesis.

All analysis in this chapter use the latest IRF[1]: Pass 7 version 6. This IRF is superior to the Pass 6 used at launch (Ackermann *et al.*, 2012) and includes updates from in-orbit performance of Fermi. The diffuse models for all analysis are the iso_p7v6 and can be found on the Fermi website[2]. Note that these models are continuously being updated and improved.

The catalogues of radio binary pulsars compiled by Wm. Robert Johnston[3] (updated 2005) and X-ray binary pulsars compiled by Mauro Orlandini[4] (updated

[1]For the latest IRF and improvements, see http://fermi.gsfc.nasa.gov/ssc/data/analysis/documentation/Cicerone/Cicerone_LAT_IRFs/IRF_overview.html

[2]For the latest diffuse models, see http://fermi.gsfc.nasa.gov/ssc/data/access/lat/BackgroundModels.html

[3]http://hera.ph1.uni-koeln.de/~heintzma/Diverses/PSR-bin-List.htm

[4]http://www.iasfbo.inaf.it/~mauro/pulsar_list.html

2004) are analysed with Fermi. All data are initially analysed using recommended Fermi analysis chains (see section 2.5) to identify the best cuts for time and maximise signal to noise ratio. The energy and RoI cuts are fixed at 200 MeV to 300 GeV and 10 deg, respectively. All source models (from the Fermi Second Source Catalog (Nolan *et al.*, 2012)) within 10 degrees of the candidates are included with fixed model parameters for flux and spectral index. All source models within 3 degrees of the candidates have free parameters. All the sources are analysed with Fermi data between launch and August 2012. A summary of the results for the X-ray and radio catalogues analyses are shown in tables A.1 and B.1, respectively.

The full Fermi data for each source is downloaded from `http://fermi.gsfc.nasa.gov/ssc/data/access/`. To keep the analysis between sources consistent, the same cuts for energy, time and radius of interest are used. The only variables are the positions of each source. The analysis of each source is also kept the same using analysis scripts. The *gtselect* and *gtmktime* tools from Fermi are initially used to fix the energy and RoI cuts at 200 MeV to 300 GeV and 10°, respectively. Following the data selection cuts, the *gtltcube* and *gtexpmap* tools from Fermi are used to generate exposure maps. The final analysis tool is *gtlike*, which is used to find the source significance given an input model. The input model is the distribution of gamma-ray sources in the sky, and includes their intensity and spectra, as well as taking into account the galactic and extragalactic contributions given the source region. Each source will have a different input model but the radius of interest cuts are kept fixed at 10°. After the initial analysis, all sources with TS $>$ 25 are analysed further by splitting the full time range into 20 bins. The entire analysis chain is repeated on each of the 20 bins. The aim at this stage is to find any particular periods of high activity that could be further investigated.

Any sources with bins of interest are then analysed using the timing analysis in section 4.3.

The initial analysis of each source used approximately 170 CPU hours. The HEAC computer cluster at the University of Leeds was used for all analysis. The total number of available CPU cores for the analysis was 10. At maximum capacity, only 10 sources could be analysed per 7 day week. It therefore took approximately 20 weeks to complete initial analysis of all catalogue sources. Further analysis was required for the 17 sources shown in table 6.1, which took further 2 weeks. All these times of course do not take into account issues that developed during analysis such as failed CPU cores and computer cluster downtime.

Each stage of source analysis required custom scripts, which were written and modified for individual sources as required. This included the automated analysis of each source in the computer cluster and the implementation of the timing analysis described in section 4.3.

Figures 6.1 and 6.2 show the distribution of TS values from the sources analysed in tables A.1 and B.1. The tables use the same values and the only difference is in the log axis used for figure 6.1. The top panels for each figure show the total counts as a function of TS values. The bottom panels show the the expected random TS distribution for comparison with the data. The distributions are approximately Gaussian and centered on zero. Figure 6.3 shows the expected cumulative distribution of TS with the observed distribution.

As can be seen from Figure 6.3, the expected cumulative distribution of TS values under the null (no extra source) hypothesis falls significantly below the observed distribution. Naively, this could be taken as statistical evidence for a substantial class of new emitters but caution is needed. Firstly, the expected

distribution is only an asymptotic expectation (Wilks Theorem) so deviations at relatively small TS values are to be expected. Secondly, and more importantly for the case of large TS values, the catalogue set of potential sources represents a highly non-independent group: many of the tested directions are clustered in small regions of the sky (as expected from the general galactic distribution of such sources). Consequently many of the tested directions differ in direction by much less than the Fermi photon PSF; the TS values of nearby sources are contaminated by their neighbours. A good example in the full summary list of catalogue sources (Appendix A) is the source J0052.1-7319 (TS = 8.4) and nearby J0053-724 (TS = 16.2) and J0051-733 (TS = 10.0).

An alternative method to try to establish the expected distribution of TS under the null hypothesis would be by MC simulation of randomly chosen non-source sky positions. Unfortunately, the source confusion for Fermi prohibits this; in regions of the sky appropriate for the test, where galactic diffuse emission is very high, there are too many sources and in darker (off the galactic plane) regions such a test would not have comparable backgrounds.

We are thus forced to apply a somewhat arbitrary TS cut on the distribution shown in Figure 6.2 - which was chosen, a priori, as TS $>$ 25. The only statistical evaluation of the significance of a detection will then only be made if additional evidence from time variability, or periodicity, is obtained (see Chapter 7).

All sources with TS $>$ 25 (table 6.1) are further analysed. The full time range for each source is split into 20 bins to confirm for any active periods. However, only 3 sources (see table 6.2) have bins with TS $>$ 20. These 3 sources are classed as "of interest" and the techniques described in section 4.3 can be used to identify them as possible gamma-ray sources. The remaining sources do not contain any

bins with TS > 20 and are not analysed further.

Name	Flux > 200 MeV (ph/cm2/s)	dFlux (ph/cm2/s)	Index	± Index	TS
0655.8-0708	1.60E-08	2.96E-09	-3.5	0.1	33.6
1118-61	2.45E-08	1.71E-08	-2.8	0.1	42.5
Ginga_1843-02	5.04E-08	2.91E-08	-2.8	0.1	57.9
J004723.7-731226	3.72E-09	1.34E-09	-2.4	0.1	28.6
J0049.4-7323	4.51E-09	1.36E-09	-2.4	0.1	43.8
J0055.2-7238	4.15E-09	2.80E-09	-2.4	0.1	26.3
J0057.4-7325	4.74E-09	1.95E-09	-2.5	0.1	35.0
J0544.1-7100	8.04E-09	1.71E-09	-2.9	0.1	32.7
J1809.8-1943	4.34E-08	3.77E-08	-2.8	0.1	45.0
J1820.5-1434	4.06E-08	3.79E-08	-2.7	0.1	43.5
J1841.0-0535	1.52E-08	2.66E-09	-2.0	0.1	41.8
J1855-026	2.50E-08	5.72E-09	-5.0	0.1	28.6
J1858+034	2.81E-08	1.92E-08	-2.6	0.1	32.6
J1946+274	2.09E-08	3.63E-09	-5.0	0.4	47.4
KES_73	4.77E-08	4.39E-09	-2.2	0.1	144.6
Sct_X-1	4.62E-08	1.52E-08	-2.5	0.1	78.7
XTE_SMC95	6.01E-09	2.43E-09	-2.5	0.1	44.8

Table 6.1: *Candidate sources from the Radio and X-ray catalogues with TS > 25 when analysed with the full Fermi-LAT data. The full data for each source was split into 20 bins and any source with bins containing TS > 20 are shown in table 6.2 and further analysed. The analysis process used is described in the text.*

Name	Flux (ph/cm2/s)	dFlux (ph/cm2/s)	Index	± Index	TS
1118-615	2.45E-08	1.71E-08	-2.8	0.1	42.5
J1841.0-0535	1.52E-08	2.66E-09	-2.0	0.1	41.8
KES_73	4.77E-08	4.39E-09	-2.2	0.1	144.6

Table 6.2: *Candidate sources from the Radio and X-ray catalogues. These sources all have bins with TS > 20 when analysed with the Fermi-LAT. These sources are of particular interest and further analysed with Fermi. See text for the analysis process used.*

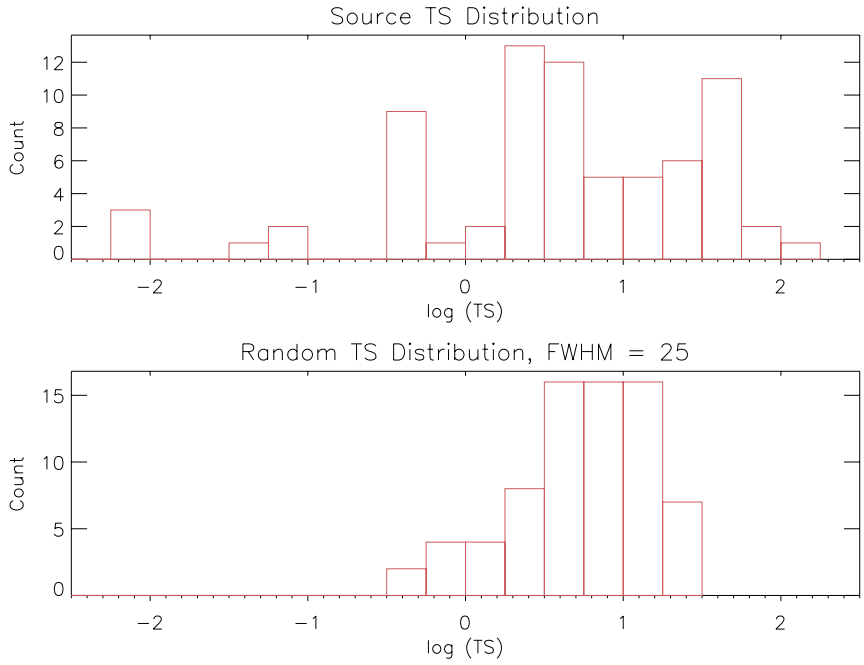

Figure 6.1: *Histogram showing the distribution of the TS statistic for all sources analysed. The vast majority of sources are expected to have low TS values as shown in the figure. Those with TS > 25 are of interest for further analysis.*

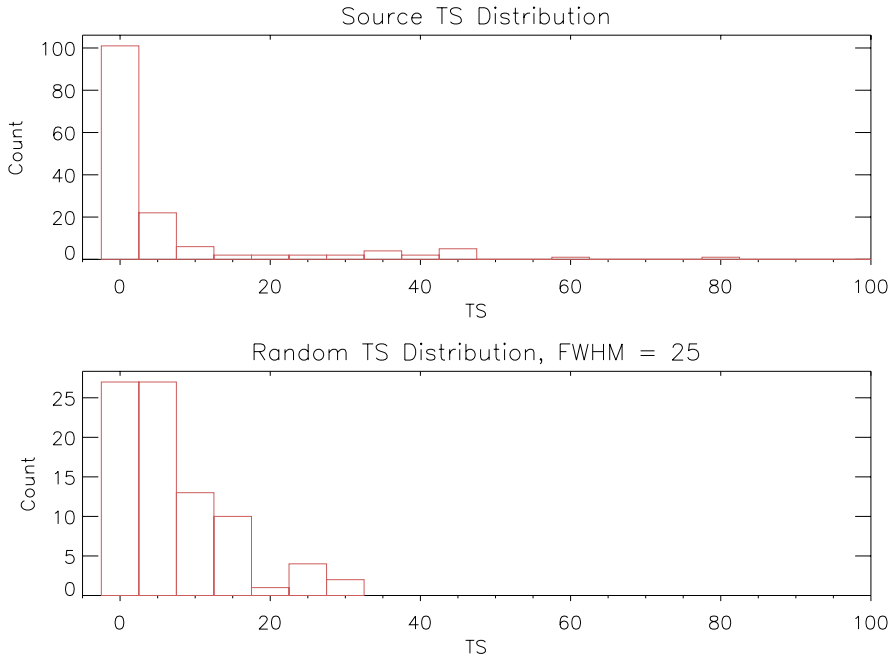

Figure 6.2: *Histogram showing the distribution of the TS statistic for all sources analysed. The vast majority of sources are expected to have low TS values as shown in the figure. Those with TS > 25 are of interest for further analysis.*

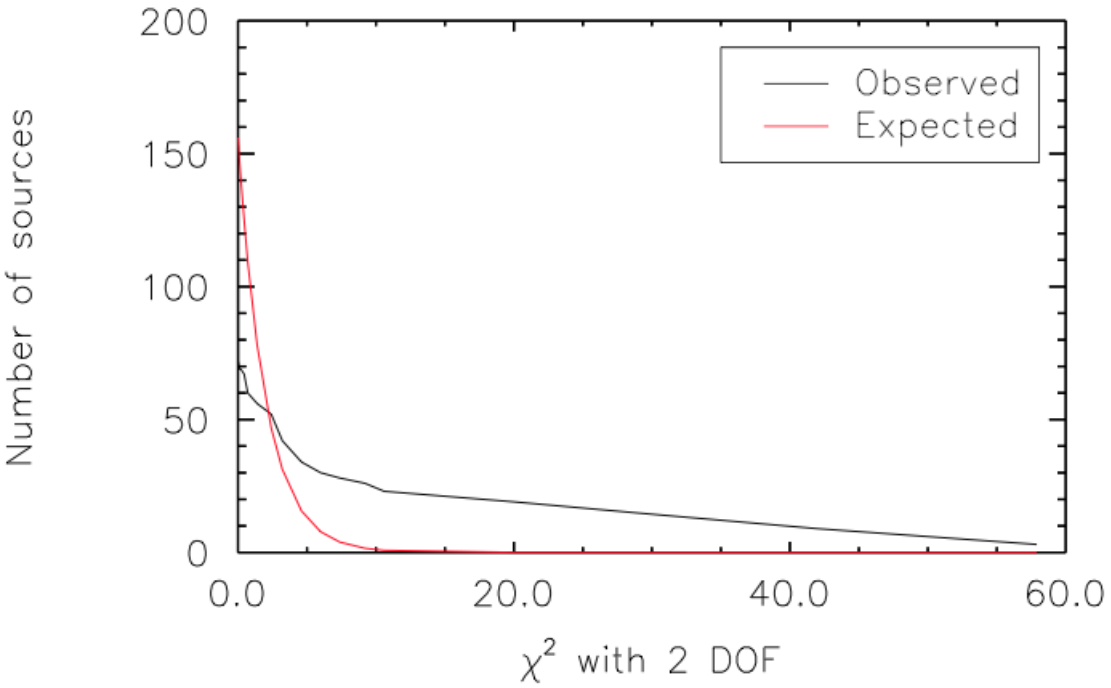

Figure 6.3: *The expected and observed χ^2 cumulative distributions of TS values with 2 degrees of freedom. The expected cumulative distribution of TS values under the null (no extra source) hypothesis falls significantly below the observed distribution.*

6.1 Interesting Candidates

There are 3 sources of interest (shown in Table 6.2), which might contain significant gamma-ray emission. These sources were originally selected from the radio and X-ray binary catalogues discussed at the beginning of this chapter. If there are any correlations between radio or X-ray and gamma-ray activities, these three candidates provide the best opportunity to study them.

6.1.1 1118-615

1118-615 was first discovered with Ariel V in an outburst in 1974 (Eyles *et al.*, 1975) and classified as a hard X-ray transient pulsar. Ives *et al.* (1975) also found X-ray pulsations with a duration of 405.3 ± 0.6 seconds from the same observations. The optical counterpart is classified as a Be star with strong Balmer emission lines suggesting the presence of an extended envelope (Motch *et al.*, 1988). The distance to the source is estimated to be 5 ± 2 kpc (Janot-Pacheco *et al.*, 1981) and the binary orbital period was reported by Staubert *et al.* (2011) as 24 ± 0.4 days.

There have been three outbursts detected so far for this source. The first was detected in 1974 with Ariel V (Maraschi *et al.*, 1976). The second was observed by BATSE in January 1992 (Coe *et al.*, 1994) and lasted for ≈ 30 days with a detection of pulsar period ≈ 406.5 seconds up to 100 keV.

1118-615 remained quiescence until a third outburst was detected on 4 January 2009 by Swift (Mangano, 2009). The pulsations detected by Swift were slightly longer at 407.68 seconds. The outburst was also detected by Rossi X-Ray Timing Explorer (RXTE) and INTEGRAL observed flaring activity in the source ≈ 30 days after the main outburst (Leyder *et al.*, 2009).

The X-ray light curve of 1118-615 between 55200 - 56085 MJD from the MAXI observatory is shown in figure 6.4. The time range was selected between the launch of MAXI and the cut off time for Fermi analysis of 1118-615. There are no obvious periods of flaring from the MAXI observation.

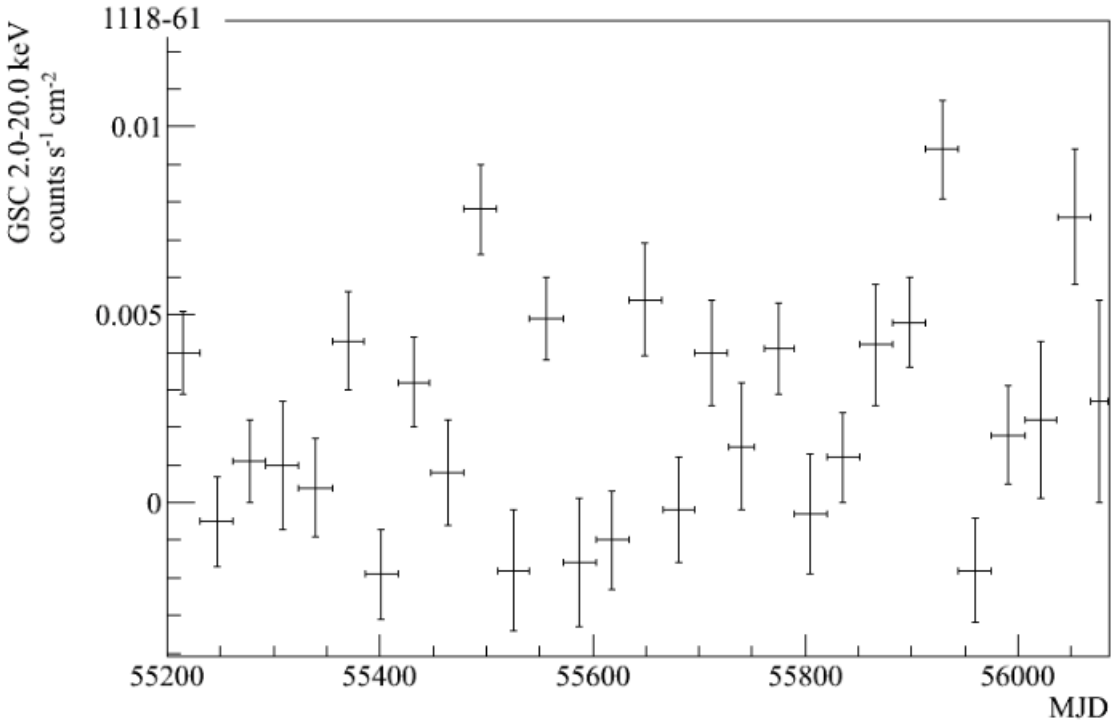

Figure 6.4: *X-ray light curve of 1118-615 from the MAXI observatory. The full time range from MAXI launch (55200 MJD) to the cut off time for Fermi analysis (56085 MJD) is shown. The full energy cut for MAXI is used (2-20 keV). There are no obvious periods of active flaring.*

The Fermi counts map of the source is shown in figure 6.5. The diffuse Galactic emission can be seen clearly. The bright source at RA = 169.7° and DEC = -60.5° is the point source, 2FGL J1118.8-6128, detected by Fermi in the second year catalogue. All sources within 10° of 1118-615, including 2FGL J1118.8-6128, are removed from the analysis. The full Fermi time range (July 2008 to August 2012)

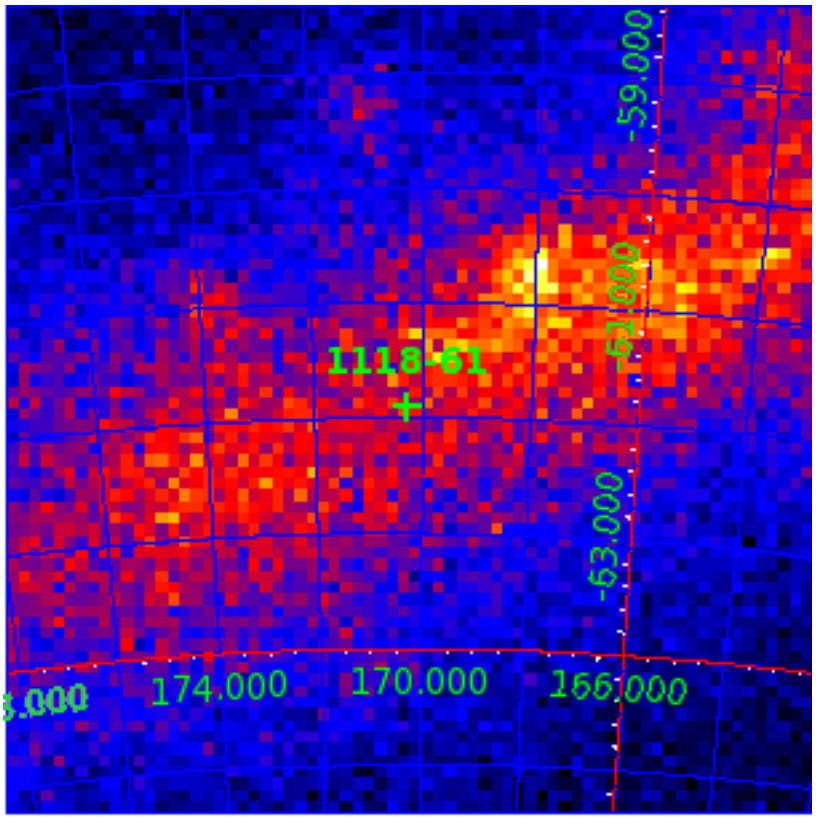

Figure 6.5: *Counts map from Fermi centred on 1118-615. There are approximately 80 photons per pixel at the position of 1118-615. The galactic diffuse emission can easily be seen. The minimum energy threshold for the counts map was set to 200 MeV. The colour scale for the photons per pixel is between 5 (dark blue) to 160 (white).*

was analysed and reveals a TS value of 42.5 (Table 6.2, which corresponds to 6.5σ (section 4.6). The light curve for the full time range split into 20 bins is shown in figure 6.6 with the equivelant TS shown in figure 6.7. There are two bins with TS $>$ 16, which are then split into 4 bins each. The analysis is repeated on the resulting 8 bins with only one bin showing TS $>$ 16 (shown in figure 6.8). Timing analysis (see section 4.3 for details) is then applied to the bin with TS $>$ 16.

There is no known ephemeris of 1118-615 in the Australia Telescope National

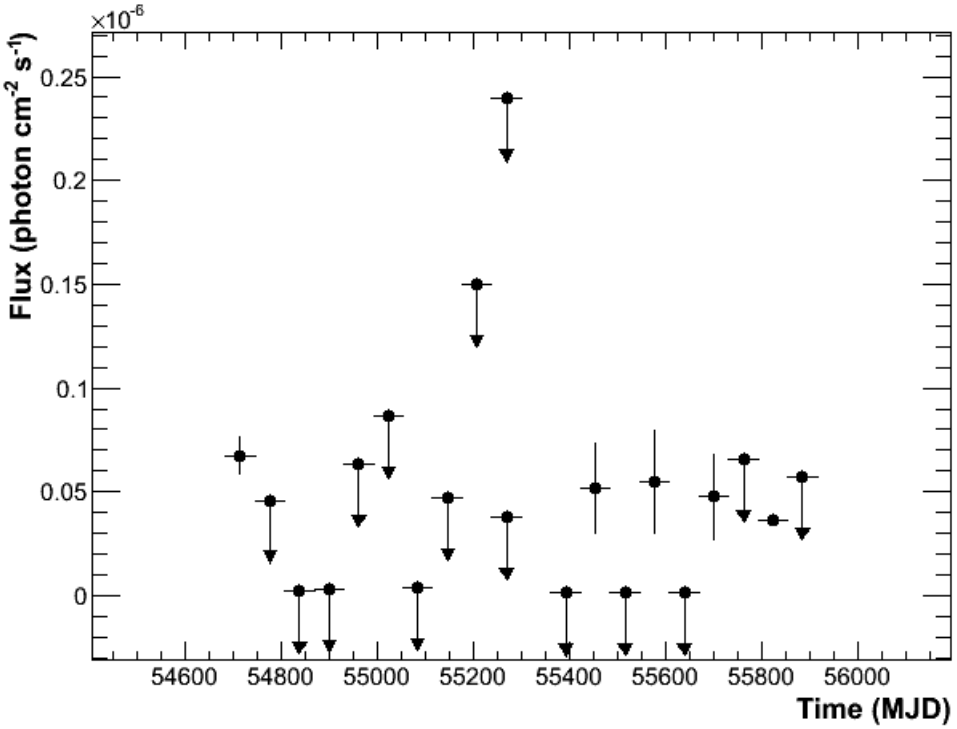

Figure 6.6: *The full Fermi time range (July 2008 to August 2012) gamma-ray flux for 1118-615. The data are split into 20 bins of equal length. Bins with TS < 10 are shown with upper limits. See figure 6.7 for the equivelant TS results.*

Facility (ATNF)[1] database. Therefore, the database was searched for any pulsars within 0.5 degrees of 1118-615 that could be potential sources of the gamma-ray emission. There is only one pulsar that satisfies these conditions: J1119-6127. The ephemeris for this pulsar (shown on Table 6.3) was used for the timing analysis and the results shown in figure 6.9. The highest value for the H-test TS (see section 4.2.3 for details) is 6.5 which corresponds to a $P(H) \sim 0.07$. This is clearly not statistically significant, especially considering the extra trials penalty for selecting the highest value of H-statistic from 10 values spanning different lengths of observation. This result is discussed in chapter 7.

[1] http://www.atnf.csiro.au

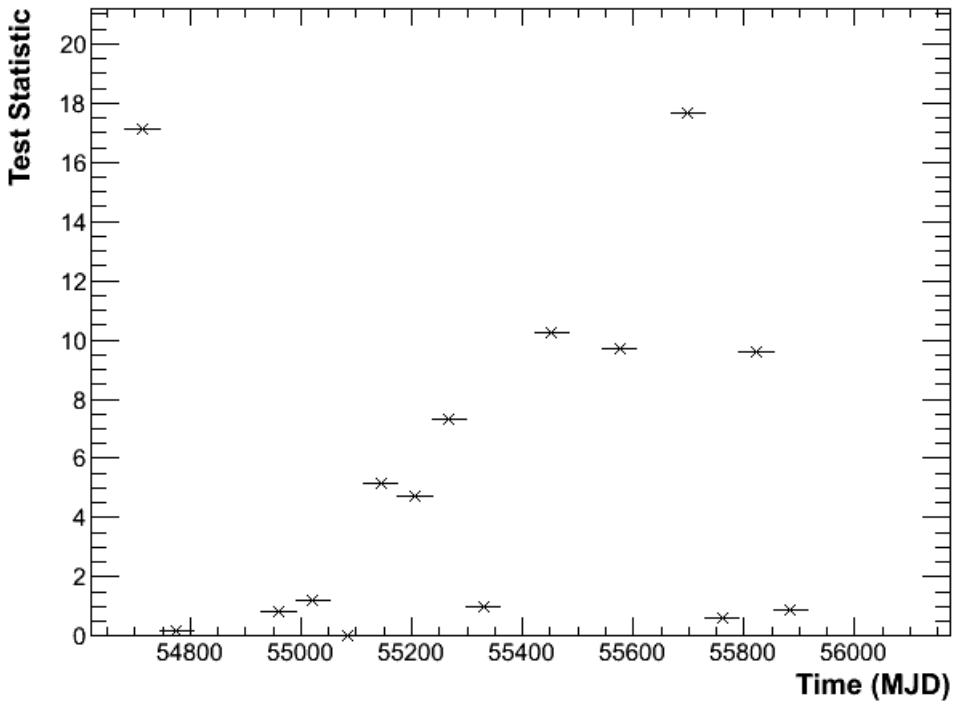

Figure 6.7: *The full Fermi time range (July 2008 to August 2012) TS for 1118-615 split into 20 bins of equal length. Bins with TS > 16 are then split into 4 bins each. See figure 6.6 for the equivelant light curve results.*

Ephemeris for J1119-6127
$T_0 = 54819.992 \pm 0.001$ MJD
$P_0 = 0.40872937 \pm 0.00000005$ s
$\dot{P} = (4.02 \pm 0.04)$ x 10^{-12}

Table 6.3: *Ephemeris for J1119-6127 from Parent et al. (2011), which is used for the timing analysis of 1118-615 shown in figure 6.9.*

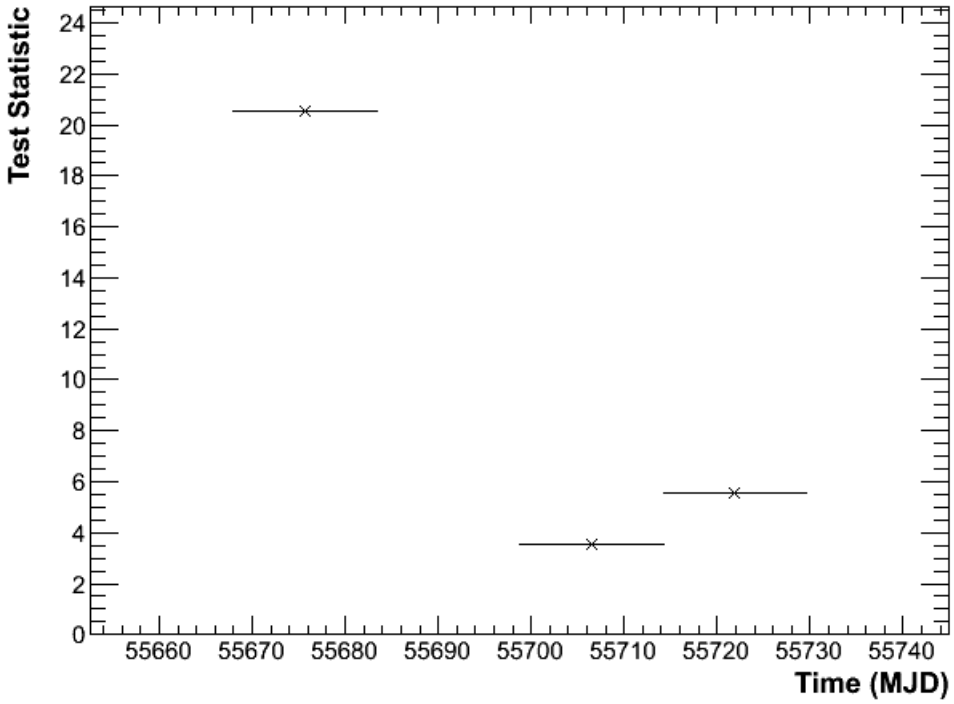

Figure 6.8: *4 bin TS analysis for 1118-615. The second data point is effectively equal to zero and is not shown on the graph. The first bin containing TS ∼ 20 is analysed further in figure 6.9.*

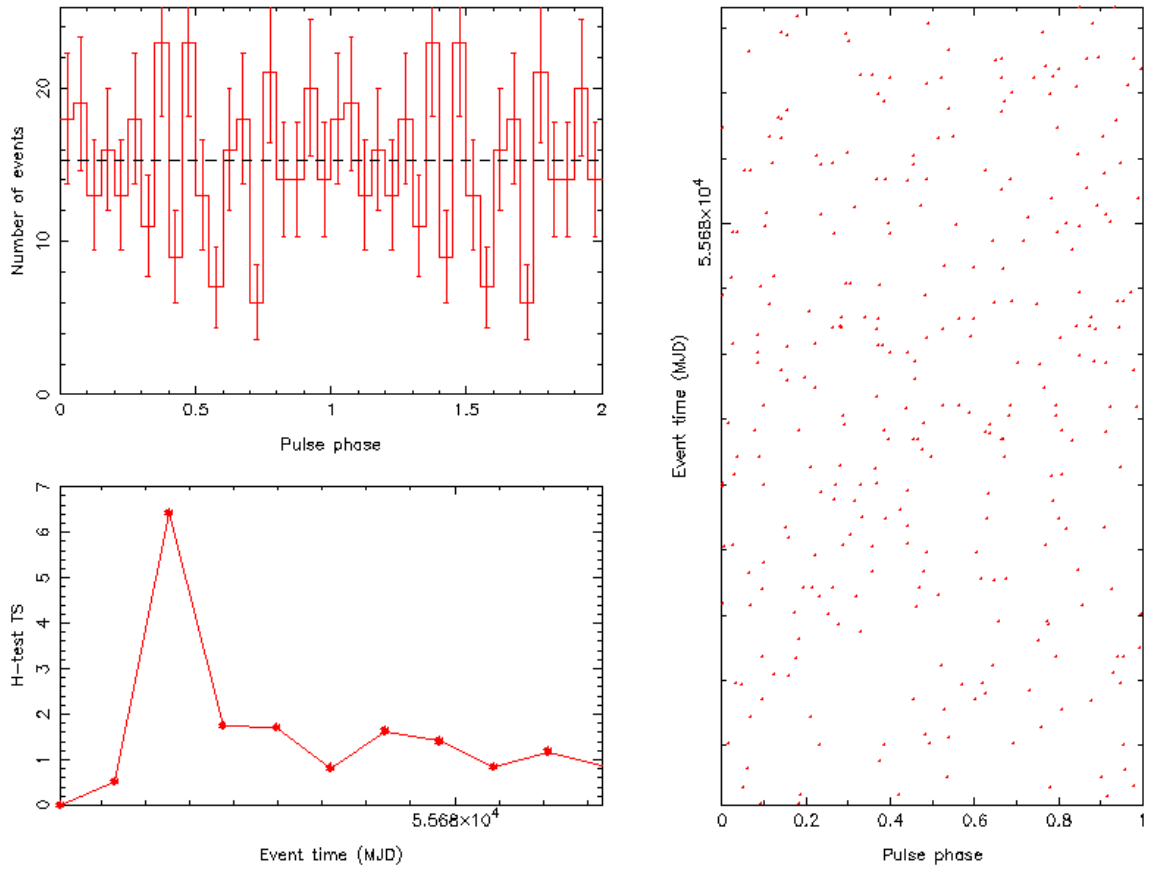

Figure 6.9: *Timing analysis results for J1119-6127 showing the phase folded light curve and H-test TS. The highest H-test TS value is 6.5 which corresponds to a $P(H) \sim 0.07$.*

6.2 J1841.0-0535 and KES 73

J1841.0-0535 and KES 73 are both within the same radius of interest in the Fermi analysis (see figure 6.10) and show high TS values of 41.8 and 144.6, respectively. They are analysed individually but are included here together as the same factors, such as Galactic diffuse emission and Fermi point sources, affect both.

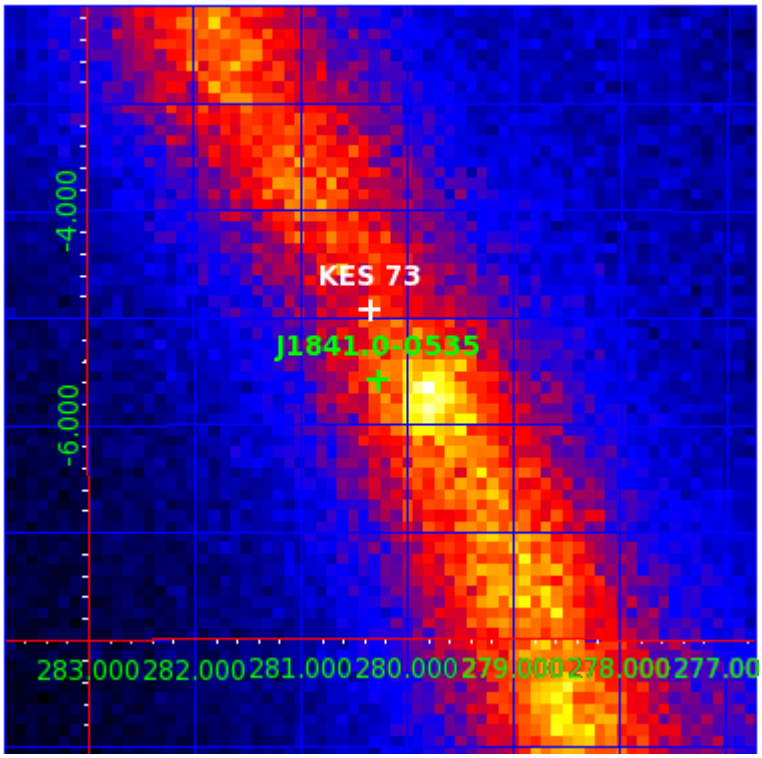

Figure 6.10: *Counts map from the Fermi analysis representing the region with J1841.0-0535 and KES 73. There are approximately 160 and 140 photons per pixel at the positions of J1841.0-0535 and KES 73, respectively. The galactic diffuse emission can easily be seen. The minimum energy threshold for the counts map was set to 200 MeV. The colour scale for the photons per pixel is between 5 (dark blue) to 265 (white).*

6.2.1 J1841.0-0535

J1841.0-0535 (also known as IGR J18410-0535) was discovered by *ASCA* in 1994 as a 4.7 second transient X-ray pulsar. It was detected again in 1999 and in both cases it showed fast X-ray flaring activity with flux changing from $\sim 10^{-12}$ erg cm^{-2} s^{-1} to $\sim 10^{-10}$ erg cm^{-2} s^{-1} within $\sim$ 1 hour (Bamba *et al.*, 2001). There are no more reports of the source in literature until *INTEGRAL* detects three X-ray flares in the 20-80 keV band (two flares in Spring 2003 and one flare in October 2004 (Filippova *et al.*, 2005)). The flares are fast with a duration of a few hours each and peak flux of $\sim 10^{-9}$ erg cm^{-2} s^{-1} (Rodriguez *et al.*, 2004).

A pointed observation of the source with *Chandra* in 2004 detected the source during a non-flaring phase with flux of $\sim$ 4 x 10^{-9} erg cm^{-2} s^{-1} (Halpern *et al.*, 2004). This is likely to represent the quiscent X-ray emission. The companion to J1841.0-0535 was identified as a B1 Ib-type supergiant by Nespoli *et al.* (2008) through infrared spectroscopy, which classifies the system as a Supergiant Fast X-ray transient (Negueruela *et al.*, 2006). There have been no confirmed detections of the source in radio.

The MAXI observatory continuously monitors J1841.0-0535. The X-ray light curve from MAXI between 55200 - 56085 MJD is shown in figure 6.11. The time range was selected between the launch of MAXI and the cut off time for Fermi analysis of J1841.0-0535. There are no detections of active flaring period from the MAXI observation.

J1841.0-0535 is characterized by its striking positional association with the unidentified TeV source HESS J1841-055 (see figure 6.12). J1841.0-0535 is the only X-ray (4-20 keV) and soft gamma-ray (20-100 keV) source detected by *INTEGRAL*

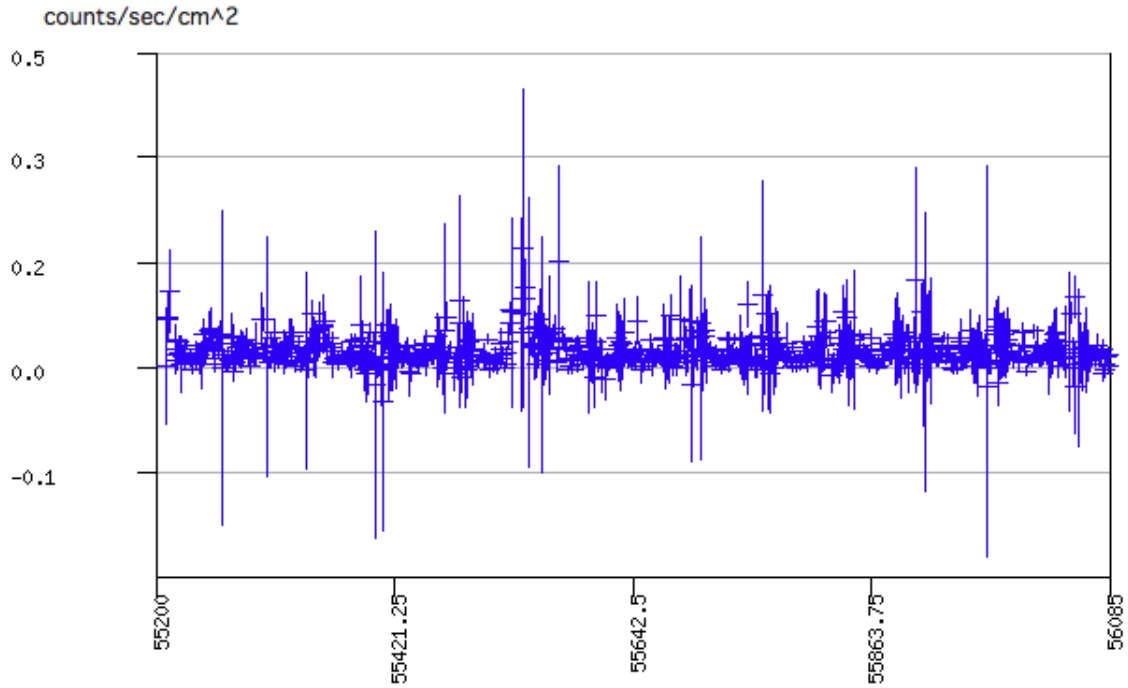

Figure 6.11: *X-ray light curve of J1841.0-0535 from the MAXI observatory. The full time range from MAXI launch (55200 MJD) to the cut off time for Fermi analysis (56085 MJD) is shown. The full energy cut for MAXI is used (2-20 keV). There are no obvious periods of active flaring.*

within the HESS error ellipse of HESS J1841-055 (Sguera *et al.*, 2009). However, the transient X-ray behavior and pointlike nature of J1841.0-0535 do not agree with the extended and non variable TeV emission of HESS J1841-055. Nevertheless, it would be reasonable to postulate that J1841.0-0535 could contribute some fraction of the TeV emission detected for HESS J1841-055 (Sguera *et al.*, 2009).

The Fermi counts map of J1841.0-0535 is shown in figure 6.10. The diffuse gamma-ray emission can be seen as well as the other candidate source in the region: KES 73 (see section 6.2.2 for results). The bright source at RA = 280.3° and DEC = -4.9° is the point source, 2FGL J1841.2-0459c, detected by Fermi in

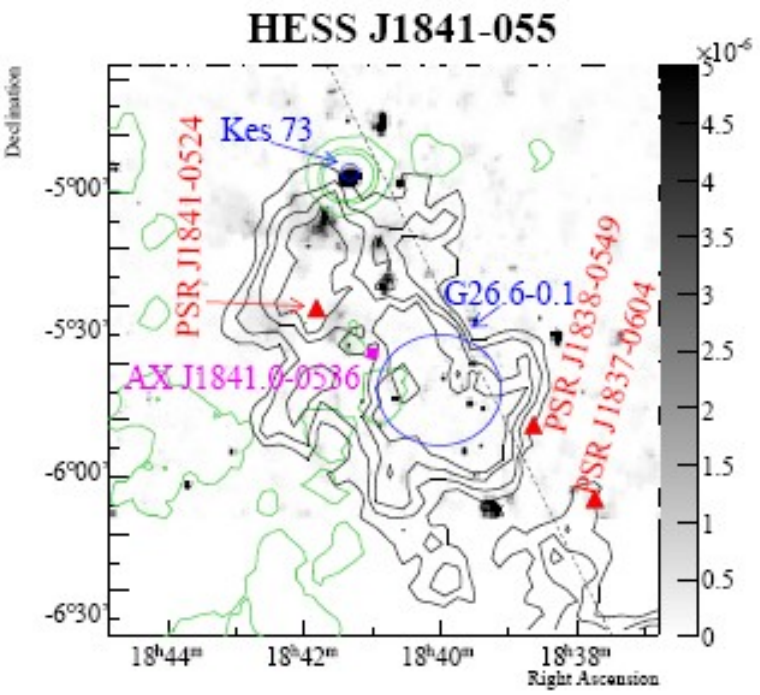

Figure 6.12: *HESS image of the HESS J1841-055 region showing the position of J1841.0-0535, which is the only X-ray (4-20 keV) and soft gamma-ray (20-100 keV) source within the HESS error ellipse. The green adaptively smoothed contours represent X-ray results from ROSAT and are overlaid on the grey-scale radio image. Known positions for SNR Kes 73 (circle), high spin-down pulsars (filled triangles), high mass X-ray binary J1841.0-0536 (purple) and SNR G26.6-01 are also shown. Image from Kosack et al. (2008).*

the second year catalogue. All sources within 10° of J1841.0-0535, including 2FGL J1841.2-0459c, are removed from the analysis. The Fermi data between July 2008 to August 2012 was analysed and revealed a TS value of 41.8 (Table 6.2, which corresponds to $\sim 6.5\sigma$ (section 4.6). The data set was then split into 20 bins with the resulting light curve and TS shown in figures 6.13 and 6.14, respectively. There is only one bin with TS > 16, which is then split into 4 bins with the TS shown in figure 6.15. Timing analysis (see section 4.3 for details) is then applied to the bin with TS > 16.

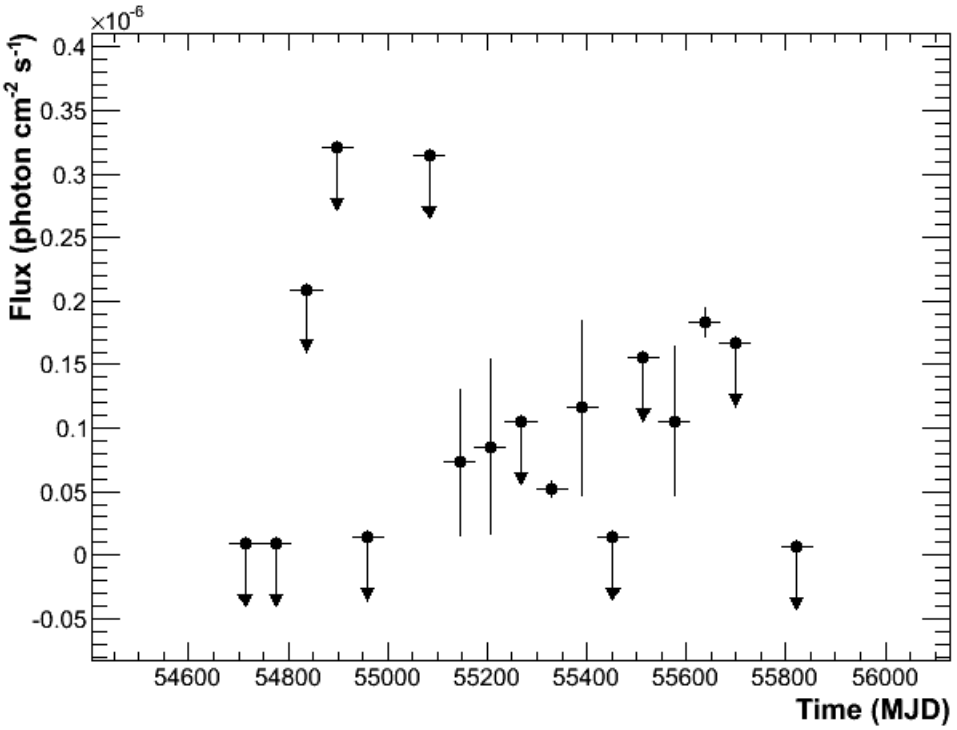

Figure 6.13: *The full Fermi time range (July 2008 to August 2012) gamma-ray flux for J1841.0-0535. The data are split into 20 bins of equal length. Bins with TS < 10 are shown with upper limits. See figure 6.14 for the equivelant TS results*

There is no known ephemeris of J1841.0-0535 in the ATNF database but there is one available for J1841-0524, which is the only pulsar within 0.5 degrees (see figure 6.12). The ephemeris for J1841-0524 (shown on Table 6.4) was used for timing analysis and the results shown in figure 6.16. The highest value for the H-test TS (see section 4.2.3 for details) is 3.8 which corresponds to a $P(H) \sim 0.22$. This is not statistically significant, especially considering the extra trials penalty for selecting the highest value of H-statistic from 10 values spanning different lengths of observation. This result is discussed further in chapter 7.

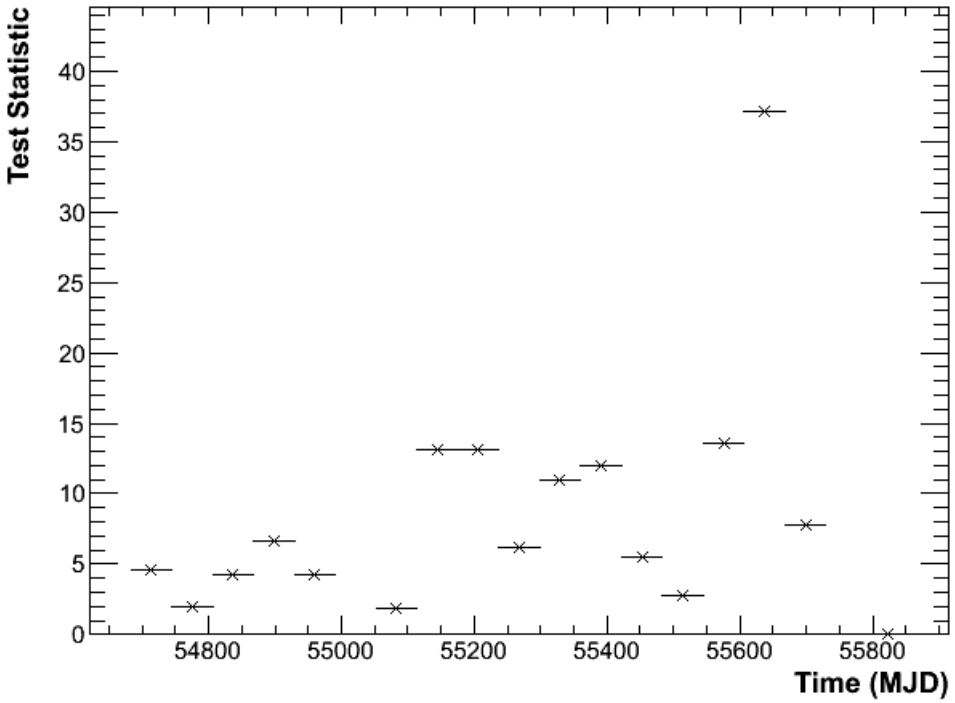

Figure 6.14: *The full Fermi time range (July 2008 to August 2012) TS for J1841.0-0535 split into 20 bins of equal length. Bins with TS > 16 are then split into 4 bins each. See figure 6.13 for the equivelant light curve results*

Ephemeris for J1841-0524
$T_0 = 54743.427 \pm 0.001$ MJD
$P_0 = 0.4457971741 \pm 0.0000000002$ s
$\dot{P} = (2.34 \pm 0.04)$ x 10^{-13}

Table 6.4: *Ephemeris for J1841-0524 from the ATNF database, which is used for the timing analysis of J1841.0-0535 shown in figure 6.16.*

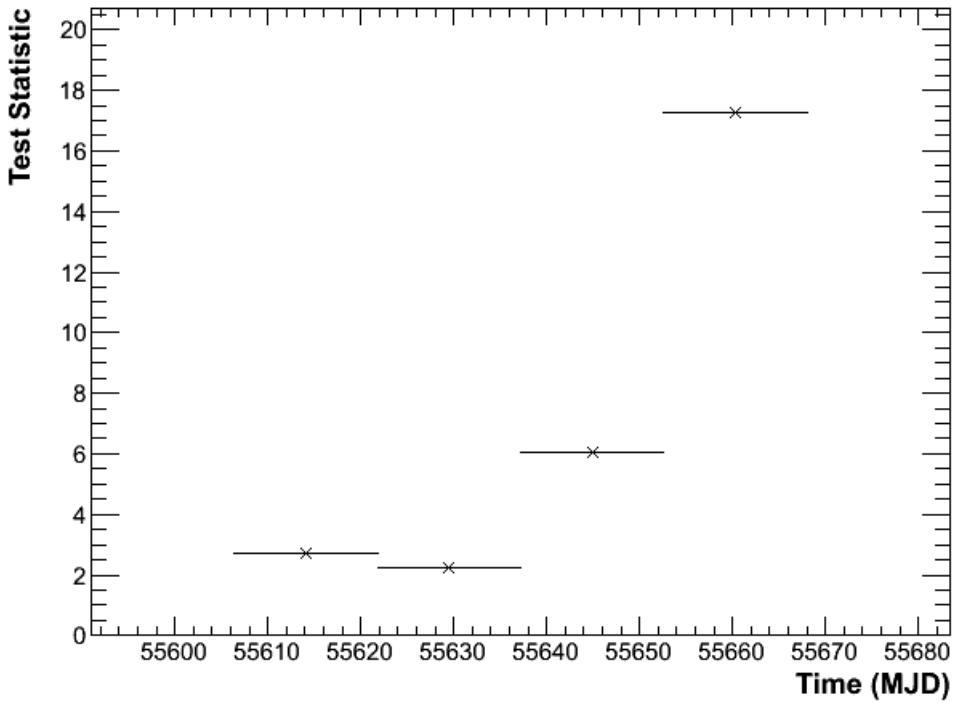

Figure 6.15: *4 bin TS analysis for J1841.0-0535. The fourth bin containing TS ∼ 17.5 is analysed further in figure 6.16.*

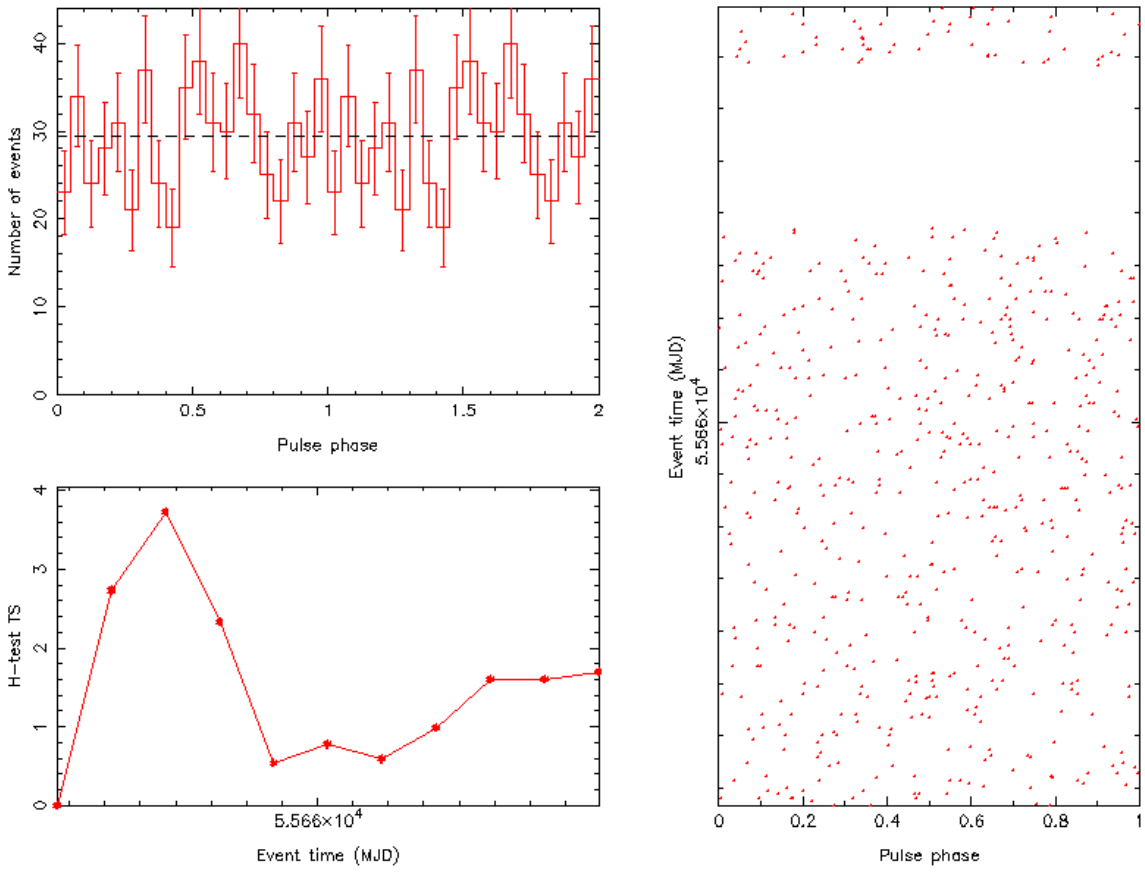

Figure 6.16: *Timing analysis results for J1841.0-0535 showing the phase folded light curve and H-test TS. The highest H-test TS value is 3.8 which corresponds to a* $P(H) \sim 0.22$.

6.2.2 KES 73

KES 73 is a small ($\sim 4'$ diameter) supernova remnant. However, we are interested in the power source of the supernova remnant: the anomalous X-ray pulsar J1841.3-0455 located at the centre. Anomalous X-ray pulsars are rare sources closely concentrated along the Galactic plane (see Kaspi (2007) for a review). They are characterized by X-ray luminosities ($\sim 10^{33}$ - 10^{35} erg s^{-1}) that are orders of magnitude too high to be explained by rotational energy release of spin-down.

J1841.3-0455 is stable with no flaring activity detected in over 20 years of observations (Kaspi, 2007). J1841.3-0455 is continuously monitored by the MAXI X-ray observatory and the light curve between 55200 - 56085 MJD is shown in figure 6.17. There are no flaring activity in the X-ray light curve. J1841.3-0455 is within the 95% error circle of unidentified EGRET source 3EG J1837-0423. However, physical association is ruled out by Kaspi (2007) and Sguera *et al.* (2009) who studied the X-ray and soft gamma-ray behaviours of both sources. There have been no confirmed detections of J1841.3-0455 in radio.

The counts map of the source and its surrounding region is shown in figure 6.10. The Galactic diffuse emission can be seen clearly as well as the other candidate source in the region: J1841.0-0535 (see section 6.2.1 for results). The TS for the Fermi full time range (July 2008 to August 2012) is 144.6 which corresponds to 12σ (Table 6.2). The full time light curve with 20 bins is shown in figure 6.18 with the equivelant TS shown in figure 6.19. There are three bins with TS $>$ 16, which are analysed with 4 bins each. Of the resulting 12 bins, only one contains TS $>$ 16 (shown in figure 6.20). That bin is then analysed using the method described in section 4.3.

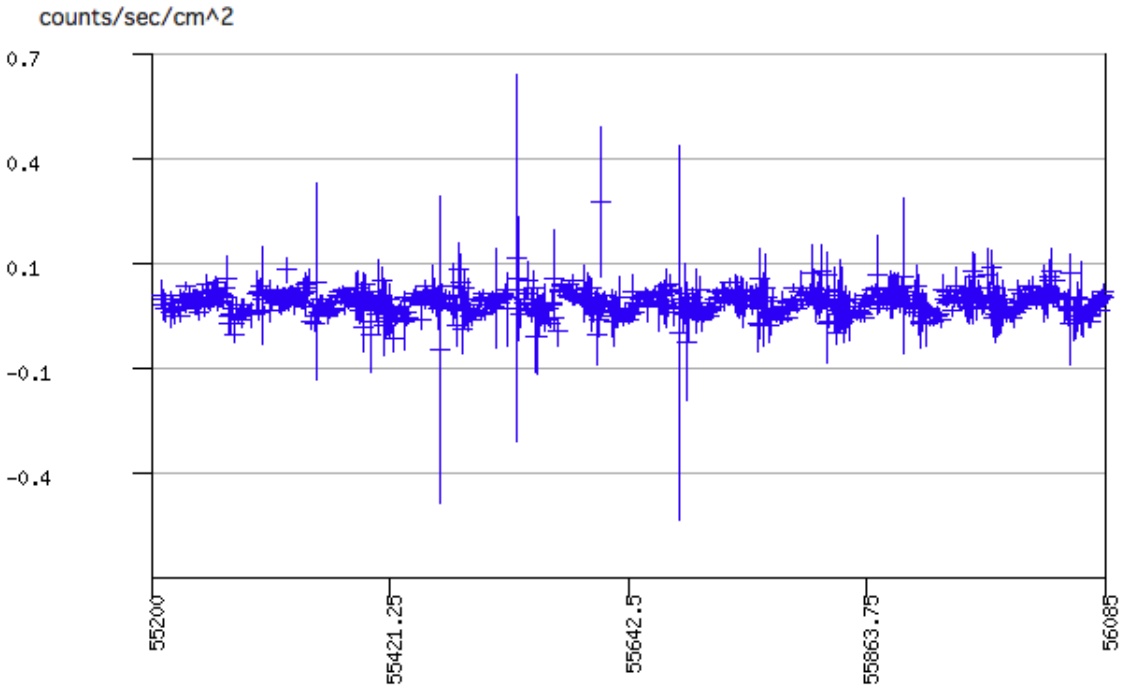

Figure 6.17: *X-ray light curve of J1841.3-0455 from the MAXI observatory. The full time range from MAXI launch (55200 MJD) to the cut off time for Fermi analysis (56085 MJD) is shown. The full energy cut for MAXI is used (2-20 keV). There are no obvious periods of active flaring.*

The ephemeris for J1841.3-0455 (shown on Table 6.5) was extracted from the ATNF database. The results from the timing analysis is shown in figure 6.21. The highest value for the H-test TS (section 4.2.3) is 6 which corresponds to a $P(H) \sim 0.09$. Similar to the result for 1118-615 (section 6.1.1), this is also not statistically significant, especially considering the extra trials penalty for selecting the highest value of H-statistic from 10 values spanning different lengths of observation.

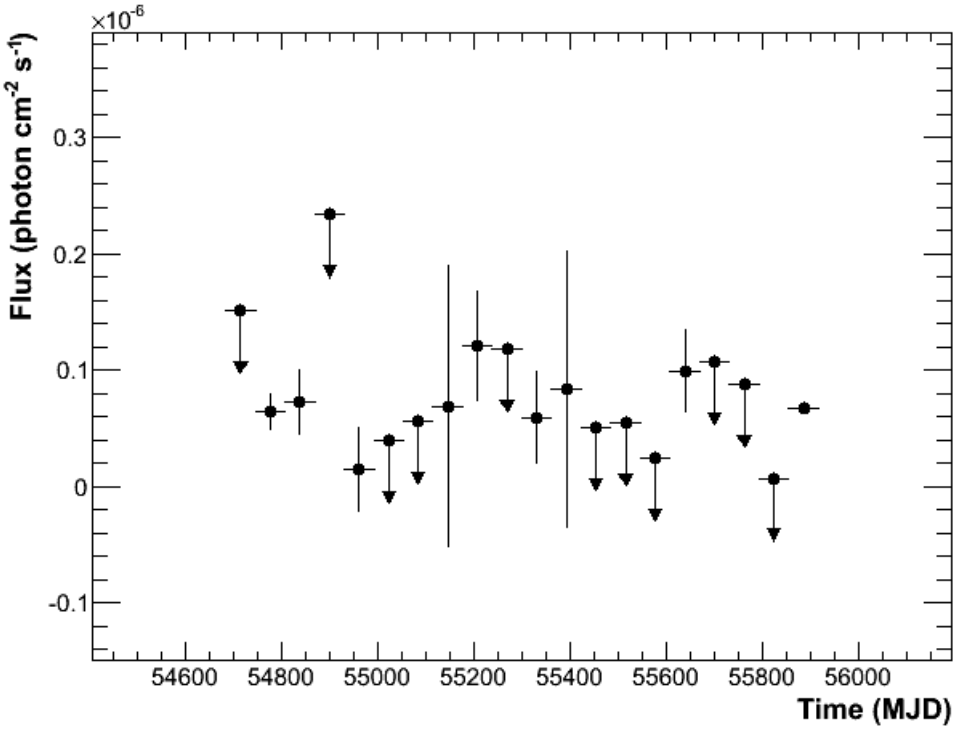

Figure 6.18: *The full Fermi time range (July 2008 to August 2012) gamma-ray flux for KES 73. The data are split into 20 bins of equal length. Bins with TS < 10 are shown with upper limits. See figure 6.19 for the equivelant TS results*

Ephemeris for J1841-0524
$T_0 = 54775.032 \pm 0.001$ MJD
$P_0 = 11.7789433 \pm 0.0000005$ s
$\dot{P} = (4.47 \pm 0.03)$ x 10^{-11}

Table 6.5: *Ephemeris for J1841.3-0455 from the ATNF database, which is used for the timing analysis shown in figure 6.21.*

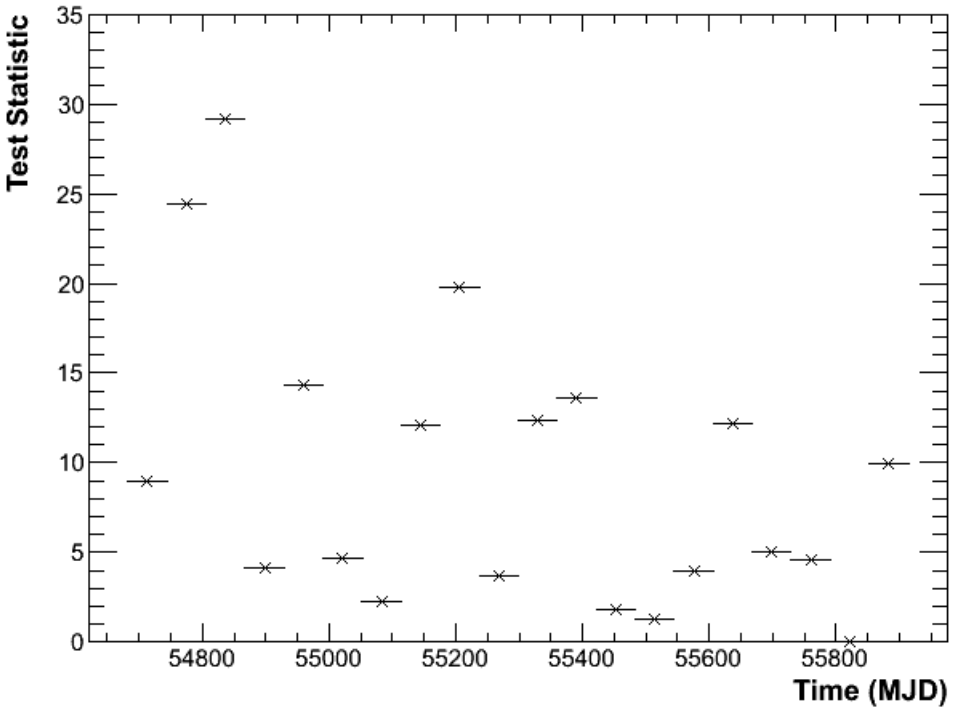

Figure 6.19: *The full Fermi time range (July 2008 to August 2012) TS for KES 73 split into 20 bins of equal length. Bins with TS > 16 are then split into 4 bins each. See figure 6.18 for the equivelant light curve results*

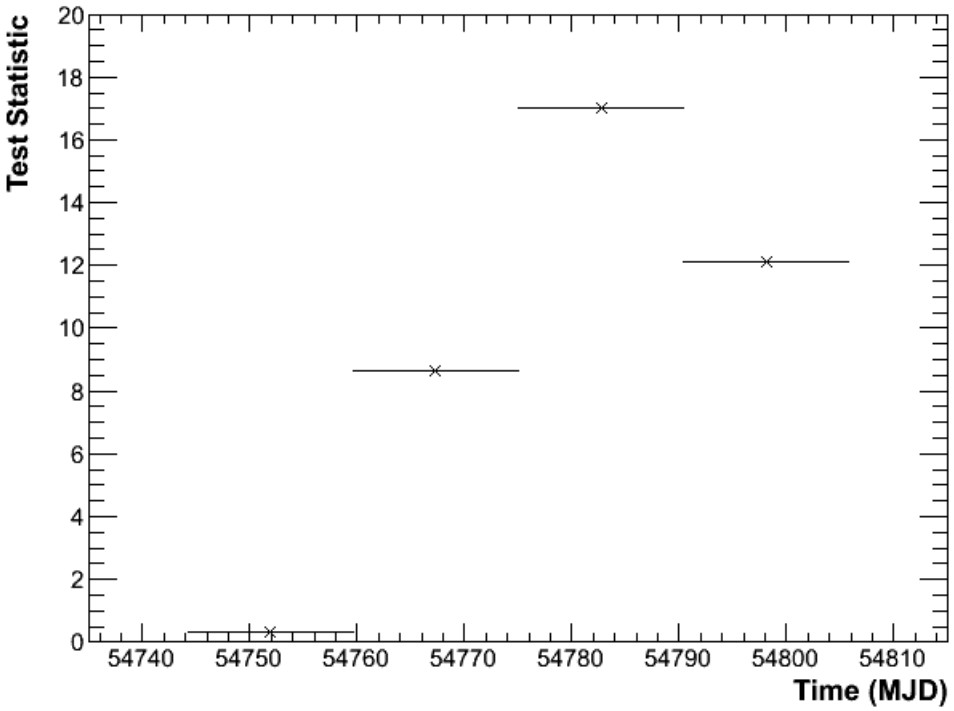

Figure 6.20: *4 bin TS analysis for KES 73. The third bin containing TS ∼ 17 is analysed further in figure 6.21.*

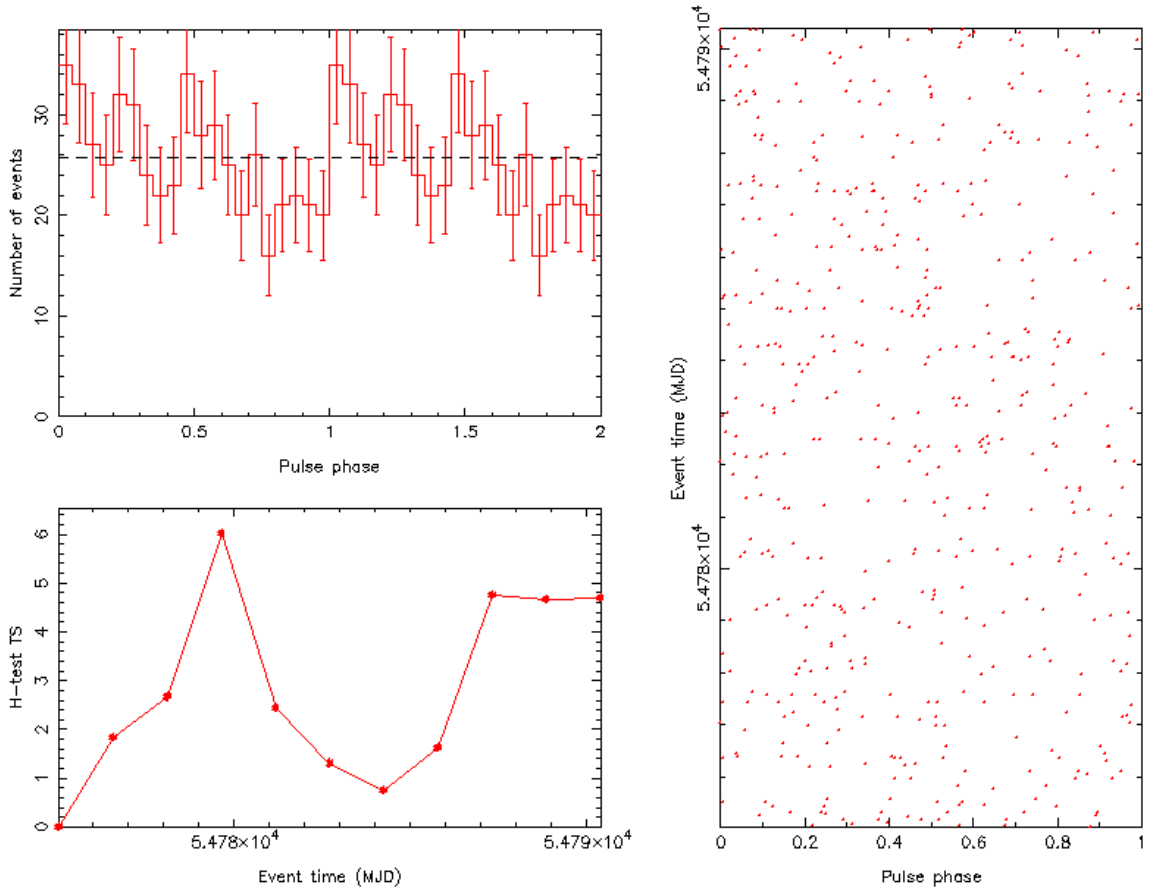

Figure 6.21: *Timing analysis results for J1841.3-0455 showing the phase folded light curve and H-test TS. The highest H-test TS value is 6 which corresponds to a $P(H) \sim 0.09$.*

Chapter 7

Discussion and Conclusion

There is no celestial object which is hot enough to emit, thermally, photons in the high energy gamma-ray range. Hence, gamma-rays must be produced in extreme non-thermal processes. These radiative emission mechanisms include synchrotron and inverse-Compton processes. Common to most gamma-ray emission mechanisms is the requirement of a population of particles at TeV energies (Weekes, 2003). One of the mechanism for acceleration of particles to these high energies is via the shocks within collimated jets. Another mechanism is the interaction between the relativistic winds of particles produced by pulsars and the stellar wind of the companion star.

Binary systems containing compact objects, such as a neutron star or a black hole of up to a few solar masses, and a companion star can be important astronomical particle accelerators. They contain violent environments with high magnetic fields and stellar winds that operate under a varying, but often regularly repeating, set of environmental conditions. Throughout the orbit of the binary system, matter and photon field densities are continually changing. Observations

of gamma-ray binary systems provide repeatable and stringent tests for models of particle acceleration and high energy emission mechanisms (Dubus, 2007).

The sources analysed in this thesis contain interesting properties that could lead to the production of gamma-rays. For example, gamma-ray emission might be detectable if the electrons responsible for the strong radio outbursts in Cygnus X-3 are accelerated to high enough energies. In the case of PSR B1259-63, the situation is complicated as there are two models. In the hadronic model, the emission is caused by the collisions of high energy protons accelerated by the pulsar wind and the circumstellar disc (Neronov & Chernyakova, 2007). The emission could also be explained by the inverse Compton (IC) scattering of ultra-relativistic electrons accelerated at the pulsar wind termination shock (Khangulyan *et al.*, 2007). For Circinus X-1, the presence of superluminal jets during flaring periods provides strong evidence of particle acceleration.

There are two groups of sources analysed in this thesis. The first group focused on likely candidates and includes firm detections of Cygnus X-3 and PSR B1259-63. The second group focused on interesting candidates from two catalogues containing radio and X-ray binary systems.

7.1 Sources of Interest

7.1.1 Circinus X-1

The analysis of Fermi observations of Cir X-1 focused on the 16.6 day orbital period of the system, which has been clearly observed in radio, infra-red and optical. The system is known to be a transient X-ray source with periods of flaring separated by months of no activity. These periods of flaring peaks are separated by 16.6

days in line with the orbital periodicity of Cir X-1.

The Fermi data was split into two 180 day timespans with one covering an active flaring period of Cir X-1 and the other containing data from a quiescent timespan. Corresponding data from MAXI was used to analyse for any cross correlation between the gamma-rays and X-rays. The results of the cross correlation during the active flaring period show only a hint of small correlations at approximately $\sim \pm$ 15 days. The correlation is not statistically significant however - with a chance probability of $\sim$23%, and so cannot be definitvely associated with the Cir X-1 period of 16.6 days. The analysis is complicated by the Fermi satellite precession period having a third harmonic at approximately 17 days. However, analysis of the non-active timespan contain no evidence for either the Cir X-1 orbital period or for a cross correlation with the X-ray data.

The Lomb-Scargle power spectral technique was used to search for the 16.6 day periodicity of Cir X-1. Full Fermi timespan data centred on Cir X-1 and approximately 9^o away were analysed and showed no evidence of the 16.6 day periodicity. This result is not surprising as the Fermi satellite precession period of approximately 52 days and its harmonics are the dominent features. However, the active flaring timespan periodogram shows the position of the 16.6 day period of Cir X-1, with a significance of 96% (i.e. a probability of occurrence by chance of 4%). This is not sufficiently high to claim detection.

The jet in Cir X-1 is believed to be beamed at us making the system a good candidate for gamma-ray observations. The X-ray active flaring period analysed in this thesis provided the best opportunity to study the source with Fermi. Calvelo *et al.* (2010) observed the flaring period with ATCA and found the strongest radio emission (60 $\pm$20 mJy at 5 GHz and 80 $\pm$20 mJy at 8 GHz) observed ever from

Cir X-1 by ATCA over nearly fifteen years, an order of magnitude stronger than when ATCA observations in 1998-2000 appeared to reveal an ultrarelativistic flow (Fender *et al.*, 2004). A detection with Fermi would constrain the physics involved in the superluminal jet.

7.1.2 Cygnus X-3

The Cygnus X-3 region is challenging to analyse with Fermi as it contains three known bright gamma-ray pulsars combined with high levels of diffuse emission. In fact, PSR J2032+4127 is within 0.5 degrees of Cygnus X-3 and contributes significantly to the Fermi observation of Cygnus X-3. Therefore, detection of Cygnus X-3 with Fermi cannot be claimed solely on spatial association.

The pulsar gating technique described in section 4.5 is used to reduce the contribution of the pulsar to the Fermi data on Cygnus X-3. Approximately 80% of the photons from Cygnus X-3 can be preserved and analysed using this technique making it particularly valuable for regions with several gamma-ray emitters and source confusion.

The Cygnus X-3 orbital period of 4.8 hours is firmly detected during an active flaring period. The full Fermi timespan, with pulsar gating, shows no features that identify the source as being Cygnus X-3. The results suggest that Cygnus X-3 is detectable up to X-ray energetics when not flaring and up to GeV when going through an active phase. The system has not been detected at TeV, at least in the newer generation of Cherenkov telescopes.

The Fermi light curve has an asymmetric shape with a slow rise and faster decay. The Fermi maximum is in phase with the X-ray maximum, which suggests that the emission mechanisms are closely connected. The Fermi detection is com-

patible with the extrapolation of the hard X-ray tail observed up to several 100 keV by Hjalmarsdotter *et al.* (2009). The gamma-ray emission could be explained by the inverse Compton scattering of ultraviolet photons from the Wolf Rayet companion star off of high energy electrons. The limit to this scenario is that the accretion disc and the emission region cannot be close as the gamma-ray emission would be absorbed via the pair production on the soft X-ray photons from the accretion disc.

From the perspective of Fermi, the peak in gamma-ray detection (assuming the dominant gamma-ray production mechanism is inverse Compton scattering) would occur during the time of superior conjunction when the electrons are behind the Wolf Rayet companion star resulting in head-on collisions with the ultraviolet photons. The X-ray peak corresponds to the gamma-ray emission maximum, which suggests that the X-ray modulation is produced via the Compton scattering in the Wolf Rayet companion star.

Cygnus X-3 was only detected between 8 June to 2 August 2009 (MJD 54990 - 55045), which was an active flaring period. Further analysis of Cygnus X-3 after that period would be useful in developing a better understanding of the system.

7.1.3 PSR B1259-63

The analysis of Fermi observations of PSR B1259-63 spanning 90 days between 15th November 2010 and 15th March 2011 is shown in section 5.3. The source was detected simultaneously with Tam *et al.* (2010) on the 21st of November 2010. There was also increased X-ray activity detected with Swift. However, the Fermi flux from PSR B1259-63 decreased after the 21st of November 2010 and was below the detection level of Fermi until another short and relatively weak detection in

the middle of December 2010.

The first 60 days of the Fermi analysis, including the periastron on 15th December 2010, show little activity. However, the last 30 days (between 15th January and 15th February 2011) show detection of the source at $\sim 5\sigma$. The spectral index softens from 1.7-2.3 during the brightening to a peak of ≈ 4 at the flare. The index then hardens for the rest of the flare period.

The multiwavelength emission from PSR B1259-63 is believed to be produced via the interaction of the pulsar wind with the companion star stellar wind. The emission from the system has been observed in radio, X-ray and TeV gamma-rays so a detection in the GeV band was not a surprise. However, the emission detected by Fermi reveals interesting features that have not been detected at other wavelengths. The flare observed approximately 15 days after the periastron was only found with Fermi and not at other wavelengths. Furthermore, the flare continued to be observed even after the neutron star passage through the equatorial wind of the companion star.

The flare also revealed an efficient conversion of the pulsar spin down power into gamma-rays (see the spectral energy distribution in Figure 7.1). The highest single day average flux was $\sim$ 3.6 x 10^{-6} cm^{-2} s^{-1}, which corresponds to an isotropic gamma-ray luminosity of $\sim$ 8.2 x 10^{35} erg s^{-1} at a distance of 2.3 kpc. This is similar to the estimated total pulsar spin down luminosity of $\simeq$ 8.3 x 10^{35} erg s^{-1} (Johnston *et al.*, 1992).

During the flare, there is a correlation between gamma-ray flux and spectral index as shown in Figure 7.2. This can be explained by a leptonic model where the photons are Doppler boosted to higher energies and the observed synchrotron flux is amplified (Dubus & Cerutti, 2013). However, the inverse Compton component

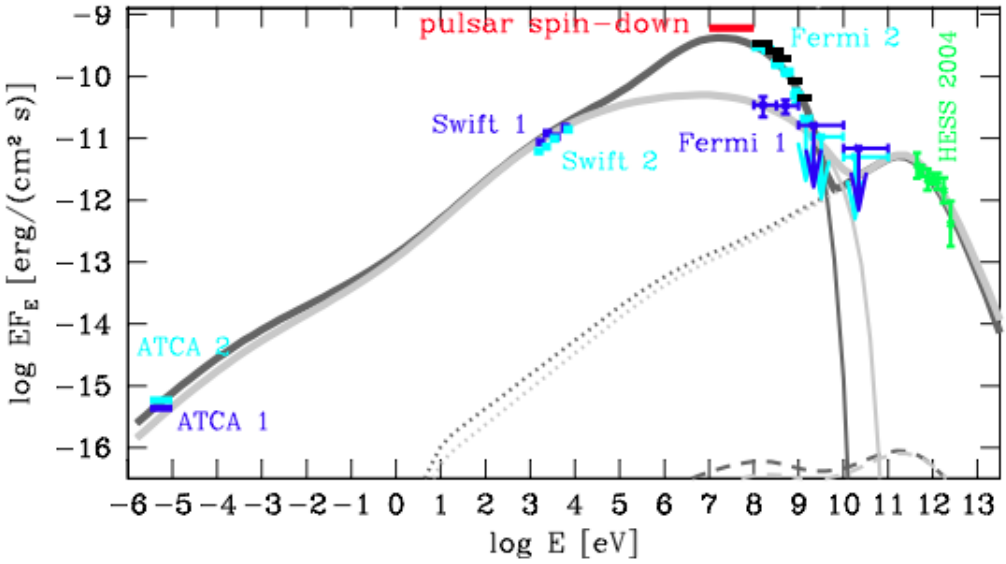

Figure 7.1: *Spectral energy distribution of PSR B1259-63 during periastron. Blue and cyan points represent the measurements of the spectra in the pre- and post- periastron periods by the Fermi Collaboration in gamma-rays, Swift in X-rays and ATCA in radio. The black points represent the results presented in this thesis for the post periastron flare. The dotted, dashed and thin solid lines represent the inverse Compton, Bremsstrahlung and synchrotron components, respectively. The dark grey curves represent the models of the post-periastron flare and the light grey curves show the pre-periastron emission models. The green points are the HESS observations from HESS Collaboration (2005a). The solid red mark is the predicted flux which would be produced given 100 % of the pulsar spin-down power were converted into electromagnetic emission. Figure from Abdo* et al. *(2011).*

of the photon flux is not amplified as much due to the increased scatters between particles and incident photons (Tam *et al.*, 2011). Therefore, the energy flux of the synchrotron emission is higher than the inverse Compton radiation resulting in a spectrum dominated by the high energy tail of the synchrotron emission. The end result is the steep spectrum ($\sim$ -3) shown in Figure 7.2.

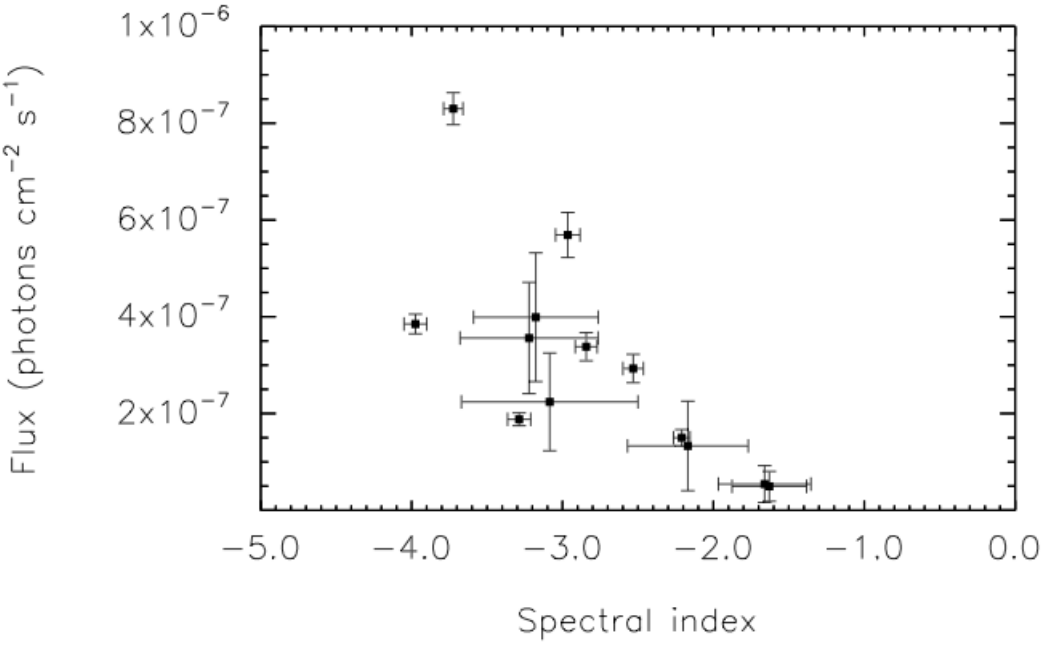

Figure 7.2: *Photon flux versus photon index during the flare of PSRB1259 as discussed in the text. The steep spectrum (∼ -3) can be explained by the high energy tail of the synchrotron emission.*

7.2 Catalogue Sources

The non-catalogue "of interest" sources examined by an overall likelihood in Chapters 5 and a small set of catalogue sources of Chapter 6 were also examined for time variability and, where possible, periodicity. Normally, if two (or more) independent statistical tests are performed on a data set, then the overall detection confidence - quoted as the probability of obtaining such test values by chance, can be evaluated (see Eadie *et al.* (1971), for example) as :

$$P_{\rm overall} = P_1 P_2 (1 - \ln(P_1 P_2)) \tag{7.1}$$

Where P_1 and P_2 are the chance probabilities for tests 1 and 2, respectively. This is substantially more conservative than the naïve simple product: $P_{overall} \sim P_1 P_2$. The second expression grossly overestimates the combined significance (typically by a factor of at least 10, when P_1 and P_2 are both moderate, say 1% each). The reason is that the second expression only determines the probability of obtaining P_1 and P_2, but usually we would be just as interested if, say, P_1 were less but P_2 were more, so that the product was the same. We are thus interested in the probability of getting a value of $P_1 P_2$ from whatever the distributions of P_1 and P_2; this represents the area under the hyperbola given by $P_1 P_2$ = a constant. The first expression yields that area.

For the results of Chapter 5 and 6, we cannot combine any statistical significance obtained from the overall likelihood with any values obtained from high TS values when the data are split into 20, and thence 4 timespan bins, as the two tests are clearly not independent. In addition, we discussed in Chapter 6 how the statistical behaviour of the overall cumulative TS distribution is not reliably

expected to follow the asymptotic χ^2 distribution. To be conservative therefore, we make no attempt to combine any original statistical evidence from the overall TS value with that from variability tests.

A second complication when trying to assess overall detection significance is that a considerable number of trials must be accounted for. If N independent data sets are examined and one is found to have a chance probability of P, then the overall chance probability of observing one such set from N (trials) is :

$$P_{\text{after trials}} = 1 - (1 - P)^N \tag{7.2}$$

With 156 sources examined and 20 timespan bins, 3 of which are split into 4 timespan bins the number of trials for the most significant short timespan TS (for source 1118-61, TS value 20.5) is approximately 240. If the TS value can be relied on statistically (which is in doubt for the reasons described above) then the most significant result from variability would have a chance probability level of 1.1%. This is not sufficiently high to claim detection.

The probability obtained from a short timespan TS value may be combined with any statistical evidence provided by, for example, the H-test for variability, as the tests are independent - so equation 7.2 could be used. Unfortunately, none of the H-test values for periodicity for the catalogue sources are significant, especially considering the trials in choosing the highest H-test value from 10 time ranges. The highest H-test from the catalogue sources is 0.07 from 1118-61, which has a chance probability of 48% (using equation 7.2) and a combined probability of 3.3% (using equation 7.1). Thus, we fail to detect any evidence for variability of periodicity in any of the catalogue sources examined.

Further information could also be gained by stacking analysis of the catalogue sources. Although most sources are in typically dense regions, a stacking analysis could show any underlying astrophysical processes.

7.3 Comparison with Known Sources

The interesting candidates discussed in section 6.1 are compared with known Fermi gamma-ray sources and the results shown in Figure 7.3. All the gamma-ray luminosities assume isotropic emission. The sources with the triangles represent those with gamma-ray upper limits. With the exception of Cygnus X-3, the gamma-ray luminosities of known Fermi sources are the same order of or larger than their X-ray luminosities. Cygnus X-3 is also the only known Fermi source on the plot that is only detected during flaring. The other sources, including PSR B1259-63, are detected either throughout their orbit or part of it.

Candidate sources 1118-61 and J1841.0-0535 are both close to the $L_\gamma = 10^{-2}\ L_x$ line suggesting that their upper limits on gamma-ray luminosities are less than 10^{-2} of their X-ray luminosities. Interestingly, KES 73 is in the vicinity of the known Fermi gamma-ray sources and could be a good candidate for further analysis with more Fermi data.

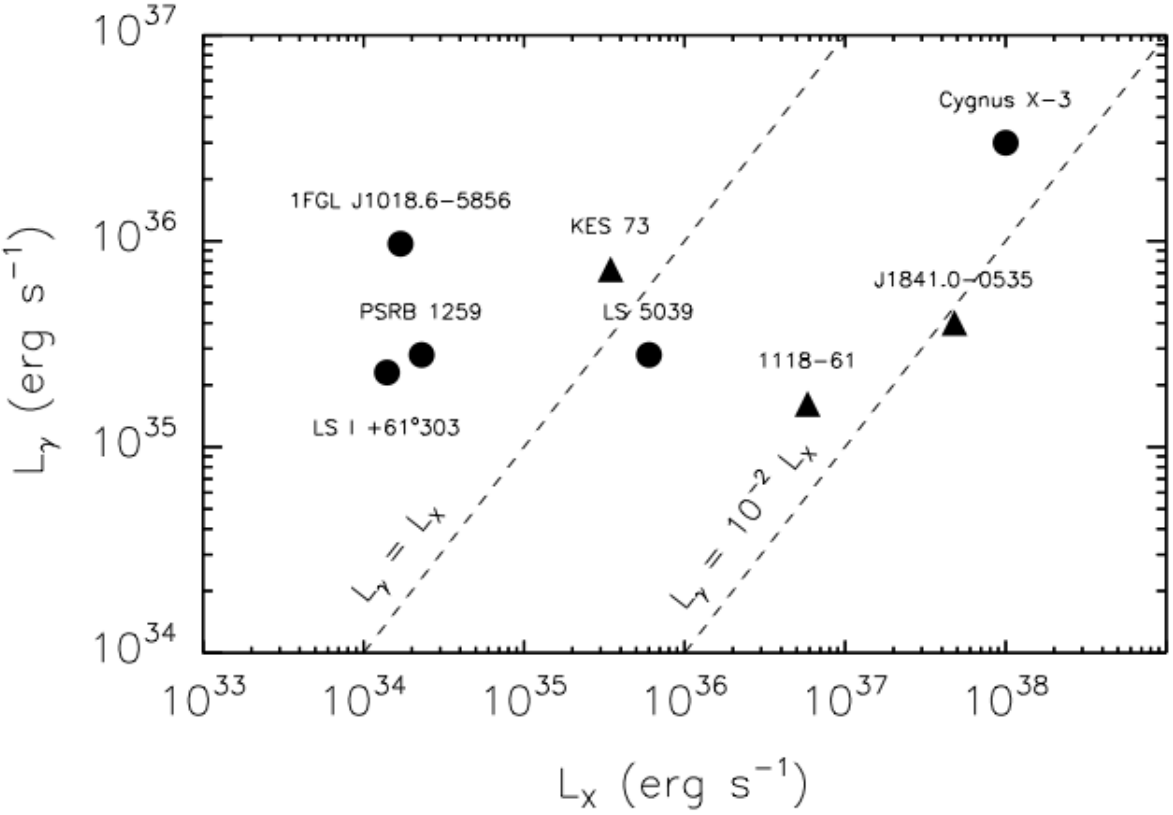

Figure 7.3: *X-ray luminosities versus gamma-ray luminosities for known Fermi gamma-ray sources (circles) and the candidates analysed in section 6.1 (triangles). The gamma-ray upper limits are used for the triangle sources.*

Conclusion

The current list of known Fermi gamma-ray binaries stands at five, which would suggest that they are a rare class of astrophysical sources at high energies. The lack of conclusive detections for any of the 156 X-ray and radio binaries would suggest that gamma-ray emission is not common in those systems.

Nevertheless, PSR B1259-63 and Cygnus X-3 are firmly detected with Fermi and there is a hint of detection for Circinus X-1, although the chance probability of 4% is too high to claim definitive detection. The X-ray luminosity and upper limit gamma-ray luminosity for KES 73 place it in a similar position to the already detected gamma-ray sources.

The hint of, but not statistically significant, detection of Circinus X-1 and the interesting candidates suggest that further studies could be fruitful. This is not always dependent on more data being available as the current Fermi data set can be improved further. For example, the sources analysed are heavily dependent on the modeling of the Galactic diffuse emission as they are positioned on or close to the Galactic plane. The models for the Galactic diffuse emission are provided by the Fermi Collaboration and have undergone two updates over the last 3 years. However, the parameters for these models can be adjusted by the user and investigated for their effect on source analysis.

Further investigation could also be applied to the energy cuts used and their effect on the telescope sensitivity. Higher energy cuts result in better photon direction reconstruction but a reduction in the total number of photons available for analysis, which could influence the maximum likelihood statistics. The energy cuts used in this thesis are kept the same so as to standardise the catalogue analysis. However, there is no astrophysical reason to suggest that these energy cuts are optimum for all the sources.

One of the main issues when analysing sources close to the Galactic plane is source confusion due to the intrinsically poor single photon point spread function of Fermi. Of course this is a complex matter and not one easily dealt with by simple cuts. However, the Fermi satellite automatically tags each photon with a class that defines how well that photon was reconstructed for direction and energy. The current list of classes range from one to four, where the higher the number, the stricter the cuts (i.e. photons classed as one will be less accurately reconstructed compared to a class four photon). The cuts for this thesis use the class two, which is the default for Fermi analysis and contains all class three and four photons as well. Further investigation could be done on using higher class photons. However, this also introduces the issue of lower photon counts as the higher the class of photon, the less available.

Further analysis for the X-ray and radio binary catalogues could be improved with more accurate and up to date ephemerides for any periodicity searches. The three catalogue sources of interest did not have ephemeris data available and had to be analysed with the nearest pulsar that could potentially contribute to the gamma-ray flux, which was not ideal.

It would also be good to rigorously ascertain the underlaying probability distri-

bution of the TS statistic since it clearly does not behave as the formal likelihood ratio is expected to.

The data for this thesis was cut off on August 2012 so that 4 years of Fermi data could be analysed for all sources. However, the Fermi satellite is an all sky observatory and continues to collect data for the whole sky every 3 hours. There has been almost a third more data collected by Fermi since the cut off for the data presented in this thesis. There is a wealth of data that will continue to grow and that can be "mined" for gamma-ray counterparts to radio and X-ray binaries.

Appendix A

X-ray Binary Pulsars Catalogue

Name	Flux > 200 MeV (ph/cm2/s)	dFlux (ph/cm2/s)	Index	± Index	TS
0050.1-7247	2.52E-10	3.68E-11	-2.0	0.2	0.3
0142+614	3.84E-09	1.03E-08	-4.8	0.7	2.6
0352+30	1.37E-10	1.19E-10	-2.0	0.3	0.1
0535+26	1.18E-12	1.23E-12	-1.9	0.2	0.0
0655.8-0708	1.60E-08	2.96E-09	-3.5	0.1	33.6
0728-25	9.86E-09	2.66E-09	-3.9	0.1	20.1
1048.1-5937	3.27E-12	4.33E-12	-4.6	0.6	0.0
1118-61	2.45E-08	1.71E-08	-2.8	0.1	42.5
1323-62	1.42E-12	1.27E-11	-2.4	0.2	0.0
1416-62	5.55E-13	4.69E-12	-5.0	0.7	0.0
1538-52	8.30E-09	5.57E-09	-3.1	0.3	4.1
1553-542	1.48E-12	5.30E-12	-2.4	0.2	0.0

1626-67	1.10E-12	2.89E-12	-2.8	0.3	0.0
1700-37	1.31E-12	1.95E-12	-2.5	0.3	0.0
1907+09	1.70E-12	1.91E-11	-2.2	0.2	0.0
1909+07	1.63E-12	6.37E-12	-2.2	0.2	0.0
2206+54	1.60E-12	3.17E-10	-3.2	0.3	0.0
2259.0+5836	5.04E-13	1.32E-14	-5.0	0.6	0.0
2905-121-1	5.93E-09	2.76E-09	-5.0	0.5	7.2
301-2	5.85E-09	5.29E-09	-2.8	0.3	2.5
Ginga_0834-430	8.73E-10	1.43E-10	-3.1	0.3	2.7
Ginga_1722-36	9.55E-10	8.76E-11	-2.2	0.2	1.3
Ginga_1843+00	7.36E-09	2.89E-08	-3.0	0.3	2.3
Ginga_1843-02	5.04E-08	2.91E-08	-2.8	0.1	57.9
Ginga_2138+56	9.95E-09	2.99E-09	-3.6	0.2	12.9
Her_X-1	9.61E-13	5.44E-11	-3.4	0.4	0.0
J004723.7-731226	3.72E-09	1.34E-09	-2.4	0.1	28.6
J0049.0-7250	3.39E-10	4.06E-10	-2.0	0.2	0.5
J0049.4-7323	4.51E-09	1.36E-09	-2.4	0.1	43.8
J0049-732	1.18E-09	5.61E-10	-2.0	0.2	6.2
J0051-722	5.18E-13	2.48E-12	-2.0	0.3	0.0
J0051-733	1.47E-09	5.75E-10	-2.0	0.1	10.0
J0051.8-7310	8.92E-10	6.49E-10	-2.0	0.2	2.7
J0052.1-7319	1.39E-09	5.47E-10	-2.0	0.1	8.4
J0052-723	1.10E-10	4.63E-11	-2.0	0.2	0.1

J0053-724	2.18E-09	1.35E-09	-2.1	0.1	16.2
J0054-720	6.53E-13	4.61E-12	-2.0	0.3	0.0
J0054.9-7226	5.47E-10	6.84E-12	-2.0	0.3	1.4
J0054.9-7245	8.86E-10	3.89E-10	-2.0	0.2	2.5
J0055.2-7238	4.15E-09	2.80E-09	-2.4	0.1	26.3
J005736.2-721934	6.26E-10	7.55E-12	-2.0	0.3	2.1
J0057.4-7325	4.74E-09	1.95E-09	-2.5	0.1	35.0
J0057.8-7207	2.50E-12	1.83E-11	-2.0	0.2	0.0
J0058-720	5.00E-13	3.41E-13	-2.0	0.2	0.0
J0059.2-7138	5.05E-13	8.62E-14	-2.0	0.2	0.0
J0100-7211	4.68E-11	9.55E-11	-2.0	0.3	0.0
J0101.0-7206	6.29E-13	1.05E-11	-2.0	0.2	0.0
J0101.3-7211	5.02E-13	4.61E-13	-2.0	0.3	0.0
J0103-722	7.31E-11	1.17E-10	-2.0	0.2	0.0
J0105-722	1.28E-09	1.55E-09	-2.2	0.2	9.3
J0111-732	7.62E-12	1.62E-11	-2.0	0.2	0.0
J0117.6-7330	2.32E-09	1.55E-09	-5.0	0.4	3.9
J0502.9-6626	1.01E-09	2.20E-11	-2.0	0.1	3.3
J0529.8-6556	2.46E-09	1.72E-09	-5.0	0.5	3.6
J0531.2-6609	1.84E-09	2.50E-10	-2.0	0.1	10.5
J0535.6_6651	5.22E-12	3.30E-11	-2.0	0.2	0.0
J0544.1-7100	8.04E-09	1.71E-09	-2.9	0.1	32.7
J1008-57	2.88E-09	1.29E-09	-5.0	0.6	0.6

J1324.4-6200	1.38E-12	1.49E-11	-2.5	0.3	0.0
J1452.8-5949	6.79E-11	7.66E-10	-1.0	0.3	3.7
J1543-568	1.71E-12	1.80E-11	-2.2	0.2	0.0
J1700-419	5.19E-13	3.01E-12	-4.9	0.5	0.0
J1700.7-4139	5.03E-13	4.50E-13	-2.1	0.2	0.0
J170849.0-400910	5.62E-10	4.13E-11	-2.2	0.2	0.5
J1735.9-2726	1.43E-12	6.23E-12	-1.9	0.3	0.0
J1740.2-2848	5.27E-13	1.26E-12	-2.0	0.2	0.0
J1746-2852	9.34E-12	1.77E-11	-2.0	0.2	0.0
J1749.2-2725	5.68E-10	9.92E-11	-2.1	0.1	2.6
J1802.7-2017	1.74E-12	1.71E-11	-2.2	0.2	0.0
J1809.8-1943	4.34E-08	3.77E-08	-2.8	0.1	45.0
J1820.5-1434	4.06E-08	3.79E-08	-2.7	0.1	43.5
J1838.4-0301	1.48E-08	1.51E-08	-3.0	0.2	8.4
J1841.0-0535	1.52E-08	2.66E-09	-2.0	0.1	41.8
J1844-0258	2.21E-08	2.94E-08	-2.4	0.1	22.8
J1855-026	2.50E-08	5.72E-09	-5.0	0.1	28.6
J1858+034	2.81E-08	1.92E-08	-2.6	0.1	32.6
J1859+083	1.56E-12	6.20E-11	-2.4	0.2	0.0
J1906+09	1.30E-12	3.26E-12	-2.5	0.3	0.0
J1946+274	2.09E-08	3.63E-09	-5.0	0.4	47.4
J1948+32	7.30E-09	4.41E-09	-5.0	0.4	4.7
J1958.2+3232	1.51E-08	4.64E-09	-5.0	0.3	20.5

J2058+42	1.42E-12	1.79E-11	-2.4	0.2	0.0
J2103.5+4545	1.19E-12	1.03E-10	-2.8	0.3	0.0
KES_73	4.77E-08	4.39E-09	-2.2	0.1	144.6
LMC_X-4	3.25E-09	1.96E-09	-5.0	0.5	5.5
LS_992	4.12E-10	2.12E-10	-2.0	0.2	0.5
Sct_X-1	4.62E-08	1.52E-08	-2.5	0.1	78.7
SMC_X-1	2.61E-09	1.89E-09	-5.0	0.4	4.9
SMC_X-2	3.41E-09	1.76E-09	-2.8	0.1	11.2
V0332+53	5.21E-13	9.43E-13	-2.0	0.2	0.0
V2116_Oph	1.65E-12	4.25E-12	-2.2	0.2	0.0
V2246_Cyg	5.20E-13	5.96E-12	-4.9	0.6	0.0
V635_Cas	1.61E-09	3.14E-09	-3.0	0.3	0.4
V691	1.05E-12	4.18E-11	-2.9	0.3	0.0
V801_Cen	5.09E-13	7.79E-12	-5.0	0.5	0.0
V830_Cen	5.36E-13	1.02E-10	-4.8	0.4	0.0
V850_Cen	4.55E-09	2.30E-08	-2.7	0.3	1.8
VEL_X-1	6.67E-13	1.19E-12	-2.0	0.3	0.0
XTE_SMC95	6.01E-09	2.43E-09	-2.5	0.1	44.8

Appendix B

Radio Binary Pulsars Catalogue

Name	Flux > 200 MeV (ph/cm2/s)	dFlux (ph/cm2/s)	Index	± Index	TS
J0023-7204	1.34E-09	1.99E-10	-2.0	0.2	3.1
J0034-0534	4.47E-12	5.96E-11	-2.0	0.3	0.0
J0045-7319	5.42E-10	5.44E-10	-2.0	0.3	1.3
J0218+4232	2.90E-12	2.83E-11	-2.2	0.2	0.0
J0437-4715	6.00E-13	4.41E-13	-2.3	0.2	0.0
J0514-4002A	4.05E-13	7.62E-14	-1.8	0.3	0.0
J0613-0200	5.57E-10	8.65E-11	-2.0	0.3	0.0
J0621+1002	6.38E-13	1.94E-11	-1.9	0.2	0.0
J0700+6418	5.02E-13	4.40E-13	-2.0	0.3	0.0
J0737-3039A	5.52E-10	4.03E-11	-2.0	0.2	0.5
J0751+1807	1.41E-12	6.22E-12	-2.0	0.2	0.0
J0823+0159	5.07E-13	1.16E-12	-2.0	0.4	0.0

J1012+5307	9.24E-12	1.67E-11	-2.0	0.3	0.0
J1022+1001	5.67E-10	9.91E-11	-2.0	0.1	2.6
J1045-4509	1.42E-12	1.27E-11	-2.4	0.2	0.0
J1141-6545	5.35E-13	4.49E-12	-4.9	0.6	0.0
J1157-5112	8.50E-09	5.77E-09	-3.2	0.2	4.2
J1232-6501	1.36E-12	5.18E-12	-2.3	0.2	0.0
J1300+1240	3.70E-10	7.52E-11	-2.0	0.3	2.1
J1302-6350	2.41E-09	1.69E-09	-4.9	0.4	4.8
J1312+1810	5.06E-13	1.47E-13	-2.0	0.2	0.0
J1342+2822A	1.68E-12	1.79E-11	-2.8	0.3	0.0
J1420-5625	6.49E-11	7.36E-10	-1.1	0.4	3.4
J1435-6100	1.96E-12	1.69E-11	-2.3	0.2	0.0
J1454-5846	4.59E-13	4.21E-12	-4.8	0.4	0.0
J1455-3330	5.38E-13	1.02E-13	-2.0	0.2	0.0
J1518+4904	5.53E-13	2.09E-12	-2.0	0.2	0.0
J1537+1155	4.11E-12	2.60E-11	-2.0	0.3	0.0
J1603-7202	5.78E-13	8.49E-12	-4.8	0.5	0.0
J1618-39	3.46E-13	2.32E-10	-4.5	0.4	0.0
J1623-2631	6.44E-09	3.38E-08	-2.7	0.2	2.7
J1640+2224	5.71E-10	1.59E-10	-2.0	0.2	2.8
J1641+3627B	6.27E-13	1.33E-13	-2.1	0.3	0.0
J1643-1224	6.62E-13	3.18E-12	-2.0	0.3	0.0
J1701-3006A	1.32E-12	7.13E-12	-1.9	0.2	0.0

J1709+2313	6.19E-13	2.38E-12	-2.2	0.2	0.0
J1711-4322	9.35E-12	1.69E-11	-2.0	0.3	0.0
J1713+0747	6.68E-11	7.87E-10	-1.2	0.2	4.3
J1721-1936	1.82E-12	1.81E-11	-2.2	0.3	0.0
J1732-5049	4.13E-13	4.22E-12	-4.8	0.4	0.0
J1740-3052	5.53E-13	6.48E-13	-3.1	0.4	0.0
J1740-5340	7.73E-10	3.04E-11	-2.1	0.2	0.7
J1745-0952	3.38E-12	1.61E-11	-2.0	0.3	0.0
J1748-2446A	3.77E-13	8.32E-13	-1.8	0.2	0.0
J1757-5322	3.24E-13	6.84E-14	-2.0	0.3	0.0
J1803-2712	8.23E-11	9.43E-11	-2.2	0.3	0.0
J1804-0735	2.72E-09	5.32E-09	-3.3	0.3	0.6
J1804-2717	4.11E-12	6.42E-11	-3.8	0.5	0.0
J1807-2459A	9.12E-13	3.66E-12	-4.8	0.5	0.0
J1810-2005	3.35E-13	2.23E-10	-4.4	0.4	0.0
J1811-1736	6.78E-13	3.29E-13	-2.5	0.3	0.0
J1823-1115	4.31E-10	3.05E-11	-2.3	0.2	0.5
J1829+2456	3.32E-12	4.26E-12	-3.4	0.4	0.0
J1834-0010	7.75E-13	2.27E-12	-2.9	0.4	0.0

Bibliography

Abdo, A.A., Ackermann, M., Ajello, M., Atwood, W.B. & the Fermi-LAT Collaboration (2009a). Fermi LAT Observations of LS I +61°303: First Detection of an Orbital Modulation in GeV Gamma Rays. ApJ, **701**, L123–L128. 22, 50

Abdo, A.A., Ackermann, M., Atwood, W.B., Bagagli, R., Baldini, L., Ballet, J., Band, D.L., Barbiellini, G., Baring, M.G., Bartelt, J. & et al. (2009b). Fermi Large Area Telescope Observations of the Vela Pulsar. ApJ, **696**, 1084–1093. 105

Abdo, A.A., Ackermann, M., Ajello, M., Allafort, A., Antolini, E., Atwood, W.B., Axelsson, M., Baldini, L., Ballet, J., Barbiellini, G. & et al. (2010). Fermi Large Area Telescope First Source Catalog. ApJS, **188**, 405–436. 49

Abdo, A.A., Ackermann, M., Ajello, M., Allafort, A. & the Fermi-LAT Collaboration (2011). Discovery of High-energy Gamma-ray Emission from the Binary System PSR B1259-63/LS 2883 around Periastron with Fermi. ApJ, **736**, L11. xxvii, xxxii, 23, 62, 67, 127, 134, 171

Ackermann, M., Ajello, M., Albert, A., Allafort, A., Atwood, W.B. & the Fermi-LAT Collaboration (2012). The Fermi Large Area Telescope on Orbit: Event Classification, Instrument Response Functions, and Calibration. *apjs*, **203**, 4. xvii, 32, 41, 42, 43, 48, 109, 135

Actis, M., Agnetta, G., Aharonian, F., Akhperjanian, A., Aleksić, J., Aliu, E., Allan, D., Allekotte, I., Antico, F., Antonelli, L.A. & et al. (2011). Design concepts for the Cherenkov Telescope Array CTA: an advanced facility for ground-based high-energy gamma-ray astronomy. *Experimental Astronomy*, **32**, 193–316. 29

AGILE Collaboration (2009a). Extreme particle acceleration in the microquasar CygnusX-3. Nature, **462**, 620–623. 19

AGILE Collaboration (2009b). Extreme particle acceleration in the microquasar CygnusX-3. *nat*, **462**, 620–623. 64

AGILE Collaboration (2010). AGILE gamma-ray detection of Cygnus X-1. *The Astronomer's Telegram*, **2715**, 1. 9

Aharonian, F. (2004). Very High Energy Gamma Rays and Origin of Cosmic Rays. In P. Chen, E. Bloom, G. Madejski, & V. Patrosian, ed., *Proceedings of the 22nd Texas Symposium on Relativistic Astrophysics at Stanford. Stanford California, December 13-17, 2004. Editors: Pisin Chen, Elliott Bloom, Greg Madejski (SLAC), Vahe Patrosian (Stanford University)., p.43*, 43–+. 17

Aharonian, F.A. & Bogovalov, S.V. (2003). Exploring physics of rotation powered pulsars with sub-10 GeV imaging atmospheric Cherenkov telescopes. *na*, **8**, 85–103. xvi, 6, 7

Albert, J. & the MAGIC collaboration (2008). MAGIC Observations of the Unidentified γ-Ray Source TeV J2032+4130. *apjl*, **675**, L25–L28. 64

Albert, J., Aliu, E., Anderhub, H., Antoranz, P. & for the MAGIC Collaboration (2006). Variable Very-High-Energy Gamma-Ray Emission from the Microquasar LS I +61 303. *Science*, **312**, 1771–1773. 50

Alexander, T. (1997). Is AGN Variability Correlated with Other AGN Properties? ZDCF Analysis of Small Samples of Sparse Light Curves. In D. Maoz, A. Sternberg, & E. M. Leibowitz, ed., *Astronomical Time Series*, vol. 218 of *Astrophysics and Space Science Library*, 163–+. 91

Ali, M.O. & the HESS collaboration (2012). Constraints on the gamma-ray emission from the cluster-scale AGN outburst in the Hydra A galaxy cluster. A&A, **545**, A103. 103

Aliu, E., Archambault, S., Behera, B., Berger, K., Beilicke, M., Benbow, W., Bird, R., Bouvier, A., Bugaev, V., Cerruti, M., Chen, X., Ciupik, L., Connolly, M.P., Cui, W., Dumm, J., Falcone, A., Federici, S., Feng, Q., Finley, J.P., Fortin, P., Fortson, L., Furniss, A., Galante, N., Gillanders, G.H., Griffin, S., Griffiths, S.T., Grube, J., Gyuk, G., Hanna, D., Holder, J., Hughes, G., Humensky, T.B., Kaaret, P., Kertzman, M., Khassen, Y., Kieda, D., Krennrich, F., Lang, M.J., Maier, G., Majumdar, P., McArthur, S., McCann, A., Moriarty, P., Mukherjee, R., O'Faoláin de Bhróithe, A., Ong, R.A., Otte, A.N., Park, N., Perkins, J.S., Pohl, M., Popkow, A., Prokoph, H., Quinn, J., Ragan, K., Rajotte, J., Ratliff,

G., Reynolds, P.T., Richards, G.T., Roache, E., Sembroski, G.H., Sheidaei, F., Skole, C., Smith, A.W., Staszak, D., Telezhinsky, I., Tyler, J., Varlotta, A., Vincent, S., Wakely, S.P., Weekes, T.C., Weinstein, A., Welsing, R., Zajczyk, A. & Zitzer, B. (2013). Multiwavelength Observations of the TeV Binary LS I +61° 303 with VERITAS, Fermi-LAT, and Swift/XRT during a TeV Outburst. ApJ, **779**, 88. 53

Allison, J., Amako, K., Apostolakis, J. & Araujo, H. (2006). Geant4 developments and applications. *IEEE Transactions on Nuclear Science*, **53**, 270–278. 36

Atoyan, A.M. & Aharonian, F.A. (1999). Modelling of the non-thermal flares in the Galactic microquasar GRS 1915+105. MNRAS, **302**, 253–276. 18, 63

Attix, F.H. (1987). *Introduction to Radiological Physics and Radiation Dosimetry*. Wiley VCH, 1987. xvii, 34

Atwood, W.B., Bagagli, R., Baldini, L., Bellazzini, R., Barbiellini, G., Belli, F., Borden, T., Brez, A., Brigida, M., Caliandro, G.A., Cecchi, C., Cohen-Tanugi, J., De Angelis, A., Drell, P., Favuzzi, C., Fukazawa, Y., Fusco, P., Gargano, F., Germani, S., Giannitrapani, R., Giglietto, N., Giordano, F., Himel, T., Hirayama, M., Johnson, R.P., Katagiri, H., Kataoka, J., Kawai, N., Kroeger, W., Kuss, M., Latronico, L., Longo, F., Loparco, F., Lubrano, P., Massai, M.M., Mazziotta, M.N., Minuti, M., Mizuno, T., Morselli, A., Nelson, D., Nordby, M., Ohsugi, T., Omodei, N., Ozaki, M., Pepe, M., Rainò, S., Rando, R., Razzano, M., Rich, D., Sadrozinski, H.F.W., Scolieri,

G., Sgrò, C., Spandre, G., Spinelli, P., Sugizaki, M., Tajima, H., Takahashi, H., Takahashi, T., Yoshida, S., Young, C. & Ziegler, M. (2007). Design and initial tests of the Tracker-converter of the Gamma-ray Large Area Space Telescope. *Astroparticle Physics*, **28**, 422–434. 106

Atwood, W.B., Abdo, A.A., Ackermann, M., Althouse, W., Anderson, B., Axelsson, M., Baldini, L., Ballet, J., Band, D.L., Barbiellini, G. & et al. (2009). The Large Area Telescope on the Gamma-Ray Space Telescope Mission. ApJ, **697**, 1071–1102. 29, 40

Baldini, L., Barbiellini, G., Bellazzini, R., Ylinen, T. & the Fermi-LAT Collaboration (2007). Preliminary results of the LAT Calibration Unit beam tests. In S. Ritz, P. Michelson & C.A. Meegan, eds., *The First GLAST Symposium*, vol. 921 of *American Institute of Physics Conference Series*, 190–204. 36

Ball, L., Melatos, A., Johnston, S. & Skjæraasen, O. (1998). Transient radio emission from PSR B1259-63. *memsai*, **69**, 1043–+. xx, 62

Bamba, A., Yokogawa, J., Ueno, M., Koyama, K. & Yamauchi, S. (2001). Discovery of a Transient X-Ray Pulsar, AX J1841.0-0536, in the Scutum Arm Region with ASCA. PASJ, **53**, 1179–1183. 152

Bednarek, W. (2007). GeV-TeV γ light curves expected in the IC e$\wedge$ $\pm$ pair cascade model for massive binaries: application to LS 5039. A&A, **464**, 259–262. 54

Bignami, G.F., Boella, G., Burger, J.J., Taylor, B.G., Keirle, P., Paul, J.A., Mayer-Hasselwander, H.A., Pfeffermann, E., Scarsi, L.

& Swanenburg, B.N. (1975). The COS-B experiment for gamma-ray astronomy. *Space Science Instrumentation*, **1**, 245–268. 26

Boinee, P., Cabras, G., de Angelis, A. & Favretto, D. (2003). Gleam: the GLAST Large Area Telescope Simulation Framework. In S. Ciprini, A. de Angelis, P. Lubrano & O. Mansutti, eds., *Science with the New Generation of High Energy Gamma-Ray Experiments : Between Astrophysics and Astroparticle Physics*, 141. 35

Böttcher, M. & Dermer, C.D. (2005). Photon-Photon Absorption of Very High Energy Gamma Rays from Microquasars: Application to LS 5039. ApJ, **634**, L81–L84. 3

Brazier, S.K.T., Carraminana, A., Chadwick, M.P., Dipper, A.N., Lincoln, W.E., Mannings, G.V., McComb, L.T.J., Orford, J.K., Rayner, M.S. & Turver, E.K. (1990). Evidence for a 12 ms Pulsar in Cygnus X-3. *International Cosmic Ray Conference*, **2**, 91. 64

Breiman, L., Friedman, J., Olshen, R. & Stone, C. (1984). *Classification and Regression Trees*. Wadsworth and Brooks, Monterey, CA. 37

Buccheri, R. & Sacco, B. (1985). Time Analysis in Astronomy: Tools for Periodicity Searches. In V. di Gesu, L. Scarsi, P. Crane, J.H. Friedman & S. Levialdi, eds., *Data Analysis in Astronomy*, 15. 73

Calvelo, D.E., Fender, R., Broderick, J., Moin, A., Tingay, S., Tzioumis, T. & Nicolson, G. (2010). Radio brightening of Circinus X-1. *The Astronomer's Telegram*, **2699**, 1. 167

Carpenter, G.F., Coe, M.J. & Engel, A.R. (1976). New X-ray measurements of the Crab spectrum in the range 26 keV-1.2 MeV. Nature, **259**, 99. 5

Casares, J., Ribó, M., Ribas, I., Paredes, J.M., Martí, J. & Herrero, A. (2005). A possible black hole in the γ-ray microquasar LS 5039. MNRAS, **364**, 899–908. xix, 55

Cash, W. (1979). Parameter estimation in astronomy through application of the likelihood ratio. *apj*, **228**, 939–947. 103

Cerutti, B., Dubus, G. & Henri, G. (2008). Spectral signature of a free pulsar wind in the gamma-ray binaries LS 5039 and LSI +61°303. A&A, **488**, 37–46. 55

Chadwick, P.M., Dipper, N.A., Dowthwaite, J.C., Gibson, A.I. & Harrison, A.B. (1985). A 12.6-ms pulsar in Cygnus X-3. Nature, **318**, 642–644. 64

Chernyakova, M. (2006). Multiwavelength observations of the 2007 PSR B1259-63 periastron passage. *XMM-Newton Proposal*, 169. 61, 130

Chernyakova, M., Neronov, A., Aharonian, F., Uchiyama, Y. & Takahashi, T. (2009). X-ray observations of PSR B1259-63 near the 2007 periastron passage. MNRAS, **397**, 2123–2132. 61

Chernyakova, M., Neronov, A., Molkov, S., Malyshev, D., Lutovinov, A. & Pooley, G. (2012). Superorbital Modulation of X-Ray Emission from Gamma-Ray Binary LSI +61 303. ApJ, **747**, L29. 51

Cheung, C.C. & on behalf of the Fermi-LAT collaboration (2013). Fermi Discovers a New Population of Gamma-ray Novae. *ArXiv e-prints*. 9

Cheung, C.C., Jean, P., Shore, S.N. & Fermi Large Area Telescope Collaboration (2013). Fermi-LAT Gamma-ray Observations of Nova Centauri 2013. *The Astronomer's Telegram*, **5649**, 1. 9

Church, M.J., Halai, G.S. & Bałucińska-Church, M. (2006). An explanation of the Z-track sources. A&A, **460**, 233–244. 11

Clark, D.H., Parkinson, J.H. & Caswell, J.L. (1975). Is CIR X-1 a runaway binary. *nat*, **254**, 674–676. 110

Cocke, W.J., Disney, M.J. & Taylor, D.J. (1969). Discovery of Optical Signals from Pulsar NP 0532. Nature, **221**, 525–527. 5

Coe, M.J., Roche, P., Everall, C., Fishman, G.J., Hagedon, K.S., Finger, M., Wilson, R.B., Buckley, D.A.H., Shrader, C., Fabregat, J., Polcaro, V.F., Giovannelli, F. & Villada, M. (1994). Multiwaveband study of a major X-ray outburst from the Be/X-ray transient system A 1118-616. A&A, **289**, 784–794. 144

Corbet, R.H.D., Fermi LAT Collaboration, Coe, M.J., Edwards, P.G., Filipovic, M.D., Payne, J.L., Stevens, J. & Torres, M.A.P. (2011). Discovery Of The New Gamma-ray Binary 1FGL J1018.6-5856. In *AAS/High Energy Astrophysics Division*, vol. 12 of *AAS/High Energy Astrophysics Division*, 03.07. 57, 67

DE JAGER, O.C. (1994). On periodicity tests and flux limit calculations for gamma-ray pulsars. ApJ, **436**, 239–248. 74

DE JAGER, O.C., RAUBENHEIMER, B.C. & SWANEPOEL, J.W.H. (1989a). A poweful test for weak periodic signals with unknown light curve shape in sparse data. A&A, **221**, 180–190. 74, 75

DE JAGER, O.C., RAUBENHEIMER, B.C. & SWANEPOEL, J.W.H. (1989b). The Rayleigh Statistic in the Case of Weak Signals - Applications and Pitfalls. In V. di Gesu, L. Scarsi, P. Crane, J.H. Friedman, S. Levialdi & M.C. Maccarone, eds., *Data Analysis in Astronomy*, 21. 73

DE ONA WILHELMI, E.D.O.W. (2011). X-ray and VHE gamma-ray observations of SNR G284.3-1.8 and PSR J1016-5857 with XMM-Newton and the H.E.S.S. Telescope Array. In *International Cosmic Ray Conference*, vol. 7 of *International Cosmic Ray Conference*, 94. 57

DHAWAN, V., MIODUSZEWSKI, A. & RUPEN, M. (2006). LS I +61 303 is a Be-Pulsar binary, not a Microquasar. In *VI Microquasar Workshop: Microquasars and Beyond*. 22, 52

DONE, C., GIERLIŃSKI, M. & KUBOTA, A. (2007). Modelling the behaviour of accretion flows in X-ray binaries. Everything you always wanted to know about accretion but were afraid to ask. A&A Rev., **15**, 1–66. 10, 11

DUBUS, G. (2006a). Gamma-ray absorption in massive X-ray binaries. A&A, **451**, 9–18. 70

Dubus, G. (2006b). Gamma-ray binaries: pulsars in disguise? A&A, **456**, 801–817. 11

Dubus, G. (2006c). Gamma-ray emission from the X-ray binary LS 5039. In J.M. Alimi & A. Füzfa, eds., *Albert Einstein Century International Conference*, vol. 861 of *American Institute of Physics Conference Series*, 608–613. 54, 55

Dubus, G. (2007). Gamma-ray emission from binaries with GLAST. In J. Bouvier, A. Chalabaev, & C. Charbonnel, ed., *SF2A-2007: Proceedings of the Annual meeting of the French Society of Astronomy and Astrophysics*, 163–+. 1, 166

Dubus, G. & Cerutti, B. (2013). What caused the GeV flare of PSR B1259-63? A&A, **557**, A127. 170

Dubus, G., de Naurois, M. & H.E.S.S. Collaboration (2005). VHE emission from the X-ray binary LS 5039. In F. Casoli, T. Contini, J.M. Hameury & L. Pagani, eds., *SF2A-2005: Semaine de l'Astrophysique Francaise*, 447. 54

Eadie, W.T., Drijard, D., James, F.E., Roos, M. & Sadoulet, B. (1971). *Statistical Methods in Experimental Physics*. North Holland. 173

Edelson, R.A. & Krolik, J.H. (1988). The discrete correlation function - A new method for analyzing unevenly sampled variability data. *apj*, **333**, 646–659. 91

Esposito, P., Caraveo, P.A., Pellizzoni, A., de Luca, A., Gehrels, N. & Marelli, M.A. (2007). Swift/XRT monitoring of five orbital cycles of LS I +61° 303. A&A, **474**, 575–578. 51

Eyles, C.J., Skinner, G.K., Willmore, A.P. & Rosenberg, F.D. (1975). Variable X-ray source near CEN X-3. Nature, **254**, 577. 144

Fegan, D.J., Cawley, M.F., Gibbs, K., Gorham, P.W., Lamb, R.C., Porter, N.A., Reynolds, P.T., Stenger, V.J. & Weekes, T.C. (1987). Search for a 12. 59 ms. Pulsar in Cygnus X-3 at E >400 GeV. In K.E. Turver, ed., *NATO ASIC Proc. 199: Very High Energy Gamma Ray Astronomy*, 111. 64

Feigelson, E.D. & Jogesh Babu, G. (2012). *Modern Statistical Methods for Astronomy*. Cambridge University Press, 2012. 71

Fender, R. (2006). Jets From X-ray Binaries: A Brief Overview and Comparison with Active Galactic Nuclei. In P.A. Hughes & J.N. Bregman, eds., *Relativistic Jets: The Common Physics of AGN, Microquasars, and Gamma-Ray Bursts*, vol. 856 of *American Institute of Physics Conference Series*, 23–32. 69

Fender, R. & Maccarone, T. (2004). High Energy Emission from Microquasars. In K.S. Cheng & G.E. Romero, eds., *Cosmic Gamma-Ray Sources*, vol. 304 of *Astrophysics and Space Science Library*, 205. 2

Fender, R., Wu, K., Johnston, H., Tzioumis, T., Jonker, P., Spencer, R. & van der Klis, M. (2004). An ultra-relativistic outflow from a neutron star accreting gas from a companion. Nature, **427**, 222–224. 168

Fender, R., Tzioumis, T. & Tudose, V. (2005). Dramatic radio brightening of Circinus X-1. *The Astronomer's Telegram*, **563**, 1. 18

Fermi LAT Collaboration (2009a). Fermi/LAT observations of LS 5039. ApJ, **706**, L56–L61. xix, 55, 56

Fermi LAT Collaboration (2009b). Modulated High-Energy Gamma-Ray Emission from the Microquasar Cygnus X-3. *Science*, **326**, 1512–. xx, 19, 64, 65, 67, 120

Fermi LAT Collaboration (2010). Gamma-Ray Emission Concurrent with the Nova in the Symbiotic Binary V407 Cygni. *Science*, **329**, 817–. 9

Fichtel, C.E., Hartman, R.C., Kniffen, D.A., Thompson, D.J., Ogelman, H., Ozel, M.E., Tumer, T. & Bignami, G.F. (1975). High-energy gamma-ray results from the second small astronomy satellite. ApJ, **198**, 163–182. 26

Filippova, E.V., Tsygankov, S.S., Lutovinov, A.A. & Sunyaev, R.A. (2005). Hard Spectra of X-ray Pulsars from INTEGRAL Data. *Astronomy Letters*, **31**, 729–747. 152

Fisher, R.A. (1920). Accuracy of observation, A mathematical examination of the methods of determining, by the mean error and by the mean square error. MNRAS, **80**, 758–770. 100

Fruhwirth, R., Regler, M., Bock, R.K., Grote, H. & Notz, D. (2000). *Data analysis techniques for high-energy physics*. No. 11 in Cambridge monographs on particle physics, nuclear physics, and cosmology, Cambridge University Press, 2nd edn. 36

Gaensler, B.M., Stappers, B.W., Frail, D.A., Moffett, D.A., Johnston, S. & Chatterjee, S. (2000). Limits on radio emission from pulsar wind nebulae. *mnras*, **318**, 58–66. 5

Gallo, E., Fender, R., Kaiser, C., Russell, D., Morganti, R., Oosterloo, T. & Heinz, S. (2005). A dark jet dominates the power output of the stellar black hole Cygnus X-1. Nature, **436**, 819–821. xvi, 19, 21

Gaskell, C.M. & Peterson, B.M. (1987). The accuracy of cross-correlation estimates of quasar emission-line region sizes. *apjs*, **65**, 1–11. 91

Georganopoulos, M., Aharonian, F.A. & Kirk, J.G. (2002). External Compton emission from relativistic jets in Galactic black hole candidates and ultraluminous X-ray sources. A&A, **388**, L25–L28. 63

Glass, I.S. (1978). Variations of Circinus X-1 in the infrared. *mnras*, **183**, 335–340. 110

Goss, W.M. & Mebold, U. (1977). The distance of CIR X-1. *mnras*, **181**, 255–258. 110

Gregory, A.A., Patterson, J.R., Roberts, M.D., Smith, N.I. & Thornton, G.J. (1990). Observations of Cygnus X-3 near 100 TeV using the low elevation atmospheric Cherenkov technique. A&A, **237**, L5–L8. 64

Gregory, P.C. (2002). Bayesian Analysis of Radio Observations of the Be X-Ray Binary LS I +61°303. ApJ, **575**, 427–434. 51

Gregory, P.C. & Taylor, A.R. (1978). New highly variable radio source, possible counterpart of gamma-ray source CG135+1. Nature, **272**, 704–706. xviii, 50

Hadasch, D., Torres, D.F., Tanaka, T., Corbet, R.H.D., Hill, A.B., Dubois, R., Dubus, G., Glanzman, T., Corbel, S., Li, J., Chen, Y.P., Zhang, S., Caliandro, G.A., Kerr, M., Richards, J.L., Max-Moerbeck, W., Readhead, A. & Pooley, G. (2012). Long-term Monitoring of the High-energy γ-Ray Emission from LS I +61°303 and LS 5039. ApJ, **749**, 54. xviii, 51, 52, 54

Halpern, J.P., Gotthelf, E.V., Helfand, D.J., Gezari, S. & Wegner, G.A. (2004). Chandra and Optical Identification of AX J1841.0-0536. *The Astronomer's Telegram*, **289**, 1. 152

Hartman, R.C., Bertsch, D.L., Fichtel, C.E., Hunter, S.D., Kanbach, G., Kniffen, D.A., Kwok, P.W., Lin, Y.C., Mattox, J.R. & Mayer-Hasselwander, H.A. (1992). The EGRET high energy gamma ray telescope. In C.R. Shrader, N. Gehrels & B. Dennis, eds., *NASA Conference Publication*, vol. 3137 of *NASA Conference Publication*, 116–125. 26

Heitler, W. (1954). *Quantum theory of radiation*. Oxford University Press, 1954. 12, 28

HESS Collaboration (2005a). Discovery of the binary pulsar PSR B1259-63 in very-high-energy gamma rays around periastron with HESS. *aap*, **442**, 1–10. xxxii, 22, 61, 171

HESS Collaboration (2005b). Discovery of the binary pulsar PSR B1259-63 in very-high-energy gamma rays around periastron with HESS. A&A, **442**, 1–10. 23

HESS Collaboration (2005c). Discovery of Very High Energy Gamma Rays Associated with an X-ray Binary. *Science*, **309**, 746–749. 54

HESS Collaboration (2006a). HESS Observations of the Galactic Center Region and Their Possible Dark Matter Interpretation. *Physical Review Letters*, **97**, 221102–+. 29

HESS Collaboration (2006b). The H.E.S.S. Survey of the Inner Galaxy in Very High Energy Gamma Rays. *apj*, **636**, 777–797. 29

HESS Collaboration (2008). HESS very-high-energy gamma-ray sources without identified counterparts. *aap*, **477**, 353–363. 29

HESS Collaboration (2009). H.E.S.S. VHE gamma-ray observations of the microquasar GRS 1915+105. *ArXiv e-prints*. 18

HESS Collaboration (2012). Discovery of VHE emission towards the Carina arm region with the H.E.S.S. telescope array: HESS J1018-589. A&A, **541**, A5. xix, 58

Hill, A.B., Dubois, R., Torres, D.F. & Fermi LAT Collaboration (2011). Fermi results on γ-ray binaries. In D.F. Torres & N. Rea, eds., *High-Energy Emission from Pulsars and their Systems*, 498. xviii, 51

Hillas, A.M. (1985). Cerenkov light images of EAS produced by primary gamma. In F. C. Jones, ed., *International Cosmic Ray Conference*, vol. 3 of *International Cosmic Ray Conference*, 445–448. 28

Hillas, A.M. (2013). Evolution of ground-based gamma-ray astronomy from the early days to the Cherenkov Telescope Arrays. *Astroparticle Physics*, **43**, 19–43. 28

Hjalmarsdotter, L., Zdziarski, A.A., Szostek, A. & Hannikainen, D.C. (2009). Spectral variability in Cygnus X-3. MNRAS, **392**, 251–263. 63, 122, 169

Homan, J., Wijnands, R., van der Klis, M., Belloni, T., van Paradijs, J., Klein-Wolt, M., Fender, R. & Méndez, M. (2001). Correlated X-Ray Spectral and Timing Behavior of the Black Hole Candidate XTE J1550-564: A New Interpretation of Black Hole States. ApJS, **132**, 377–402. 10

Ives, J.C., Sanford, P.W. & Bell Burnell, S.J. (1975). Observations of a transient X-ray source with regular periodicity of 6.75 min. Nature, **254**, 578–580. 144

Janot-Pacheco, E., Ilovaisky, S.A. & Chevalier, C. (1981). A photometric and spectroscopic study of He 3-640 = A1118-61/. A&A, **99**, 274–284. 144

Johnston, S., Manchester, R.N., Lyne, A.G., Bailes, M., Kaspi, V.M., Qiao, G. & D'Amico, N. (1992). PSR 1259-63 - A binary radio pulsar with a Be star companion. ApJ, **387**, L37–L41. 130, 131, 170

Kaluzienski, L.J., Holt, S.S., Boldt, E.A. & Serlemitsos, P.J. (1976). Evidence for a 16.6 day period from Circinus X-1. *apjl*, **208**, L71–L75. 110

Kaspi, V.M. (2007). Recent progress on anomalous X-ray pulsars. Ap&SS, **308**, 1–11. 159

Kawachi, A., Naito, T., Patterson, J.R., Edwards, P.G., Asahara, A., Bicknell, G.V., Clay, R.W., Enomoto, R., Gunji, S., Hara, S., Hara, T., Hattori, T., Hayashi, S., Hayashi, S., Itoh, C., Kabuki, S., Kajino, F., Katagiri, H., Kifune, T., Ksenofontov, L., Kubo, H., Kushida, J., Matsubara, Y., Mizumoto, Y., Mori, M., Moro, H., Muraishi, H., Muraki, Y., Nakase, T., Nishida, D., Nishijima, K., Ohishi, M., Okumura, K., Protheroe, R.J., Sakurazawa, K., Swaby, D.L., Tanimori, T., Tokanai, F., Tsuchiya, K., Tsunoo, H., Uchida, T., Watanabe, A., Watanabe, S., Yanagita, S., Yoshida, T. & Yoshikoshi, T. (2004). A Search for TeV Gamma-Ray Emission from the PSR B1259-63/SS 2883 Binary System with the CANGAROO-II 10 Meter Telescope. ApJ, **607**, 949–958. 130

Khangulyan, D., Hnatic, S., Aharonian, F. & Bogovalov, S. (2007). TeV light curve of PSR B1259-63/SS2883. MNRAS, **380**, 320–330. 22, 166

Kochhar, R.K. (1981). On the relationship between pulsars and supernova remnants. *Journal of Astrophysics and Astronomy*, **2**, 87–93. 5

Kosack, K., Djannati-Atai, A., Lemiere, A. & et al. (2008). H.E.S.S. VHE Gamma-ray sources without identified counterparts. *International Cosmic Ray Conference*, **2**, 621–624. xxx, 154

Kraushaar, W.L. & Clark, G.W. (1962). Gamma Ray Astronomy. *Scientific American*, **206**, 52–61. 25

Kraushaar, W.L., Clark, G.W., Garmire, G.P., Borken, R., Higbie, P., Leong, V. & Thorsos, T. (1972). High-Energy Cosmic Gamma-Ray Observations from the OSO-3 Satellite. ApJ, **177**, 341. 25

Levine, A.M., Bradt, H., Cui, W., Jernigan, J.G., Morgan, E.H., Remillard, R., Shirey, R.E. & Smith, D.A. (1996). First Results from the All-Sky Monitor on the Rossi X-Ray Timing Explorer. ApJ, **469**, L33. 121

Leyder, J.C., Walter, R. & Lubiński, P. (2009). INTEGRAL detects 1A 1118-615 in outburst. *The Astronomer's Telegram*, **1949**, 1. 144

Ling, Z., Zhang, S.N. & Tang, S. (2009). Determining the Distance of Cyg X-3 with its X-Ray Dust Scattering Halo. *apj*, **695**, 1111–1120. 63

Manchester, R.N. & Taylor, J.H. (1977). *Pulsars*. Springer Verlag, 2001. 16

Mangano, V. (2009). 1A 1118-61: detection of the pulsation period in Swift-XRT data. *The Astronomer's Telegram*, **1896**, 1. 144

Maraschi, L., Huckle, H.E., Ives, J.C. & Sanford, P.W. (1976). Spectral characteristics of transient X-ray sources. Nature, **263**, 34–36. 144

Marecki, A. & Swoboda, B. (2011). The transition from quasar radio-loud to radio-quiet state in the framework of the black hole scalability hypothesis. A&A, **525**, A6. 4

Margon, B., Lampton, M., Bowyer, S. & Cruddace, R. (1971). A Pulsing X-Ray Source in Circinus. *apjl*, **169**, L23+. 110

Martí, J., Paredes, J.M. & Estalella, R. (1992). Modelling Cygnus X-3 radio outbursts - Particle injection into twin jets. A&A, **258**, 309–315. 19

Martí, J., Rodriguez, L.F., Mirabel, I.F. & Paredes, J.M. (1996). A search for arcminute-scale radio jets in Cygnus X-1. A&A, **306**, 449. 19

Martí, J., Paredes, J.M. & Peracaula, M. (2001). Development of a two-sided relativistic jet in Cygnus X-3. A&A, **375**, 476–484. xvi, 20

Martocchia, A., Motch, C. & Negueruela, I. (2005). The low X-ray state of LS 5039 / RX J1826.2-1450. A&A, **430**, 245–253. 54

Massi, M., Ribó, M., Paredes, J.M., Peracaula, M. & Estalella, R. (2001). One-sided jet at milliarcsecond scales in LS I +61° 303. A&A, **376**, 217–223. 52

Massi, M., Ribó, M., Paredes, J.M., Garrington, S.T., Peracaula, M. & Martí, J. (2004). Hints for a fast precessing relativistic radio jet in LS I +61303. A&A, **414**, L1–L4. 22

Matthews, J. (2005). A Heitler model of extensive air showers. *Astroparticle Physics*, **22**, 387–397. 28

Miller-Jones, J.C.A., Blundell, K.M., Rupen, M.P., Mioduszewski, A.J., Duffy, P. & Beasley, A.J. (2004). Time-sequenced Multi-Radio Frequency Observations of Cygnus X-3 in Flare. *apj*, **600**, 368–389. 63

Mioduszewski, A.J., Rupen, M.P., Hjellming, R.M., Pooley, G.G. & Waltman, E.B. (2001). A One-sided Highly Relativistic Jet from Cygnus X-3. ApJ, **553**, 766–775. 63

Mirabel, I.F. (2006). Very energetic gamma-rays from microquasars and binary pulsars. *Science*, **312**, 1759–+. xv, 2

Mirabel, I.F. & Rodríguez, L.F. (1994). A superluminal source in the Galaxy. Nature, **371**, 46–48. 18

Mirabel, I.F., Dhawan, V., Chaty, S., Rodriguez, L.F., Marti, J., Robinson, C.R., Swank, J. & Geballe, T. (1998). Accretion instabilities and jet formation in GRS 1915+105. A&A, **330**, L9–L12. 18

Moneti, A. (1992). Optical and infrared observations of Circinus X-1. *aap*, **260**, L7–L10. 110

Motch, C., Pakull, M.W., Janot-Pacheco, E. & Mouchet, M. (1988). Coordinated X-ray and optical observations of the pulsating X-ray transient A 1118-61. A&A, **201**, 63–71. 144

Motch, C., Haberl, F., Dennerl, K., Pakull, M. & Janot-Pacheco, E. (1997). New massive X-ray binary candidates from the ROSAT Galactic Plane Survey. I. Results from a cross-correlation with OB star catalogues. A&A, **323**, 853–875. 54

Myung, I.J. (2003). Tutorial on maximum likelihood estimation. *J. Math. Psychol.*, **47**, 90–100. xxiii, 97, 99

Negueruela, I., Smith, D.M., Reig, P., Chaty, S. & Torrejón, J.M. (2006). Supergiant Fast X-ray Transients: A New Class of High Mass X-ray Binaries Unveiled by INTEGRAL. In A. Wilson, ed., *The X-ray Universe 2005*, vol. 604 of *ESA Special Publication*, 165. 152

Neronov, A. & Chernyakova, M. (2007). Radio-to-TeV γ-ray emission from PSR B1259 63. Ap&SS, **309**, 253–259. 22, 166

Nespoli, E., Fabregat, J. & Mennickent, R.E. (2008). Unveiling the nature of six HMXBs through IR spectroscopy. A&A, **486**, 911–917. 152

Neyman, J. & Pearson, E.S. (1933). On the Problem of the Most Efficient Tests of Statistical Hypotheses. *Royal Society of London Philosophical Transactions Series A*, **231**, 289–337. 102

Nolan, P.L., Abdo, A.A., Ackermann, M., Ajello, M., Allafort, A., Antolini, E., Atwood, W.B., Axelsson, M., Baldini, L., Ballet, J. & et al. (2012). Fermi Large Area Telescope Second Source Catalog. ApJS, **199**, 31. 49, 136

Ormes, J.F., Atwood, W., Burnett, T., Grove, E., Longo, F., McEnery, J., Mizuno, T. & Ritz, S. (2007). The GLAST Background Model. In S. Ritz, P. Michelson & C.A. Meegan, eds., *The First GLAST Symposium*, vol. 921 of *American Institute of Physics Conference Series*, 560–561. 35

Page, K.L., Osborne, J.P., Kuin, N.P.M., Woodward, C.E., Schwarz, G.J., Starrfield, S., Shore, S.N. & Walter, F.M. (2013). Detection of super-soft emission in nova V339 Del. *The Astronomer's Telegram*, **5470**, 1. 9

Paredes, J.M., Martí, J., Ribó, M. & Massi, M. (2000). Discovery of a High-Energy Gamma-Ray-Emitting Persistent Microquasar. *Science*, **288**, 2340–2342. 54

Parent, D., Kerr, M., den Hartog, P.R., Baring, M.G., DeCesar, M.E., Espinoza, C.M., Gotthelf, E.V., Harding, A.K., Johnston, S., Kaspi, V.M., Livingstone, M., Romani, R.W., Stappers, B.W., Watters, K., Weltevrede, P., Abdo, A.A., Burgay, M., Camilo, F., Craig, H.A., Freire, P.C.C., Giordano, F., Guillemot, L., Hobbs, G., Keith, M., Kramer, M., Lyne, A.G., Manchester, R.N., Noutsos, A., Possenti, A. & Smith, D.A. (2011). Observations of Energetic High Magnetic Field Pulsars with the Fermi Large Area Telescope. ApJ, **743**, 170. 148

Pittard, J.M. (2010). Models of the Non-Thermal Emission from Early-Type Binaries. In J. Martí, P.L. Luque-Escamilla & J.A. Combi, eds., *High Energy Phenomena in Massive Stars*, vol. 422 of *Astronomical Society of the Pacific Conference Series*, 145. 8

Pollock, A.M.T., Masnou, J.L., Bignami, G.F., Hermsen, W., Swanenburg, B.N., Kanbach, G., Lichti, G.G. & Wills, R.D. (1981). Search for gamma-radiation from extragalactic objects using a likelihood method. A&A, **94**, 116–120. 103

Portegies Zwart, S.F., Verbunt, F. & Ergma, E. (1997). The formation of black-holes in low-mass X-ray binaries. A&A, **321**, 207–212. 3

Ray, P.S., Kerr, M., Parent, D., Abdo, A.A., Guillemot, L., Ransom, S.M., Rea, N., Wolff, M.T., Makeev, A., Roberts, M.S.E., Camilo, F., Dormody, M., Freire, P.C.C., Grove, J.E., Gwon, C., Harding, A.K., Johnston, S., Keith, M., Kramer, M., Michelson, P.F., Ro-

mani, R.W., Saz Parkinson, P.M., Thompson, D.J., Weltevrede, P., Wood, K.S. & Ziegler, M. (2011). Precise γ-ray Timing and Radio Observations of 17 Fermi γ-ray Pulsars. *apjs*, **194**, 17–+. xxi, xxii, 76, 79, 84, 85, 86

Ribó, M., Paredes, J.M., Moldón, J., Martí, J. & Massi, M. (2008). The changing milliarcsecond radio morphology of the gamma-ray binary LS 5039. A&A, **481**, 17–20. 54

Rodriguez, J., Garau, A.D., Grebenev, S., Parmard, A., Roques, J.P., Schonfelder, V., Ubertini, P., Walter, R. & Westergaard, N.J. (2004). INTEGRAL discovery of a possible new source IGR J18410-0535. *The Astronomer's Telegram*, **340**, 1. 152

Romero, G.E., Torres, D.F., Kaufman Bernadó, M.M. & Mirabel, I.F. (2003). Hadronic gamma-ray emission from windy microquasars. A&A, **410**, L1–L4. 63, 69

Romero, G.E., Okazaki, A.T., Orellana, M. & Owocki, S.P. (2007). Accretion vs. colliding wind models for the gamma-ray binary LS I +61 303: an assessment. A&A, **474**, 15–22. 22

Romero, G.E., Del Valle, M.V. & Orellana, M. (2010). Gamma-ray absorption and the origin of the gamma-ray flare in Cygnus X-1. A&A, **518**, A12. 20

Sabatini, S., Tavani, M., Caraveo, P., Barbiellini, G., Costa, E., Feroci, M., Argan, A., Bulgarelli, A., Cattaneo, P.W., Chen, A.W.,

D'Ammando, F., de Paris, G., Del Monte, E., Di Cocco, G., Donnarumma, I., Evangelista, Y., Ferrari, A., Fiorini, M., Fuschino, F., Galli, M., Gianotti, F., Giuliani, A., Giusti, M., Labanti, C., Lazzarotto, F., Lipari, P., Longo, F., Marisaldi, M., Mereghetti, S., Morelli, E., Moretti, E., Morselli, A., Pacciani, L., Pellizzoni, A., Perotti, F., Piano, G., Picozza, P., Pilia, M., Pucella, G., Prest, M., Rapisarda, M., Rappoldi, A., Rubini, A., Scalise, E., Soffitta, P., Striani, E., Trifoglio, M., Trois, A., Vallazza, E., Vercellone, S., Zambra, A., Zanello, D., Pittori, C., Verrecchia, F., Vittorini, V., Santolamazza, P., Giommi, P., Colafrancesco, S., Antonelli, L.A. & Salotti, L. (2010). Galactic transients with AGILE: the case of Eta Carinae and Cygnus X-1. In *38th COSPAR Scientific Assembly*, vol. 38 of *COSPAR Meeting*, 2596. 20

Schoenfelder, V., Aarts, H., Bennett, K., de Boer, H., Clear, J., Collmar, W., Connors, A., Deerenberg, A., Diehl, R., von Dordrecht, A., den Herder, J.W., Hermsen, W., Kippen, M., Kuiper, L., Lichti, G., Lockwood, J., Macri, J., McConnell, M., Morris, D., Much, R., Ryan, J., Simpson, G., Snelling, M., Stacy, G., Steinle, H., Strong, A., Swanenburg, B.N., Taylor, B., de Vries, C. & Winkler, C. (1993). Instrument description and performance of the Imaging Gamma-Ray Telescope COMPTEL aboard the Compton Gamma-Ray Observatory. ApJS, **86**, 657–692. 103

Sguera, V., Romero, G.E., Bazzano, A., Masetti, N., Bird, A.J. & Bassani, L. (2009). Dissecting the Region of 3EG J1837-0423 and HESS J1841-

055 with INTEGRAL. ApJ, **697**, 1194–1205. 153, 159

Shrader, C.R., Titarchuk, L. & Shaposhnikov, N. (2010). New Evidence for a Black Hole in the Compact Binary Cygnus X-3. ApJ, **718**, 488–493. 63

Singh, N.S., Naik, S., Paul, B., Agrawal, P.C., Rao, A.R. & Singh, K.Y. (2002). New measurements of orbital period change in Cygnus X-3. *aap*, **392**, 161–167. 120, 121

Smponias, T. & Kosmas, T.S. (2011). Modelling the equatorial emission in a microquasar. MNRAS, **412**, 1320–1330. 2

Stark, M.J. & Saia, M. (2003). Doppler Modulation of X-Ray Lines in Cygnus X-3. *apjl*, **587**, L101–L104. 63

Staubert, R., Pottschmidt, K., Doroshenko, V., Wilms, J., Suchy, S., Rothschild, R. & Santangelo, A. (2011). Finding a 24-day orbital period for the X-ray binary 1A 1118-616. A&A, **527**, A7. 144

Stecker, F.W. (1975). Galactic gamma-ray observations and galactic structure. *NASA STI/Recon Technical Report N*, **76**, 12933–+. 16

Stewart, R.T., Nelson, G.J., Penninx, W., Kitamoto, S., Miyamoto, S. & Nicolson, G.D. (1991). On the puzzling nature of the X-ray binary Circinus X-1. *mnras*, **253**, 212–216. 110

Tam, P.H.T., Kong, A.K.H., Huang, R.H.H. & Hui, C.Y. (2010). Fermi/LAT and Swift/XRT detection of increased activity from the binary system PSR B1259-63/SS 2883. *The Astronomer's Telegram*, **3046**, 1. 125, 169

Tam, P.H.T., Huang, R.H.H., Takata, J., Hui, C.Y., Kong, A.K.H. & Cheng, K.S. (2011). Discovery of GeV γ-ray Emission from PSR B1259-63/LS 2883. ApJ, **736**, L10. 171

Tavani, M. & Arons, J. (1997). Theory of High-Energy Emission from the Pulsar/Be Star System PSR 1259-63. I. Radiation Mechanisms and Interaction Geometry. *apj*, **477**, 439–+. 22, 61

Tavani, M., Grove, J.E., Purcell, W., Hermsen, W., Kuiper, L., Kaaret, P., Ford, E., Wilson, R.B., Finger, M., Harmon, B.A., Zhang, S.N., Mattox, J., Thompson, D. & Arons, J. (1996). High-energy emission from the PSR B1259-63 system near periastron. A&AS, **120**, C221. xxvii, 134

Tavani, M., Kniffen, D., Mattox, J.R., Paredes, J.M. & Foster, R. (1998). The Variable Gamma-Ray Source 2CG 135+01. *apjl*, **497**, L89. 27

The Fermi LAT collaboration (2010). Fermi Large Area Telescope Observation of a Gamma-ray Source at the Position of Eta Carinae. *ArXiv e-prints*. 9

The Fermi LAT Collaboration, Coe, M.J., Di Mille, F., Edwards, P.G., Filipović, M.D., Payne, J.L., Stevens, J. & Torres, M.A.P. (2012). Periodic Emission from the Gamma-ray Binary 1FGL J1018.6-5856. *ArXiv e-prints*. xix, xx, 57, 59, 60

Tudose, V., Fender, R.P., Linares, M., Maitra, D. & van der Klis, M. (2009). The disc-jet coupling in the neutron star X-ray binary Aquila X-1. MNRAS, **400**, 2111–2121. 11

Uchiyama, Y., Takahashi, T., Aharonian, F.A. & Mattox, J.R. (2002). ASCA View of the Supernova Remnant γ Cygni (G78.2+2.1): Bremsstrahlung X-Ray Spectrum from Loss-flattened Electron Distribution. *apj*, **571**, 866–875. 15

van Kerkwijk, M.H., Geballe, T.R., King, D.L., van der Klis, M. & van Paradijs, J. (1996). The Wolf-Rayet counterpart of Cygnus X-3. A&A, **314**, 521–540. 63

Vernetto, S. & for the ARGO-YBJ collaboration (2013). Study of the Crab Nebula TeV emission variability during five years with ARGO-YBJ. *ArXiv e-prints*. 5

Weekes, T., ed. (2003). *Very High Energy Gamma-Ray Astronomy*, vol. 11 of *Wiley Praxis Series in Astronomy and Astrophysics*. 11, 165

Wex, N., Johnston, S., Manchester, R.N., Lyne, A.G., Stappers, B.W. & Bailes, M. (1998). Timing models for the long orbital period binary pulsar PSR B1259-63. MNRAS, **298**, 997–1004. 61

Whelan, J.A.J., Mayo, S.K., Wickramasinghe, D.T., Murdin, P.G., Peterson, B.A., Hawarden, T.G., Longmore, A.J., Haynes, R.F., Goss, W.M., Simons, L.W., Caswell, J.L., Little, A.G. & McAdam, W.B. (1977). The optical and radio counterpart of Circinus X-1 /3U 1516-56/. *mnras*, **181**, 259–271. 110